

Triplet Exciton Management in Organic Optoelectronic Devices



Patrick Joseph Conaghan

Department of Physics
University of Cambridge

This dissertation is submitted for the degree of
Doctor of Philosophy

This thesis is dedicated to Sophie, Ruairi and the Little One.

Declaration

I hereby declare that except where specific reference is made to the work of others, the contents of this dissertation are original and have not been submitted in whole or in part for consideration for any other degree or qualification in this, or any other university. This dissertation is my own work and contains nothing which is the outcome of work done in collaboration with others, except as specified in the text and Acknowledgements. This dissertation contains fewer than 65,000 words including appendices, bibliography, footnotes, tables and equations and has fewer than 150 figures.

Patrick Joseph Conaghan

June 2019

Acknowledgements

Many people deserve my thanks for their mentorship, tuition, collaboration, assistance and friendship. This thesis would not have been possible without them.

Firstly, thank you to my supervisor, Neil Greenham, for the opportunity to study here in Cambridge and for feedback, support and guidance. Thank you to Dan Credgington for acting as an informal second supervisor on a fruitful project. Thank you to Matt Menke and Andrew Pearson for showing me the ropes in the lab and being the first ports of call for more than their fair share of questions. Thank you to Alex Romanov for sharing an unending supply of new and interesting materials. Thank you to Emrys Evans, Leah Weiss and William Myers for making ESR measurements possible.

I have been lucky to collaborate with a large number of people. I have been lent generous amounts of other people's time, effort and expertise. I have received ample help when I needed it, been given plenty of good advice and have made some firm friendships. In addition to those already mentioned I need to say a big thank you to all of: Ned Booker, Mike Price, Pete Budden, Heather Goodwin, Simon Dowland, Nate Davis, James Xiao, Arfa Karani, Feng Li, Alex Gillett, Saul Jones, Campbell Matthews, Bluebell Drummond, Jiangbin Zhang, Jeff Gorman, Florian Auras, Daniele Di Nuzzo, Florian Lombeck and Ian Jacobs.

Thank you to all of the technical and administrative staff: Richard Gymer, Alex Crook, Anthony Barnett, Roger Beadle, Jennie Nelson, William Mortimer, Egle Bunkute, Alison Barker, Angela Campbell and Gilly Walker. I must also make a special thank you very much to Fliss Cadbury at the university counselling service.

Thank you to my family and friends who have supported and encouraged me throughout. Especially thank you to Sophie, for everything. Ruairi, you were less helpful, but thanks anyway.

I acknowledge funding from the Engineering and Physical Sciences Research Council.

Abstract

To date optoelectronic devices have been dominated by inorganic semiconductors such as silicon and gallium nitride. However organic semiconductors have many potential advantages and have shown significant research progress in both organic light-emitting diodes and organic photovoltaics.

Tightly-bound excitons form intermediate states in the operation of both organic light-emitting diodes and organic photovoltaics. Many properties of an exciton are determined by its spin state, which can either be a spin-zero singlet or a spin-one triplet. In both organic light-emitting diodes and organic photovoltaics triplet excitons can be a source of loss due to poor radiative coupling to the ground state and energy loss on formation from the singlet state. In this thesis, methods of avoiding loss pathways through triplet states are investigated in both organic light-emitting diodes and organic photovoltaics.

Carbene-metal-amides are a new class of emitter material for organic light-emitting diodes. High-performance devices are reported with maximum external quantum efficiency of 27%, which indicates effective triplet utilisation. Emission colour can be selected through both molecular design and host environment allowing the demonstration of blue-emitting devices with 19% external quantum efficiency. Host-free devices have been fabricated with record external quantum efficiency of 23%, enabled by a resistance to concentration-dependent luminescence quenching.

Electron spin resonance has been used to investigate the mechanism of intersystem crossing between singlets and triplets in the important organic light-emitting diode material, 4CzIPN. It is demonstrated that the spin-vibronic model of intersystem crossing breaks down in device-relevant solid films. Evidence is instead found for back transfer from a spin-correlated radical pair state being the dominant mode of intersystem crossing. With increased film concentration the signal becomes dominated by free polarons, suggesting that charge separation may be a mechanism of luminescence quenching at high concentration.

In many organic photovoltaic material systems triplets are low-lying states from which charge separation is not energetically favoured. In this thesis, attempts are made to negate this triplet loss pathway by the use of low singlet-triplet energy gap materials to ensure that the charge-transfer state can be endothermically accessed from all molecular exciton states.

Table of contents

List of figures	xv
List of tables	xix
1 Introduction	1
2 Background	3
2.1 Organic semiconductors	3
2.1.1 Molecular orbitals	3
2.2 Excited states	4
2.2.1 Excitons	4
2.2.2 Charge-transfer states	6
2.2.3 Polarons	7
2.3 Absorption and emission of light	8
2.3.1 Fluorescence	8
2.3.2 Phosphorescence	8
2.3.3 Thermally Activated Delayed Fluorescence	9
2.4 Spin interactions	11
2.4.1 Zeeman splitting	12
2.4.2 Hyperfine splitting	12
2.4.3 Zero-field splitting	13
2.4.4 Electron Spin Resonance	14
2.5 Organic optoelectronic devices	17
2.5.1 Organic photovoltaics	18
2.5.2 Organic light-emitting diodes	22
3 Methods	27
3.1 Vacuum thermal evaporation	27
3.2 Spin-coating	28

3.3	Photovoltaic characterisation	28
3.3.1	External quantum efficiency	29
3.3.2	Power conversion efficiency	29
3.4	Light-emitting diode characterisation	31
3.4.1	Electrical characterisation	31
3.4.2	Spectral characterisation	32
3.5	Absorption	32
3.5.1	UV-Vis absorption	33
3.5.2	Photothermal deflection spectroscopy	33
3.5.3	Transient absorption spectroscopy	34
3.6	Photoluminescence	35
3.6.1	Steady-state photoluminescence	35
3.6.2	Transient photoluminescence	35
3.6.3	Photoluminescence quantum efficiency	35
3.7	Ellipsometry	36
3.8	Atomic force microscopy	36
3.9	Grazing incidence wide angle X-ray scattering	37
3.10	Electron spin resonance	37
4	Carbene-metal-amides	39
4.1	Introduction	39
4.2	Collaborator contributions	41
4.3	Experimental methods	42
4.4	Results	46
4.4.1	Colour tuning through molecular design	61
4.4.2	Silver-centred CMA OLEDs	71
4.5	Discussion	74
4.6	Conclusion	76
5	The mechanism of intersystem crossing in a benchmark TADF material	77
5.1	Introduction	77
5.2	Collaborator contributions	78
5.3	Experimental methods	78
5.4	Results	80
5.5	Discussion	92
5.6	Conclusion	94

6	Triplet Excitons in Organic Photovoltaics	95
6.1	Introduction	95
6.2	Collaborator contributions	98
6.3	Experimental methods	98
6.4	Results	100
6.4.1	TXO-TPA	100
6.4.2	APDC-DTPA	113
6.5	Discussion	118
6.6	Conclusion	119
7	Conclusions	121
7.1	Carbene-metal-amide organic light-emitting diodes	121
7.2	Intersystem crossing in 4CzIPN	122
7.3	Open-circuit voltage loss in organic photovoltaics	123
7.4	Outlook and concluding remarks	123
	References	125

List of figures

2.1	State diagram indicating the ground state (S_0) and lowest energy singlet (S_1) and triplet (T_1) excitons	6
2.2	Triplet substate energies as a function of B_0 with varying orientation of B_0 .	16
2.3	Simulated triplet ESR spectra ($D > 0$) displaying varying absorption-emission patterns according to preferential population of $ X\rangle$ (bottom), $ Y\rangle$ (middle) or $ Z\rangle$ (top). Absorptive (A) and emissive (E) transitions are labelled	17
2.4	Offset HOMO and LUMO levels between donor and acceptor materials in a type II heterojunction	19
2.5	State diagrams representing OPV heterojunction blends with varying CT and T_1 state energetic ordering	21
2.6	An idealised OLED architecture under forward bias	22
3.1	Example J-V curve measured from a PCDTBT:PC ₇₁ BM OPV in the dark and under 1-sun solar simulator illumination	30
4.1	The chemical structure of gold-centred CMA material Au-Cz	40
4.2	CMA OLED Device architecture	43
4.3	Proposed energy levels in OLED devices at open circuit a) architecture 1 and b) architecture 2	44
4.4	Chemical structures of materials used in CMA OLEDs	45
4.5	Current density-voltage and luminance-voltage characteristics for Au-Cz OLEDs	47
4.6	Atomic force microscopy images of UGH2 hole-blocking layers a) with and b) without a 10 wt.% doping of TPBi	48
4.7	η_{eqe} as a function of current density for Au-Cz OLEDs	49
4.8	Histograms of peak η_{eqe} for Au-Cz OLEDs in a) an mCP host and b) host-free devices. c) and d) η_{eqe} as a function of current density for all samples included in the histograms	51

4.9	η_{eqe} as a function of current density for all tested devices with a) mCP: Au-Cz and b) host-free Au-Cz emissive layers. The line colours represent different device fabrication batches	52
4.10	Reproducibility of a) J-V and b) L-V characteristics for host-free Au-Cz OLED devices. The line colours represent different device fabrication batches	53
4.11	The angular intensity dependence of Au-Cz OLEDs at varying concentration in mCP	54
4.12	2D GIWAXS patterns of drop-cast Au-Cz and thermally evaporated Au-Cz host-free and mCP: Au-Cz films. The intensity of X-ray scatter is presented on a common colour scale	56
4.13	Electroluminescence and photoluminescence for Au-Cz	58
4.14	CIE Colour space diagram for Au-Cz OLEDs	59
4.15	The absorption onset of a host-free Au-Cz film and in a TCP and mCP host as measured by photothermal deflection spectroscopy	60
4.16	Transient photoluminescence a) kinetic and b) spectral evolution for a host-free Au-Cz film and at 20 wt.% in mCP and TCP hosts. $\lambda_{Ex} = 400$ nm . . .	62
4.17	a) Transient photoluminescence decay kinetics of a host-free Au-Cz film at varying temperature with $\lambda_{Ex} = 400$ nm b) Arrhenius plot with associated curve fitting	63
4.18	a) Temperature dependent photoluminescence spectra and b) peak energy shift for an Au-Cz solid film. $\lambda_{Ex} = 400$ nm	64
4.19	Absorption coefficient and photoluminescence of gold-centred CMA materials with varying side group substitutions	65
4.20	a) J-V and b) L-V characteristics of OLED devices incorporating Au-Cz-(^t Bu) ₂ and Au-Cz-(^t Bu)(CF ₃)	68
4.21	η_{eqe} as a function of current density for Au-Cz-(^t Bu) ₂ and Au-Cz-(^t Bu)(CF ₃) OLEDs of varying host polarity	69
4.22	a) Electroluminescence spectra and b) CIE colour space diagram for OLED devices incorporating gold-centred CMA emitters. Spectra were measured at approximately 100 cd m ⁻²	70
4.23	a) Current density - Voltage and (b) Luminance - Voltage characteristics for silver-centred CMA OLEDs	72
4.24	η_{eqe} as a function of current density for silver-centred CMA OLEDs	73
4.25	Room temperature transient photoluminescence kinetics of silver-centred CMA materials Ag-Cz and Ag-Cz-(^t Bu) ₂	74
5.1	Chemical structures of a) 4CzIPN and b) CBP	79

5.2	UV-Vis absorption of 4CzIPN thin films and in toluene solution at room temperature (solid lines) and at 80 K (dotted lines)	80
5.3	Transient ESR data from a 4CzIPN sample in a 100 μ M frozen toluene solution at 80 K	82
5.4	ESR data and simulation for 4CzIPN in a frozen 100 μ M toluene solution integrated over the first 1 ms following photoexcitation	83
5.5	Transient ESR data from thin films of 4CzIPN doped in a CBP host at (a) 1 wt.% (b) 5 wt.% (c) 50 wt.% and (d) host-free	84
5.6	Time evolution of ESR signal for a) 1 wt.% and b) 5 wt.% films of 4CzIPN dispersed in CBP	86
5.7	Transient ESR data, simulation and kinetic for CBP:4CzIPN 5 wt.% film	87
5.8	CBP:4CzIPN 5 wt.% transient ESR kinetic at 347 mT	88
5.9	An illustration of absorptive (A) and emissive (E) ESR transitions from an exclusively populated $ 1,0\rangle$ state, showing the origin of an AEEAAE signal pattern	89
5.10	Time evolution of ESR signal for films of a) 50 wt.% of 4CzIPN dispersed in CBP and b) host-free 4CzIPN	90
5.11	Transient ESR data, simulation and kinetic for a host-free film of 4CzIPN	91
5.12	A proposed kinetic model for intersystem crossing in solid films of CBP:4CzIPN in a magnetic field	93
6.1	Chemical structures of materials used in OPV device blends	97
6.2	Proposed energy level diagram of materials used in this chapter: PFB, APDC-DTPA, TXO-TPA, FDE-HTPA, PC ₆₁ BM	100
6.3	J-V characteristics a) in the dark and b) under 100 mW cm ⁻² illumination from an AM1.5G solar simulator of PFB:TXO-TPA bulk heterojunction OPV cells	102
6.4	Absorption spectra of TXO-TPA, PFB, PC ₆₁ BM and blends of PFB:TXO-TPA and TXO-TPA:PC ₆₁ BM with 20 wt.% of TXO-TPA.	103
6.5	External quantum efficiency as a function of excitation wavelength for PFB:TXO-TPA at varying reverse bias	104
6.6	Electroluminescence spectrum of a PFB:TXO-TPA device	104
6.7	J-V characteristics a) in the dark and b) under 100 mW cm ⁻² illumination from an AM1.5G solar simulator of TXO-TPA:PC ₆₁ BM bulk heterojunction OPV cells	106
6.8	External quantum efficiency as a function of excitation wavelength for TXO-TPA:PC ₆₁ BM at varying reverse bias	107

6.9	Electroluminescence spectrum of a TXO-TPA:PC ₆₁ BM device	108
6.10	J-V characteristics a) in the dark and b) under 100 mW cm ⁻² illumination from an AM1.5G solar simulator of pure PC ₆₁ BM OPV cells	110
6.11	External quantum efficiency as a function of excitation wavelength for TXO- TPA:PC ₆₁ BM bulk heterojunction OPV cells with varying composition ratios	111
6.12	Transient absorption spectroscopy of a) pure TXO-TPA b) pure PC ₆₁ BM and c) TXO-TPA:PC ₆₀ BM films	112
6.13	Absorption spectra of APDC-DTPA, FDE-HTPA and blends of APDC- DTPA: FDE-HTPA (1:1 by weight) and PFB:APDC-DTPA (1:3 by weight)	114
6.14	J-V characteristics a) in the dark and b) under 100 mW cm ⁻² illumination from an AM1.5G solar simulator of PFB:APDC-DTPA (1:3 by weight) OPV cells	115
6.15	J-V characteristics a) in the dark and b) under 100 mW cm ⁻² illumina- tion from an AM1.5G solar simulator of APDC-DTPA:FDE-HTPA (1:1 by weight) OPV cells	117

List of tables

2.1	Spin eigenstates of a two-electron system	5
4.1	Molecular composition of CMA materials	45
4.2	Summary of Au-Cz OLED performance	46

Chapter 1

Introduction

Semiconductor devices such as diodes and transistors form the basis of modern electronics and computing by allowing the construction of switches, logic gates and integrated circuits. Additionally the excitation or relaxation of electrons across the bandgap in a semiconductor allows the absorption or emission of light for energy conversion applications in optoelectronic devices such as photovoltaics or light-emitting diodes.

To avoid and reduce risks to human health, livelihoods, food security, water supply, human security and biodiversity posed by global warming it is vital to restrict the anthropogenic emission of greenhouse gases. The dominant sources of these emissions are in energy conversion from fossil fuels for use in lighting, heating and transport. Semiconductor optoelectronic devices can be used to reduce human reliance on fossil fuels by providing energy conversion mechanisms from sunlight to electricity in the case of photovoltaics and efficient conversion from electricity to light in the case of light-emitting diodes.

To date, optoelectronic devices have been dominated by inorganic semiconductors such as silicon and gallium nitride. However organic semiconductors have many potential advantages such as the ability to tune material properties through molecular design, the potential for lightweight and flexible devices and their versatility in device fabrication techniques such as thermal evaporation or solution processing.

This thesis will explore the effect of spin on the performance of organic optoelectronic devices and in particular how triplet excitons can be efficiently converted to light in organic light-emitting diodes (OLEDs), or avoided in organic photovoltaics (OPVs). Chapter 2 will introduce some of the concepts and definitions which are important to later chapters and review the current state of the scientific field. The electronic structure of organic semiconductors and the properties of their excited states will be introduced along with spin-dependent interactions which will be later used to investigate material properties. Finally the

properties of OLEDs and OPVs and the influence of spin will be discussed and will be used to provide motivation for the investigations described in later chapters.

Chapter 3 will describe the key experimental methods used including the preparation of device and film samples through both solution processing and vacuum thermal evaporation; the characterisation of films through spectroscopic ellipsometry, atomic force microscopy, absorption and photoluminescence; the characterisation of photovoltaics and light-emitting diodes and the determination of their efficiency; and investigation of spin dynamics through electron spin resonance.

Chapter 4 describes the fabrication and characterisation of OLEDs incorporating carbene-metal-amide emitting materials for efficient utilisation of triplet excitons. The ability to tune emission colour through molecular engineering and variation in the molecular environment — notably the polarity of any host material — of the emitting molecules is discussed, including the fabrication of blue-emitting devices exhibiting high efficiency. It has been discovered that some carbene-metal-amides exhibit a remarkable resistance to luminescence quenching at high concentration. This property has been exploited through the fabrication of record high efficiency host-free OLED devices. Additionally the first demonstration of OLEDs incorporating mononuclear silver is described.

Electron spin resonance data from solid films representing the emissive layer of a high-efficiency OLED device is presented in chapter 5. Evidence is shown for the mechanism of intersystem crossing between singlet and triplet manifolds in a benchmark thermally activated delayed fluorescence system which intriguingly contradicts the widely purported spin-vibronic model, informs the design of emitting materials for high-efficiency OLEDs and opens a research space for investigation of other similar materials.

Attempts to reduce the negative effect of triplet excitons in OPVs are described in chapter 6. OPV devices are fabricated with active layer designs to limit non-radiative recombination pathways through molecular triplet excitons. Confounding factors including poor optical absorption and charge transport limited the effectiveness of the devices, but a discussion of the emergence of non-fullerene acceptors demonstrates that OPVs still have potential for improvement and can be competitive with rival technologies.

Chapter 2

Background

2.1 Organic semiconductors

2.1.1 Molecular orbitals

An isolated carbon atom has a ground-state electronic configuration of $(1s)^2(2s)^2(2p)^2$, however when carbon forms either homo- or hetero-atomic bonds the 2s and 2p orbitals form hybridised sp^3 , sp^2 or sp^1 orbitals depending on the number of 2p orbitals involved.

In the case of sp^2 hybridisation — formed through mixing between the 2s, $2p_x$ and $2p_y$ orbitals — the sp^2 electrons form strong σ -bonds with neighbouring atoms. The remaining $2p_z$ electron is able to form hybridised π -bonds with neighbouring carbon atoms. The π -orbitals are located above and below the molecular plane and can be delocalised across alternating double and single bonds. This is known as a conjugated system and, as will be described, it enables semiconducting behaviour in some organic materials.

σ -orbitals lie directly on the inter-nuclear axis and hence there is a large energy separation of 8 eV or greater between a bonding σ - and an anti-bonding σ^* -orbital. In contrast the electron density in π -orbitals is away from the internuclear axis and the energy splitting between the bonding π - and anti-bonding π^* -orbitals is smaller. Consequently the highest occupied molecular orbital (HOMO) and lowest unoccupied molecular orbital (LUMO) of organic semiconducting molecules tend to be π - and π^* -orbitals respectively. The HOMO-LUMO energy gap determines the onset of absorption of electromagnetic radiation and functions in a manner analogous to the bandgap in inorganic semiconductors. Interaction between an organic semiconductor and visible light is possible when the HOMO-LUMO gap is in the range 1-3 eV.

2.2 Excited states

An organic semiconductor molecule in the ground state will have a fully occupied HOMO and an unoccupied LUMO. The molecule is said to be in an excited state when an electron is present in a higher-lying orbital than the HOMO or when an unoccupied site — which can be described as a quasiparticle known as a hole — exists in an orbital lying lower than the LUMO. This thesis is largely concerned with the behaviour of neutral excited states in which an excited electron is coulombically bound to a hole either on the same or on an adjacent molecule. Charged excited states known as polarons will also be introduced as they are also highly significant in the operation of both OLED and OPV devices and contribute strongly to electron spin resonance data in chapter 5.

Neutral excited states can be accessed through the absorption of a photon, which promotes an electron to a previously unoccupied higher orbital and leaves behind a hole in what was a fully occupied orbital. According to Kasha's rule, the excited state will usually undergo rapid vibrational relaxation — known as internal conversion — until it reaches the lowest-energy excited state of the same spin.[1] Neutral excited states can also be produced through the recombination of charge carriers which have been electrically injected directly into the molecular frontier orbitals; this will always produce the lowest energy excited state as transport of the charged excitation will preferentially occur through the lowest energy states.

2.2.1 Excitons

Excitons are neutral states in which an excited electron remains electrostatically bound to a hole. Excitons are important to the electronic processes in organic semiconductors due to their characteristically low relative permittivity values. For example, a typical organic semiconductor may have relative permittivity $\epsilon_r \sim 3$ while for an inorganic material such as crystalline silicon $\epsilon_r = 12$. This implies that coulombic screening between charge carriers is less effective in organic semiconductors; as a result an excited electron can remain strongly bound to a hole and form a Frenkel exciton, which is usually located on a single molecule. The binding energy of excitons in organic semiconductors can be greater than approximately 0.5 eV with some dependence on the size of a molecule, or length of a polymer.[2]

A spin state of spin s has $2s + 1$ allowed values for the spin projection quantum number, m_s . Electrons have spin $s = \frac{1}{2}$ so have a multiplicity of two given by $m_s = \pm\frac{1}{2}$. Two bound electrons can form a state with total spin of either $s = 1$ or $s = 0$ depending on the relative orientations of the individual electrons. If we denote the single-electron spin eigenstates where $m_s = +\frac{1}{2}$ by α and $m_s = -\frac{1}{2}$ by β then there are a total of four possible two-electron spin eigenstates (as detailed in table 2.1) split between those states with $s = 1$, which have a

Table 2.1 Spin eigenstates of a two-electron system

Eigenstate	s	m_s
$\alpha_1\alpha_2$	1	1
$\frac{1}{\sqrt{2}}(\alpha_1\beta_2 + \beta_1\alpha_2)$	1	0
$\beta_1\beta_2$	1	-1
$\frac{1}{\sqrt{2}}(\alpha_1\beta_2 - \beta_1\alpha_2)$	0	0

multiplicity of three and consequently are described as triplets, and those states with $s = 0$ which have a multiplicity of one and are consequently described as singlets.

Assuming non-degenerate molecular orbitals, then due to the Pauli exclusion principle the ground state will have no overall spin — being composed of a pair of electrons with opposite m_s — and is therefore a spin singlet state. Diradicals — in which two unpaired electrons may occupy degenerate orbitals in the ground state — may have triplet ground states, but are not studied in this thesis. However, it is interesting to note that the oxygen molecule is a diradical with a triplet ground state and hence can cause quenching of triplet excited states in organic semiconductors.

In the case of excitons, the two electrons occupy different orbitals and hence may have either equal or opposite m_s . The spin state of the exciton is determined by the total spin of the excited electron in the LUMO and the remaining unpaired electron in the HOMO. This produces four possible combinations: the singlet state with $s = 0$ and three triplet states with $s = 1$ and $m_s = -1, 0, +1$.

As a result of the electron exchange interaction, the lowest-energy triplet exciton state, T_1 , is always lower in energy than the lowest-energy singlet exciton state, S_1 . This has implications for the design and performance of organic photovoltaics (as discussed in section 2.5.1 and chapter 6). Due to conservation of angular momentum, singlet excitons are radiatively coupled to the singlet ground state. However, the transition from a triplet exciton to the singlet ground state is spin-forbidden. This spin dependence is of importance to the design and performance of organic light-emitting diodes as discussed in section 2.5.2 and chapters 4 and 5.

The electron exchange energy (J) is given by the exchange integral in equation 2.1 and is a measure of the strength of the exchange interaction.[3] J depends on the spatial overlap of the electron wavefunctions in the HOMO and LUMO, ϕ_{HOMO} and ϕ_{LUMO} , with a smaller overlap resulting in a smaller exchange energy. \bar{r}_1 and \bar{r}_2 are position vectors.

$$J = \iint \phi_{HOMO}(\bar{r}_1)\phi_{LUMO}(\bar{r}_2)\frac{1}{|\bar{r}_2 - \bar{r}_1|}\phi_{HOMO}(\bar{r}_2)\phi_{LUMO}(\bar{r}_1)d\bar{r}_1d\bar{r}_2 \quad (2.1)$$

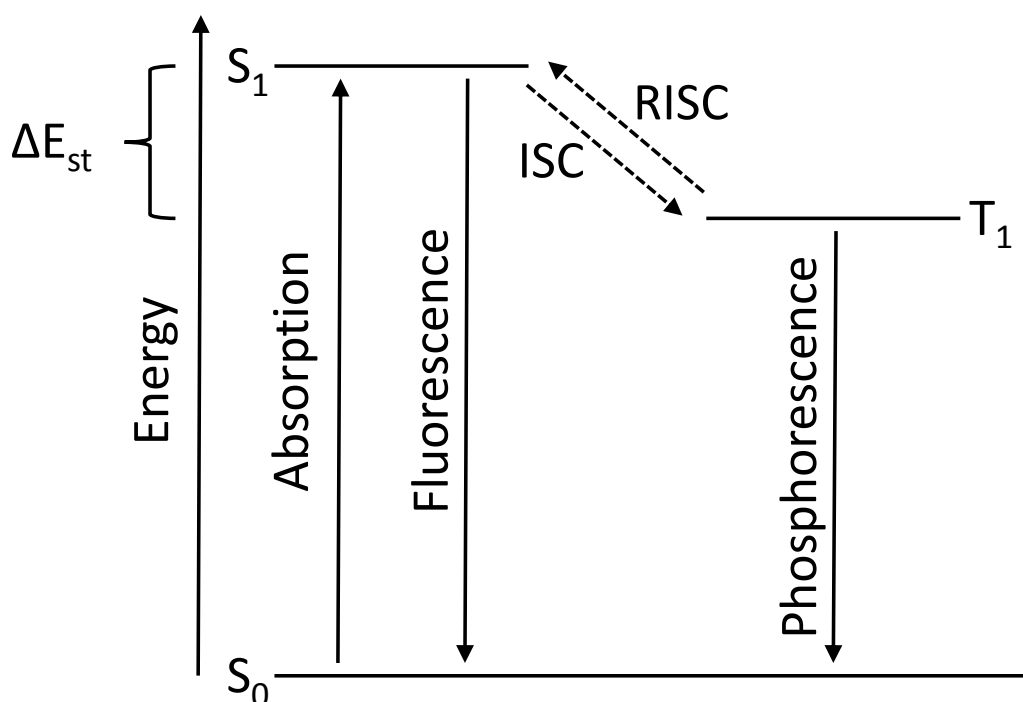


Fig. 2.1 State diagram indicating the ground state (S_0) and lowest energy singlet (S_1) and triplet (T_1) excitons. Radiative transitions are denoted by solid arrows and non-radiative transitions are denoted by dashed arrows. The vertical axis is potential energy while the horizontal axis has no physical meaning

The energy separation between S_1 and T_1 (ΔE_{ST}) can be approximated as $2J$. [4] It is therefore evident that reducing the overlap between HOMO and LUMO will lead to a reduction in the exchange integral and hence a lower ΔE_{ST} .

The positions of S_1 and T_1 with respect to the ground state (S_0) are shown in figure 2.1. Higher-lying exciton states, vibronic splitting and non-radiative decay processes have been omitted for simplicity. The radiative transitions of absorption, fluorescence and phosphorescence are represented by solid arrows while the non-radiative transition from S_1 to T_1 is indicated by a dashed arrow. Transitions from singlet to triplet states require a change in spin and are known as inter-system crossing (ISC). While technically also an ISC process, the transition from T_1 to S_1 is commonly referred to as reverse intersystem crossing (RISC) and this is the terminology adopted in this thesis. [5]

2.2.2 Charge-transfer states

Charge-transfer (CT) states are excited states in which an electron and a hole reside on different molecules (intermolecular CT states) or on different moieties in the same molecule

(intramolecular CT states), yet remain weakly coulombically bound. Similarly to excitons, CT states have four spin eigenstates. However, dissimilarly to excitons the exchange and dipolar interactions are much weaker in CT states and consequently the singlet and $m_s = 0$ triplet are not eigenstates, but instead form mixed states. The four spin eigenstates of a CT state, denoted as $|s, m_s\rangle$, are therefore given by

$$\begin{aligned}
 |1\rangle &= |1, +1\rangle \\
 |2\rangle &= \cos \psi |0, 0\rangle + \sin \psi |1, 0\rangle \\
 |3\rangle &= -\sin \psi |0, 0\rangle + \cos \psi |1, 0\rangle \\
 |4\rangle &= |1, -1\rangle,
 \end{aligned} \tag{2.2}$$

where ψ is the singlet-triplet mixing ratio.[6] CT states can be formed from a singlet exciton following photon absorption and are often an intermediate step to charge separation in OPV devices. In this case states $|2\rangle$ and $|3\rangle$ are exclusively populated due to spin selection rules and the CT state can also be described as a spin-correlated radical pair (SCRPs). SCRPs states and their influence on device function will be discussed in more detail in chapter 5 as part of the interpretation of electron spin resonance data.

CT states may also be formed by bimolecular recombination including following electrical injection in an OLED, in which case the charge pair will have uncorrelated spins. This has important implications for OLED efficiency and is discussed further in section 2.5.2. Intramolecular CT states can be formed in molecules with a donor-acceptor structure where there is a break in conjugation between the donor and acceptor moieties. This is of particular relevance to the discussion of thermally activated delayed fluorescence in section 2.3.3.

2.2.3 Polarons

A neutral molecule in the ground state can become charged through either the loss or gain of an electron, known as oxidation or reduction respectively. This ionisation process can occur by injection of charges from electrodes, such as in an OLED device, or by charge separation of a neutral exciton state, as happens during OPV operation. The minimum energy configuration of molecular nuclei following ionisation may be different to that of the neutral molecule. Hence a geometric distortion may take place following ionisation with variations in bond lengths and bond angles in comparison to the neutral molecule. As a charge is transferred from an initially ionised molecule, m_1 , to an initially neutral molecule, m_2 , then the geometry of m_1 will relax to the ground state configuration while m_2 will adopt the ionised configuration. The distorted geometry associated with ionisation is therefore transported through a film along with the charge. The combination of charge and distorted

geometry can therefore be treated as an excited state known as a polaron with a binding energy due to the energy associated with the molecular reorganisation. It is noted that the term polaron has historically been used to describe the distortion of a crystal lattice due to the presence of a charged species, but that the use of the term has broadened to include intra-molecular geometric distortions as described here.[7]

2.3 Absorption and emission of light

In an organic semiconductor absorption of a photon results in the promotion of an electron from a lower-lying occupied orbital to a higher-lying unoccupied orbital across the HOMO-LUMO energy gap. For absorption to occur it is therefore necessary for the photon energy to be greater than or equal to the HOMO-LUMO energy gap and for there to be wavefunction overlap between the ground state and the excited state. Due to the large difference in mass between an electron and a nucleus it is usually assumed that electron dynamics in absorption and emission events are much faster than nuclear motion. This is known as the Born-Oppenheimer approximation and can be directly related to the commonly observed red-shift between absorption and emission spectra, known as the Stokes shift. An electron can be assumed to absorb a photon in a fixed nuclear geometry. The molecule will then geometrically relax to find the lowest energy of the excited state with respect to the ground state. If a photon is subsequently emitted with relaxation of the molecule back to the ground state it will therefore be red-shifted in comparison to the photon which was originally absorbed.

2.3.1 Fluorescence

Fluorescence is the radiative relaxation of an excited state to the ground state of the same spin multiplicity. As discussed, organic materials will usually have a singlet ground state. Therefore fluorescence is a process associated with relaxation of singlet excitons to the ground state. Fluorescence is a spin-allowed transition and can therefore happen relatively quickly, on timescales of nanoseconds or less.

2.3.2 Phosphorescence

Similarly to fluorescence, phosphorescence is a radiative relaxation of an excited state to the ground state. However the defining feature of phosphorescent transitions is a change in spin multiplicity between a triplet exciton and the singlet ground state. Due to the change in spin, phosphorescence can only happen through the process of spin-orbit coupling whereby the singlet and triplet spin states become mixed through interaction with orbital

angular momentum. The spin-orbit coupling Hamiltonian, \hat{H}_{SOC} , for a single electron can be expressed as

$$\hat{H}_{SOC} = \frac{Zq^2}{2m^2c^2r^3} \hat{L} \cdot \hat{S} \quad (2.3)$$

where Z is the atomic number, q and m are the charge and mass of an electron, c is the speed of light in vacuum and \hat{L} and \hat{S} are the orbital angular momentum and spin operators. Due to the Z^3 dependence of the expectation value $\langle r^{-3} \rangle$ in a hydrogenic atom the spin-orbit coupling strength has an overall Z^4 dependence.[8] Phosphorescence is therefore strongest in the presence of heavy nuclei, and is often a negligible contribution to total luminescence for purely organic molecules. However it can be significant in organometallic compounds where the presence of metal nuclei can increase the spin-orbit coupling strength. Due to the requirement of a change in spin, phosphorescence is relatively slow in comparison to fluorescence and can happen on a timescale of microseconds, milliseconds or longer.

2.3.3 Thermally Activated Delayed Fluorescence

The rate of RISC, k_{RISC} , is dependent on both ΔE_{ST} and temperature, T , according to the Arrhenius-type relationship

$$k_{RISC} \propto \exp\left(\frac{\Delta E_{ST}}{k_B T}\right), \quad (2.4)$$

where k_B is the Boltzmann constant.[9] In the case of a weak electron exchange interaction for an excitonic state — for example due to a small overlap between the HOMO and LUMO wavefunctions in equation 2.1 — it is feasible for ΔE_{ST} to approach room-temperature thermal energy. On photoexcitation, the initially generated singlet excitons will display prompt fluorescence within a few nanoseconds but will also undergo intersystem crossing to populate triplet states. When ΔE_{ST} is small enough to be on the order of the available thermal energy it is possible to observe an appreciable rate of RISC and repopulate the singlet state from the triplet reservoir with subsequent fluorescent emission from S_1 . This process has historically been referred to as e-type delayed fluorescence following its observation in the molecule eosin.[10] However the term thermally activated delayed fluorescence (TADF) is more commonly used in the field of organic electronics and will be adopted in this thesis.

The separation of HOMO and LUMO electron wavefunctions necessary for TADF can be achieved through molecular design. Molecular geometry such as a torsion can be used to break the conjugation between donor and acceptor subunits and avoid wavefunction overlap between the HOMO and LUMO. As a result the exchange interaction will be weakened and the excited state formed between the HOMO and LUMO will have intramolecular CT character. In these cases ΔE_{ST} may be reduced to ≤ 100 meV to enable TADF emission.

Similarly to prompt fluorescence, TADF emission comes from the transition between the S_1 and S_0 state with the consequence that delayed and prompt emission have very similar spectra, albeit with the possibility of a red-shift over time due to molecular relaxation or exciton migration to lower energy sites. TADF can therefore be identified by the spectral similarity between prompt and delayed emission. Additionally, an activation energy can be extracted from the temperature dependence of photoluminescence decay fitted to an Arrhenius function as shown in equation 2.4.

The exact mechanism by which ISC or RISC occurs in TADF materials has been the subject of much discussion in the literature. According to El-Sayed's rule it is necessary for one of the unpaired electrons in an exciton to change orbital angular momentum during an ISC or RISC transition.[11, 12] This is to conserve total angular momentum despite the change in spin. El-Sayed's rule has led to the suggestion that ISC can be achieved by vibronic coupling between the intramolecular triplet CT state (3CT) and a local triplet exciton state (3LE) in which one of the electrons is located in a non-bonding orbital.[13, 14] One implication of this spin-vibronic model is that, in addition to ΔE_{ST} , the energy gaps between 3LE and 3CT and 3LE and 1CT also represent relevant activation energies for TADF emission. It is also implied that the level of vibronic coupling between CT and LE states can determine the efficiency of ISC processes. Due to the spatial separation of electron and hole wavefunctions the energy of a CT state is dependent on electrostatic interactions with the surrounding molecular environment, whereas this is not the case for LE states. Consequently the energy separation and even ordering between CT and LE states can be tuned through control of the polarity of host materials.[15] A key piece of supporting evidence for the spin-vibronic model is a study in which the photoluminescence properties of a TADF material were measured in regimes where the CT energy was less than, approximately equal to, and greater than the 3LE state energy. It was found that the photoluminescence intensity and the ratio of delayed fluorescence to prompt fluorescence were maximised when the CT and 3LE energies were approximately equal. However a minimisation of the characteristic decay time of the delayed fluorescence may also be expected when the CT and 3LE states are resonant, but this was not observed. Evidence for the importance of vibronic coupling has been shown by a study of a series of similar molecules with varying degrees of conformational flexibility. When alkyl groups of varying size were substituted onto the donor moiety of a TADF material, nominally to restrict vibrational motion, it was found that the rate of TADF could be suppressed. However, while a limited effect of the alkyl group substitutions on ΔE_{ST} and a large influence over vibrational modes were central to the argument, neither were experimentally verified.[16] Interesting insights can be made between similar molecules with approximately equal ΔE_{ST} values which display a variation in their TADF behaviour. For

example in a series of materials which differ only in the number and position of carbazole groups around a central benzonitrile it was found that TADF behaviour was suppressed by molecular deformation between the S_1 and T_1 excited states.[17] This suggests that molecular reorganisation can create an energetic barrier to intersystem crossing in the case of low ΔE_{ST} . The same group of materials have been found to display a variation in the formation of intramolecular intervalence CT states which correlate with TADF performance.[18] These intervalence CT states are formed by an electronic coupling between ionised and neutral moieties on the same molecule, for example through the delocalisation of cation charge between two or more carbazole groups.[19]

Conversely it has also been found that excitonic states in donor-acceptor type molecules can have a strongly mixed CT/LE character and that this can contribute to high ISC and RISC rates for El-Sayed forbidden transitions without the need to invoke intermediate transitions between discrete states. [20–22] Theoretical work on two carbazolyl dicyanobenzene TADF materials suggested that while excited states had a mixed CT/LE character it is also the case that both ΔE_{ST} and the spin-orbit coupling matrix elements vary with molecular conformation.[20] It was found that the torsional angle between the central benzonitrile group and peripheral carbazoles could vary between approximately 60° and 90° and that dynamic torsional variation was significant on the timescales of RISC. Vibrational motion is therefore thought to be important to TADF even in cases of mixed CT/LE excited states. However, paradoxically for TADF, it was also found that the torsional angles at which ΔE_{ST} is minimised are coincident with minimisation of spin-orbit coupling matrix elements.

2.4 Spin interactions

As discussed in section 2.2.1 electrons are spin $s = \frac{1}{2}$ particles and can form excitons in either a $s = 0$ (singlet) or $s = 1$ (triplet) state. The spin of an electron or exciton can interact with an external magnetic field or with other spins. The interactions which will be outlined in this section cause energy splitting which can be detected spectroscopically — for example using electron spin resonance (section 3.10) — to reveal information about excited state formation and dynamics in organic semiconductors.

The background theory on spin interactions and electron spin resonance presented here has been summarised from the books by Weil and Bolton [23] and Atherton [24] and the review article by Richert, Tait and Timmel [25].

2.4.1 Zeeman splitting

By virtue of its non-zero spin an electron possesses a magnetic moment, which interacts with any external magnetic fields. The quantum mechanical magnetic moment operator, $\hat{\mu}$, is related to the electron spin operator, \hat{S} by equation 2.5.

$$\hat{\mu} = -g\mu_B\hat{S} \quad (2.5)$$

where μ_B is the Bohr magneton, being the magnetic moment expected per \hbar unit of angular momentum. g is a dimensionless quantity known as the g -factor which is derived from relativistic quantum mechanics and for a free electron takes the scalar value 2.0023. If the direction of an externally applied magnetic field, B_0 , is used to define the z-axis then the energy of a spin with z-component m_s is given by equation 2.6.

$$E = g\mu_B m_s B_0 \quad (2.6)$$

There is therefore a magnetic field dependent energy splitting between states with different m_s values, for example between electrons with $m_s = \pm\frac{1}{2}$ and between the three triplet sublevels with $m_s = -1, 0, 1$. This splitting is the Zeeman interaction and analogously to equation 2.6 can be described by the Hamiltonian \hat{H}_z as shown in equation 2.7.

$$\hat{H}_z = g\mu_B\hat{S}_z \cdot \vec{B} \quad (2.7)$$

Electrons in molecules may be subject to spin-orbit coupling, especially when heavy atoms are present. For electrons in molecules the g -factor can deviate from the free electron value and can be anisotropic depending on molecular environment.

2.4.2 Hyperfine splitting

Nuclei with non-zero spin, such as ^1H ($s = \frac{1}{2}$) also have a magnetic dipole moment so will contribute to the magnetic field experienced by nearby electrons. In an external magnetic field, B_0 , a nucleus of spin I populates $2I + 1$ energy levels. The magnetic field experienced by electrons is therefore split into $2I + 1$ sublevels. The energy levels occupied by electrons ($s = \frac{1}{2}$) in the vicinity of a ^1H nucleus ($s = \frac{1}{2}$) will therefore be split into 4 different sublevels. This is known as hyperfine splitting and has contributions from both an isotropic and an anisotropic component.

The dipole-dipole interaction between electronic and nuclear magnetic dipole moments is the origin of anisotropic hyperfine splitting. The Hamiltonian for the dipole-dipole interaction

is given in equation 2.8

$$\hat{H}_{dd} = a \left(\frac{\hat{s} \cdot \hat{I}}{r^3} - \frac{3(\hat{s} \cdot \bar{r})(\hat{I} \cdot \bar{r})}{r^5} \right), \quad (2.8)$$

where $a = -\frac{\mu_0}{4\pi} g_e g_N \mu_B \mu_N$ with g_e and g_N the g -factors relating to the electron and nucleus respectively and μ_N the nuclear magneton. \hat{I} is the nuclear spin operator; \bar{r} is the spatial vector between the nucleus and electron and has magnitude r .

Due to spherical symmetry electrons in s-orbitals do not contribute to anisotropic hyperfine splitting. However an s-orbital has a finite probability density at the nucleus and so is subject to the Fermi contact interaction which contributes to isotropic hyperfine splitting. The Hamiltonian for the isotropic hyperfine interaction is given by equation 2.9

$$\hat{H}_{fc} = a \hat{S} \cdot \hat{I}, \quad (2.9)$$

where a is the coupling constant and is directly proportional to the probability density of the s-orbital at the nucleus.

2.4.3 Zero-field splitting

Within a triplet ($s = 1$) state there are two possible transitions where $\Delta m_s = 1$, namely between the $m_s = -1$ and the $m_s = 0$ substates and between the $m_s = 0$ and $m_s = +1$ substates. Equation 2.6 suggests that the energy of these transitions would be equal, depending only on the magnetic field B_0 , and that at zero-field ($B_0 = 0$) the three triplet sublevels would be degenerate. However dipole-dipole interactions between the two electrons in the triplet exciton lift the degeneracy and cause a zero-field splitting between triplet sublevels. Equation 2.8 can be reformulated to give the zero-field splitting caused by the dipole-dipole interaction between two electrons as in equation 2.10

$$\hat{H}_{zfs} = g_1 g_2 \mu_B^2 \frac{\mu_0}{4\pi} \left(\frac{\hat{s}_1 \cdot \hat{s}_2}{r^3} - \frac{3(\hat{s}_1 \cdot \bar{r})(\hat{s}_2 \cdot \bar{r})}{r^5} \right). \quad (2.10)$$

\hat{H}_{zfs} can also be represented in terms of the total spin operator, \hat{S} , and the zero-field splitting tensor, \mathbf{D} , as in equation 2.11

$$\hat{H}_{zfs} = \hat{S} \cdot \mathbf{D} \cdot \hat{S} = D \left(\hat{S}_z^2 - \frac{\hat{S}^2}{3} \right) + \frac{1}{2} E \left(\hat{S}_+^2 + \hat{S}_-^2 \right) \quad (2.11)$$

where \widehat{S}_+ and \widehat{S}_- are the spin ladder operators. D and E are the parameters which characterise the zero-field splitting and are related to the principal values of the \mathbf{D} tensor as

$$D = \frac{3}{2}D_z \qquad E = \frac{1}{2}(D_x - D_y) \qquad (2.12)$$

Conventionally the principal axes of the \mathbf{D} tensor are labelled such that $|D| \geq 3|E|$ and the Z axis refers to the axis of maximum dipolar coupling. Due to zero-field splitting originating from the dipole-dipole interaction between the constituent electrons in a triplet exciton, the parameters D and E are also determined by the spatial geometry of the triplet state and can be expressed as

$$D = \frac{3}{4}g_1g_2\mu_B^2\frac{\mu_0}{4\pi}\left\langle\frac{1-3\cos^2\theta}{r^3}\right\rangle \qquad E = \frac{3}{4}g_1g_2\mu_B^2\frac{\mu_0}{4\pi}\left\langle\frac{y^2-x^2}{r^5}\right\rangle, \qquad (2.13)$$

where r is the magnitude of the inter-spin vector and θ is the angle between the inter-spin vector and the Z-axis of the \mathbf{D} tensor. Therefore if $3\cos^2\theta > 1$ then $D < 0$ and vice versa. The sign of D can be used to determine if the spin distribution is oblate (positive D) or prolate (negative D) in the principal axis system.

When $B_0 = 0$, m_s becomes a poorly defined quantum number and the triplet energy levels are better described by the eigenstates of the \mathbf{D} tensor $|X\rangle$, $|Y\rangle$ and $|Z\rangle$, where X , Y and Z refer to the principal axis system of the \mathbf{D} tensor. The energies of the zero-field states, U_i , are given by

$$U_X = \frac{1}{3}D - E \qquad U_Y = \frac{1}{3}D + E \qquad U_Z = -\frac{2}{3}D. \qquad (2.14)$$

It can therefore be seen that the energetic splitting and the ordering of zero-field triplet substates depends on the relative magnitudes and signs of D and E .

2.4.4 Electron Spin Resonance

In the case where $B_0 > 0$ the Hamiltonian can be expressed as the sum of the zero-field splitting and Zeeman Hamiltonians and in matrix form with the principal axes of \mathbf{D} forming the basis as

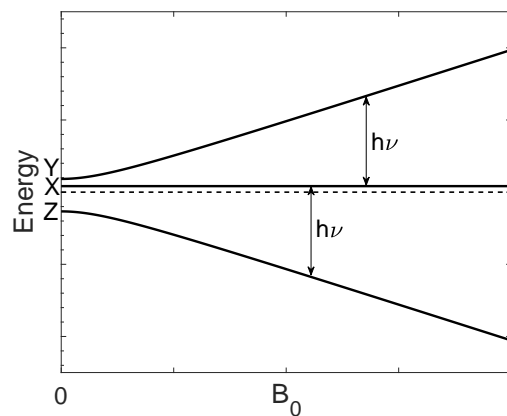
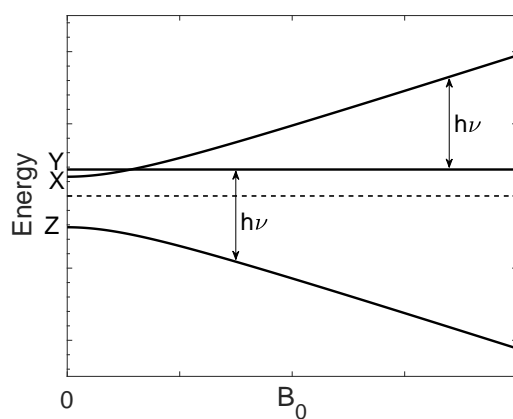
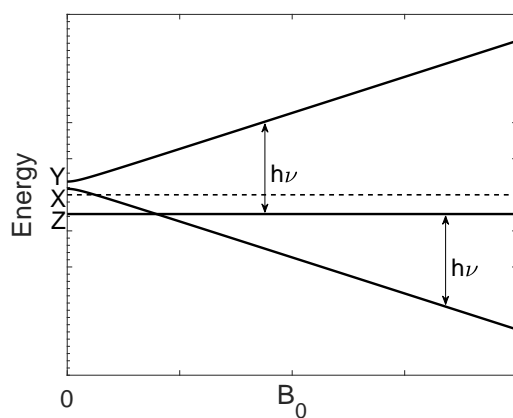
$$\widehat{H} = \widehat{H}_z f s + \widehat{H}_z = \begin{bmatrix} \frac{1}{3}D - E & g\mu_B B_0 l_Z & -ig\mu_B B_0 l_Y \\ g\mu_B B_0 l_Z & \frac{1}{3}D + E & g\mu_B B_0 l_X \\ ig\mu_B B_0 l_Y & g\mu_B B_0 l_X & -\frac{2}{3}D \end{bmatrix} \qquad (2.15)$$

where l_X , l_Y and l_Z are the direction cosines relating to the angles between B_0 and each of the X , Y and Z axes. The energy splitting between triplet sublevels is therefore determined by the Zeeman interaction, zero-field splitting and the relative alignment of B_0 with the axes of the \mathbf{D} tensor. In the case where B_0 is aligned with one of the principal axes the eigenvalues and hence the triplet energies can be found. For example when B_0 is parallel to Z then $l_X = l_Y = 0$, $l_Z = 1$ and the triplet energies become

$$\begin{aligned} U_{+1} &= \frac{1}{3}D + \sqrt{E^2 + (g\mu_B B_0)^2} \\ U_0 &= -\frac{2}{3}D \\ U_{-1} &= \frac{1}{3}D - \sqrt{E^2 + (g\mu_B B_0)^2}. \end{aligned} \quad (2.16)$$

The energy splitting between triplet sublevels as a function of B_0 is shown in figure 2.2 for each case of the canonical orientations of B_0 . In the case where $B_0 > 0$, m_s becomes a good quantum number and the triplets populate the states $|-1\rangle$, $|0\rangle$ and $|+1\rangle$ defined by $m_s = -1, 0, +1$. It is evident that photons of energy $h\nu$ will induce $\Delta m_s = 1$ transitions between the $|-1\rangle$ and $|0\rangle$ and the $|0\rangle$ and $|+1\rangle$ states at specific values of B_0 . This constitutes the basis of electron spin resonance (ESR) spectroscopy of triplet states.

In an ESR experiment the sample is held in a resonator which is critically coupled to a microwave source at fixed frequency. The resonator is located between the poles of an electromagnet which provides the B_0 field. Laser excitation is used to create excited states in the sample. In an organic semiconductor the initial excited states will be singlet excitons. Over time these will decay radiatively and non-radiatively and also undergo intersystem crossing to produce a population of triplet excitons. As the B_0 field is swept the energy of the triplet sub-states will vary as shown in figure 2.2. A resonance condition occurs at the B_0 field values at which the energy splitting between $|-1\rangle$ and $|0\rangle$ or $|0\rangle$ and $|+1\rangle$ is equal to the microwave photon energy $h\nu$. If there are non-equal populations of the triplet sub-states then ESR transitions can be detected at these B_0 values. It is possible to detect both emissive and absorptive transitions depending on the relative populations of the sub-states. Different mechanisms of intersystem crossing produce different population distributions of the triplet sub-states and hence characteristic patterns of absorption and emission. By observing the features in an ESR spectrum the mechanism of intersystem crossing in a sample can therefore be identified. Additionally the separation between features can lead to the determination of the zero-field splitting parameters D and E .

(a) $B_0 \parallel X$ (b) $B_0 \parallel Y$ (c) $B_0 \parallel Z$ Fig. 2.2 Triplet substate energies as a function of B_0 with varying orientation of B_0

In a frozen solution or disordered solid film the molecules in the sample will form a distribution of orientations of the \mathbf{D} tensor with B_0 . As a result the measured spectrum

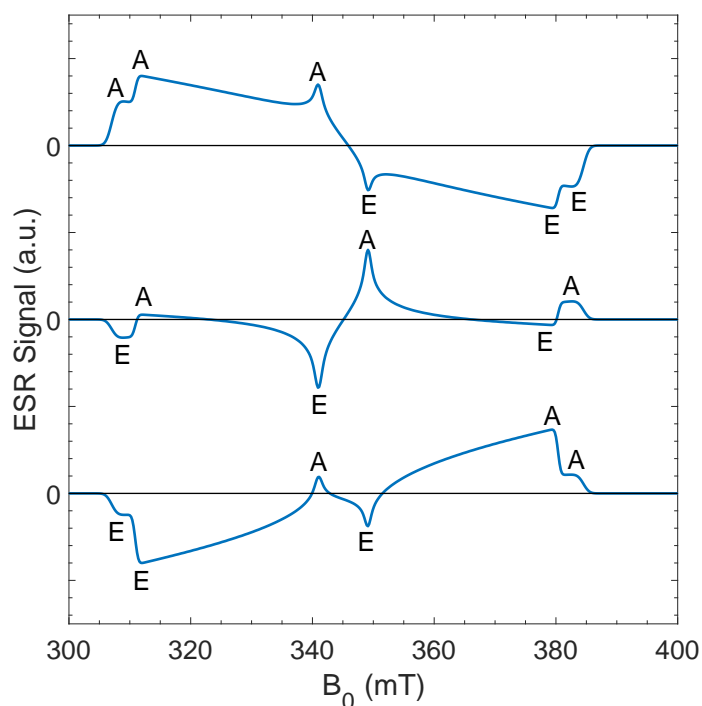


Fig. 2.3 Simulated triplet ESR spectra ($D > 0$) displaying varying absorption-emission patterns according to preferential population of $|X\rangle$ (bottom), $|Y\rangle$ (middle) or $|Z\rangle$ (top). Absorptive (A) and emissive (E) transitions are labelled

will represent a sum over all the orientations and contain six turning points corresponding to absorptive and emissive transitions between $|-1\rangle$ or $|+1\rangle$ and $|0\rangle$ at each of the three canonical orientations. The ESR spectrum can then be described by a six letter combination of A (for absorption) and E (for emission) as the spectrum is scanned from low to high field. Spectra from a triplet state with $D > 0$ are shown in figure 2.3. It can be seen that the pattern of absorption and emission depends on relative triplet sublevel populations. Preferential population in the $|X\rangle$ substate leads to an EEAEEA pattern in comparison to an EAEAEA or AAEEEE pattern from preferential population of the $|Y\rangle$ or $|Z\rangle$ states.

2.5 Organic optoelectronic devices

Organic semiconductors can be incorporated into devices by making connections to electrodes for the purpose of injection or extraction of charge. Organic optoelectronic devices, namely organic photovoltaics (OPV) and organic light-emitting diodes (OLEDs), are typically fabricated in a layered stack with the organic semiconductor layers sandwiched between the

two electrodes. Given that the absorption or emission of light is fundamental to the operation of OPV and OLED devices it is important that at least one electrode is transparent. For this reason devices are often fabricated on glass substrates which have been coated with indium-tin-oxide (ITO), a transparent conductive oxide.

2.5.1 Organic photovoltaics

Organic photovoltaics (OPVs) can be used for energy conversion from incident solar photons to electrical energy. They therefore have the potential to contribute to electrical energy generation while avoiding harmful greenhouse gas emissions. OPV devices have been investigated since the 1970s although initial studies into acenes, phthalocyanines and chlorophyll yielded low power conversion efficiencies of $10^{-3}\%$ or less.[26–29] Modern day OPVs still typically show lower power conversion efficiencies than established inorganic materials such as silicon, but record efficiencies have been increasing rapidly in research environments from 5.4% in 2008 to greater than 13% in 2018 for single-junction devices.[30–35]

As discussed, the low relative permittivity of organic semiconductors results in a charge-neutral exciton being produced following absorption of an incident photon. For a device to work the exciton must be separated into free charges and those charges need to be extracted at the electrodes. Charge separation is usually achieved at the interface between two organic semiconductor materials with offset frontier molecular orbital energies. A type II heterojunction is formed at the interface as shown in figure 2.4. The materials composing the type II heterojunction are chosen to have offset HOMO and LUMO levels so that it is energetically favourable for an excited electron in the LUMO of the electron-donor to move across the junction into the LUMO of the electron-acceptor. Similarly a hole can move from the acceptor HOMO to donor HOMO. In either case the electron and hole will form an interfacial CT state which is an intermediate state to the formation of free charges. The two materials forming the heterojunction will also often have different HOMO-LUMO gaps so that charge transfer is favoured over energy transfer at the interface.[36] A bulk heterojunction structure — in which the donor and acceptor materials are intimately mixed — is usually employed to reduce the distance between excitation sites and the heterojunction to within the diffusion length of excitons, which can typically be approximately 10 nm.[37] Assisted by the built-in field created by the difference in work function between the two electrodes, the electron is then transported through the acceptor material to the cathode while the hole is transported through the donor material to the anode. It should be noted that the optimum operation of a bulk heterojunction structure is highly morphology dependent; the domain sizes of each constituent material cannot be large in comparison to the exciton diffusion length and continuous percolation pathways must exist for charges to reach the

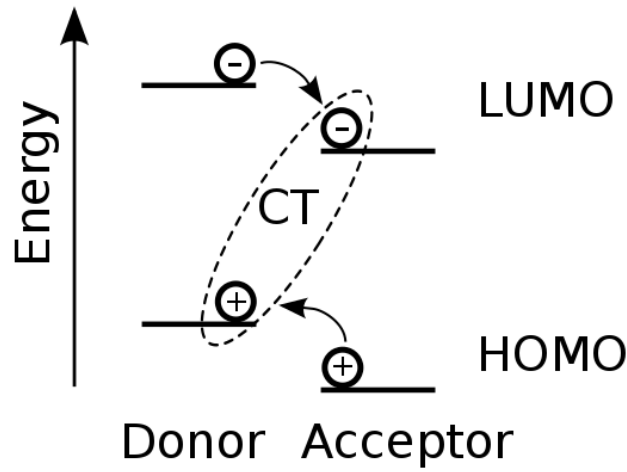


Fig. 2.4 Offset HOMO and LUMO levels between donor and acceptor materials in a type II heterojunction

electrodes. The power conversion efficiency (η_{PCE}) of OPVs is given by

$$\eta_{PCE} = \frac{J_{SC}V_{OC}F_F}{P_{in}}, \quad (2.17)$$

where J_{SC} is the short-circuit photocurrent, V_{OC} is the open-circuit voltage and P_{in} is the incident power density. F_F is the fill-factor and is the ratio of maximum electrical power out to the product $J_{SC}V_{OC}$.

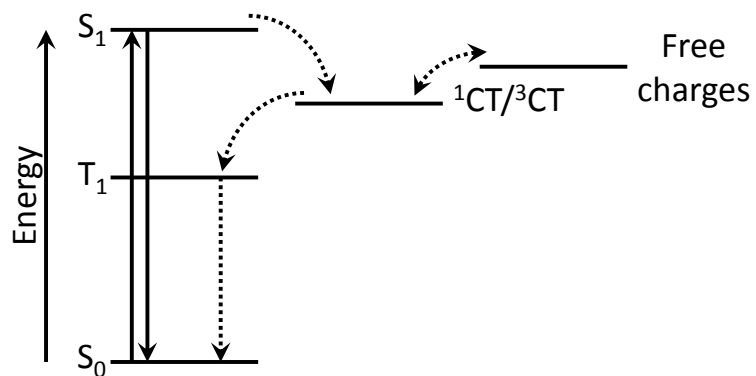
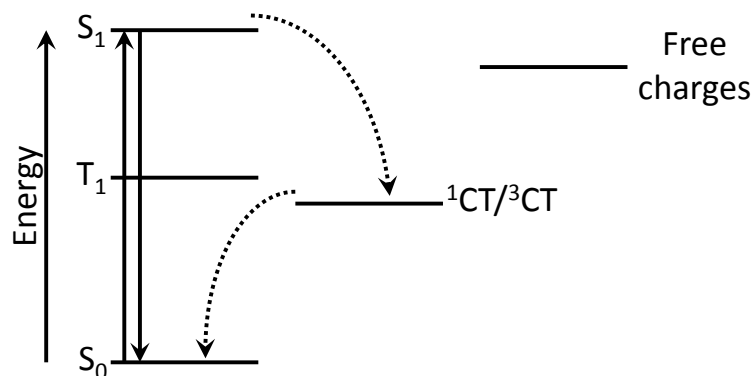
It has previously been observed that the V_{OC} of OPVs has been systematically lower than qE_g (where q is the charge of an electron and E_g is the energy of optical absorption onset) with V_{OC} loss typically greater than 0.6 V.[38, 39] This V_{OC} loss compares poorly with silicon, perovskite and other inorganic photovoltaic materials and limits the achievable η_{PCE} in OPV.[40] V_{OC} loss can be split between a number of identifiable contributions including: the offset in energy between donor and acceptor frontier orbitals, which is necessary to overcome exciton binding energy; CT state binding energy; and charge recombination.[41, 42] Of these, this thesis will focus on the loss due to charge recombination, in which excited states return to the ground state without the collection of charge at the electrodes. In a photovoltaic device the open-circuit condition occurs when the photocurrent is balanced by an opposing recombination current so that the overall current through the device is zero. For an ideal diode the V_{OC} is a function of both J_{SC} and the recombination parameter J_0 , which also has

dimensions of current density.[43]

$$V_{OC} = \frac{k_B T}{q} \left(\frac{J_{SC}}{J_0} + 1 \right) \quad (2.18)$$

A reduction in recombination processes leads to a smaller J_0 and hence a lower V_{OC} loss and larger η_{PCE} . As is noted in the famous detailed balance analysis by Shockley and Queisser the existence of radiative recombination is an unavoidable loss as it represents the reverse process of optical absorption.[44] However non-radiative recombination is a potentially avoidable loss pathway.

In π -conjugated polymers typically used as donors in OPV blends the T_1 energy may be 0.7 eV lower than the S_1 energy.[45] This creates a problem in OPV devices whereby maximising the CT state energy to avoid excess energy loss in charge separation makes it energetically favourable to access the molecular T_1 state. As shown in figure 2.5a this constitutes a loss pathway as there are no energetically favourable mechanisms by which the T_1 state can re-populate the CT state or separate to produce free charges.[46, 47] Any T_1 excitons produced are therefore destined to recombine non-radiatively and not contribute to electrical power extracted from the OPV device. Figure 2.5b illustrates an alternative arrangement where the CT state energy is lowered to be below T_1 . However, excess energy will be lost in the formation of a low-lying CT state, and further charge separation may be suppressed by the CT state stabilisation. An approach to avoiding this triplet-based loss pathway explored in chapter 6 is to use TADF emitters in OPV blends. As shown in the state diagram in figure 2.5c, the low ΔE_{ST} values of TADF materials means that the T_1 energy can be raised above the CT state energy making it energetically favourable to enter the CT state where charges may subsequently separate. In these systems the T_1 state is therefore no longer a terminal loss pathway.

(a) low-lying T_1 state

(b) low-lying CT state

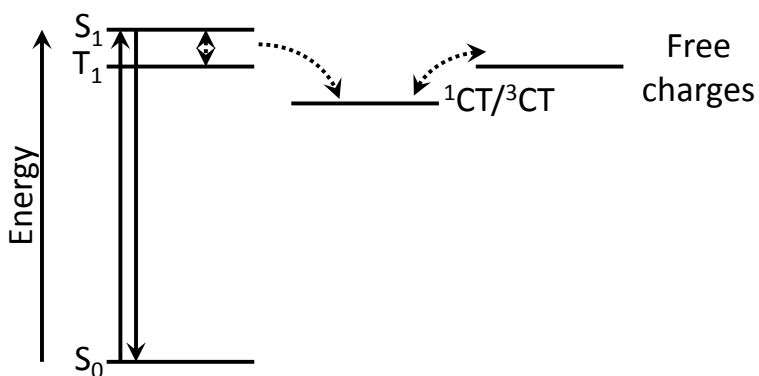
(c) high-lying T_1 state

Fig. 2.5 State diagrams representing OPV heterojunction blends with a) exothermic transfer to and subsequent non-radiative recombination from a low-lying T_1 state b) exothermic transfer to and subsequent non-radiative recombination from a low-lying CT state and c) an OPV blend incorporating low- ΔE_{ST} materials avoiding non-radiative end states

2.5.2 Organic light-emitting diodes

Organic light-emitting diodes (OLEDs) have been studied for over 30 years and can be used for the conversion of electrical energy to emitted light either for the purpose of displays or large-area lighting.[48] OLEDs function by injecting opposite charges — holes from the anode and electrons from the cathode — into an emitting material where they will radiatively recombine.

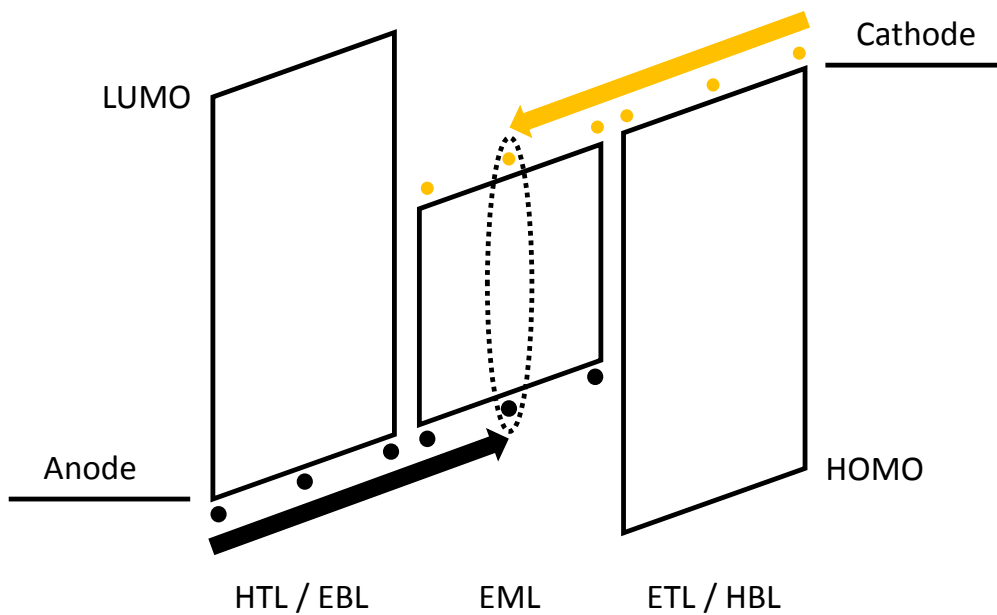


Fig. 2.6 An idealised OLED architecture under forward bias. Electron current is depicted in yellow and hole current is depicted in black.

The operation of an OLED is illustrated in the schematic device structure in figure 2.6. An electron current is injected from the cathode through the electron transport layer (ETL) and into the emissive layer (EML). Due to a large potential barrier at the interface with the electron blocking layer (EBL) the electrons become trapped in the EML. Likewise holes injected from the anode flow through the hole transport layer (HTL) and are trapped in the EML by a potential barrier at the interface with the hole blocking layer (HBL). Electroluminescence is achieved when an electron and a hole trapped in the EML form an exciton by their mutual coulombic attraction and recombine with the emission of a photon. The threshold applied bias, known as the turn-on voltage, V_{on} , at which electroluminescence is observed is determined by potential barriers at interfaces between adjacent organic layers or between the organic layers and electrodes which need to be overcome for charges to reach

the EML. It is noted that the definition of V_{on} can vary and is slightly arbitrary. In this thesis V_{on} will be defined as the applied bias at which light is emitted with a brightness of 1 cd m^{-2} as this can be measured easily and unambiguously.

When discussing OLEDs incorporating small-molecule emitting materials, the EML usually consists of a luminescent guest material dispersed in a wider HOMO-LUMO gap host. Charges may be transferred to the emissive guest molecules either directly from transport layers or following an intermediate transfer and transport through the host material. The wide HOMO-LUMO gap and consequent high exciton energies of the host material ensures that excitations remain confined on the emissive guest molecules. The guest concentration is typically low to avoid concentration dependent luminescence quenching effects often ascribed to non-radiative recombination at aggregate sites found through Förster or Dexter energy transfer mechanisms[49, 50].

The performance figure of merit often referred to in organic light-emitting diode research is the external quantum efficiency (η_{eqe}), which is the number of photons escaping the front surface per charge carrier flowing in the external circuit and is usually quoted as a percentage. η_{eqe} can be expressed according to equations 2.19 and 2.20.[51]

$$\eta_{eqe} = \eta_{oc}\eta_{iqe} \quad (2.19)$$

$$\eta_{eqe} = \eta_{oc}\gamma\chi\eta_{plqe} \quad (2.20)$$

Here η_{iqe} is the internal quantum efficiency which differs from η_{eqe} by the optical outcoupling efficiency, η_{oc} . η_{iqe} can in turn be expressed as the product of the charge carrier balance factor (γ), the proportion of excited species which are radiatively coupled to the ground state (χ) and the photoluminescence quantum efficiency of the emitting material (η_{plqe}).

For light to escape an OLED device in the desired forward direction it must cross refractive index boundaries at the interfaces between the organic semiconductor materials and the glass substrate and further between the glass substrate and air. Optical outcoupling losses are therefore incurred due to reflections at these boundaries and consequent waveguiding parallel to the substrate. Successful optical outcoupling is therefore only achieved by photons emitted within an angular escape cone. Further optical outcoupling losses are sustained at the interface of the organic layers with the conductive metal electrode which allows the formation of surface plasmon modes. The optical outcoupling efficiency is therefore determined by the dimensions of the optical cavity formed by the organic layer between the reflective metal electrode and the glass, the orientation of molecular dipoles and the consequent angular distribution of emission, and the refractive indices of the materials. This typically leads to optical outcoupling limits in the range 20-30%. [52, 53] Methods to improve the optical

outcoupling efficiency have not been investigated in this thesis but may include texturing the glass surface, using microlenses or using high refractive index glass.[54, 55]

When an electron and hole recombine following electrical excitation their spins are uncorrelated and hence the excitons are formed in a ratio of 1:3 singlets to triplets. As discussed in section 2.2.1 singlet excitons may radiatively recombine to the singlet ground state but triplet excitons are spin-forbidden from doing so. This places a limit of 25% on the internal quantum efficiency of fluorescent OLEDs since the factor χ in equation 2.20 will have a value of 0.25.

Much research effort has been invested into methods to induce luminescence from triplet excitons and hence increase the value of χ . In the case of phosphorescent materials spin-orbit coupling induced by the presence of a heavy metal such as platinum or iridium creates sufficient mixing of the triplet and singlet states to allow radiative coupling to the ground state from all electrically-pumped excitons and hence raises the theoretical maximum χ value to unity and hence the maximum η_{iqe} to 100%.[56, 57] Iridium complexes in particular have been shown to span a wide colour range including green, red and blue.[58–60] However a number of problems persist; despite commercial success in green and red emitters, blue phosphorescent OLEDs tend to suffer from poor stability, poor colour purity and lower η_{eqe} . [61, 62] One mechanism for the lower performance of blue phosphorescent OLEDs is that the incomplete d-orbital filling of iridium and platinum can lead to the formation of non-radiative metal-centred dd* states.[63] This is a problem for blue-emitting phosphorescent materials as the required activation energy to populate the dd* states from emissive triplet states is low in comparison to the same transition in green emitters. Additionally iridium is a rare element, which is a potential problem for long-term high-throughput industrial manufacture. Another approach to induce luminescence originating from triplet excitons is to use materials displaying TADF emission. The first reports of TADF emission in OLED devices came from organometallic complexes containing, for example, tin or copper.[64, 65] These were closely followed by the use of all-organic materials.[66] The field was brought to much wider attention by the publication of OLEDs based on carbazolyl dicyanobenzene derivatives spanning a wide colour range from orange to sky-blue.[67] The emission colour and device performance depended on the geometrical arrangement of the electron-donating carbazole moiety and the electron-accepting dicyanobenzene moiety and the addition of electron-donating or electron-withdrawing peripheral groups. The green-emitting material 2,4,5,6-Tetra(9H-carbazol-9-yl)isophthalonitrile (4CzIPN) in particular has subsequently come to be regarded as a prototypical TADF material with $\Delta E_{ST} = 83$ meV, $\eta_{plqe} = 94\%$ in solution and OLED devices with $\eta_{eqe} = 19.3\%$.

Fluorescence from singlet states can happen on nanosecond timescales however the timescale of TADF or heavy metal induced triplet phosphorescence is more like microseconds. This difference in emission rate leads to a higher steady-state population of excitations in TADF and phosphorescent emitters in comparison to purely fluorescent emitters at the same current density. As a result TADF and phosphorescent OLEDs are susceptible to triplet-triplet and triplet-polaron annihilation processes which cause η_{eqe} roll-off at high current density and also results in the formation of high-energy excitations which can cause material degradation, especially in blue emitters.[68–70]

While the peak η_{eqe} is an important performance metric for OLEDs it should be noted that η_{eqe} usually decreases at high current density, and hence high luminance. This is known as efficiency roll-off and is particularly detrimental for general lighting applications where luminances of greater than 1000 cd m^{-2} are required. Sources of efficiency roll-off include non-geminate annihilation processes between excitons or between an exciton and a polaron.[68] Efficiency roll-off is therefore likely to be a smaller effect in materials with higher radiative rates and consequently shorter excited state lifetimes. Additionally the charge-carrier balance factor, γ , may vary with applied field. This often leads to an initial rise in η_{eqe} at low current density due to variations between the energy barriers for electrons and holes.[71] There is no defined standard metric to quantify efficiency roll-off but the current-density or luminance measured at 90 % of peak η_{eqe} ($J_{90\%}$ or $L_{90\%}$) have been suggested as useful measures.[68] In this thesis $L_{90\%}$ will be used as the preferred measure of efficiency roll-off because the device luminance has a more direct relevance to light emission applications than the current density.

Chapter 3

Methods

3.1 Vacuum thermal evaporation

Small molecule organic semiconductors can be deposited as films through vacuum thermal evaporation. Substrates are loaded into a vacuum chamber at a distance of approximately 50 cm above crucibles containing organic material. The evaporation chamber is evacuated first by a rotary vane pump and then a helium cooled cryogenic pump which allows high vacuum (10^{-7} Torr) to be reached with short pumping times. The organic material is heated by passing electrical current through metal filaments surrounding the crucible. At temperatures in the approximate range 150°C-300°C, depending on molecular weight and inter-molecular interactions, the organic material will begin to either evaporate or sublime. The molecules diffuse through the evaporation chamber in a gas phase and form a solid film on the substrates, and any other surface on which they are incident. The substrates are rotated at 25 revolutions per minute to improve the uniformity of film thickness. The deposition rate is monitored using a quartz crystal microbalance which has been calibrated by measuring the achieved film thickness through ellipsometry. The deposition rate is controlled via a software based proportional-integral-derivative (PID) feedback controller which can adjust the power applied to the heating filaments. Blended films can be fabricated by the deposition of up to three materials simultaneously and multiple layer device stacks can be formed from sequential deposition of different materials. A selective shutter can be used to vary layer thickness or composition between substrates. Vacuum thermal evaporation typically produces uniform and smooth films but is not suitable for materials with high molecular weights or low thermal stability where the required evaporation temperature may be greater than the thermal degradation temperature.

Metals used as electrodes in devices such as calcium, aluminium, silver or gold and inorganic electrode interlayer materials such as lithium fluoride or molybdenum trioxide

can be evaporated by a similar method but from resistive boats made from tungsten or molybdenum as opposed to crucible sources. Individual pixel areas can be defined using a shadow mask in near-contact to the substrates. In this thesis a 7-source Angstrom Engineering EvoVac vacuum thermal evaporation system sited inside a glovebox has been used to prepare thin film samples, create multilayer device stacks and deposit metal electrodes.

3.2 Spin-coating

Spin-coating is a film deposition technique for soluble materials. Solutions are prepared in a N₂-filled glovebox typically at weight concentrations of 5-30 mg mL⁻¹. Approximately 40 μL of solution is then dropped onto a pre-cleaned borosilicate glass, ITO-patterned glass, or quartz substrate which is being spun at ~ 800 – 3000 revolutions per minute. Depending on the substrate surface energy and the solution surface tension, the solution will spread across the substrate surface. Centrifugal force created by the substrate rotation helps to ensure an even layer is created. As the solvent evaporates a solid film of the semiconductor material is deposited onto the substrate. The film thickness depends on a number of factors including the substrate rotation rate, solution viscosity and solvent evaporation rate.

Their ability to be deposited through solution-processing techniques has long been highlighted as an advantage of organic semiconductors as it may allow high-throughput roll-to-roll manufacture by inkjet printing. Additionally, it provides a viable deposition technique for semiconducting polymers and other high molecular weight or low degradation temperature materials which are otherwise unsuitable for vacuum thermal deposition. Conversely solution-processing is only possible with soluble materials which excludes many organic semiconductors which otherwise display interesting or useful electronic characteristics. Additionally, the vision of large-scale industrial solution processing raises questions regarding the control and disposal of waste solvents which may cause a hazard to human health and the environment.

3.3 Photovoltaic characterisation

OPVs are primarily characterised by a spectrally resolved measurement of the external quantum efficiency (η_{EQE}) and by measurement of the J - V curve to determine the power conversion efficiency η_{PCE} .

3.3.1 External quantum efficiency

The external quantum efficiency (η_{EQE}) of a photovoltaic device is defined as the ratio of charge carriers extracted at the electrodes to the number of incident photons. η_{EQE} is therefore related to the absorbance of a device in addition to the efficiency of charge generation and collection following photon absorption. The measurement of η_{EQE} is usually spectrally resolved which shows which wavelengths of incident light are efficiently converted to photocurrent by the test cell.

Light from a xenon arc lamp is transmitted through an Oriel Instruments 74000 monochromator and focused onto a calibrated silicon photodiode. The photodiode signal is recorded as the wavelength of incident light is scanned from 900 nm to 375 nm with steps every 5 nm. Using the known quantum efficiency of the calibrated photodiode the photon flux can be calculated at each wavelength. The calibrated photodiode is then replaced by the OPV cell under test and the photocurrent is recorded as a function of wavelength. η_{EQE} can then be calculated for each wavelength as the ratio of extracted photocurrent to the photon flux. The lamp is typically allowed to warm up and stabilise for approximately 15 minutes prior to measurement. To further reduce uncertainty which could be introduced by variation in lamp output between the calibrated photodiode and test cell measurements, a beam splitter is used to direct part of the beam onto a reference photodiode which is consistent between the two measurements.

3.3.2 Power conversion efficiency

The power conversion efficiency (η_{PCE}) of an OPV device is determined through the measurement of a current density-voltage (J-V) curve during irradiation from an ABET Technologies Sun 2000 solar simulator under 1-sun (100 mW cm^{-2}) conditions adjusted according to the spectral mismatch factor. The J-V characteristic is measured using a sensitive Keithley 2636A source-meter unit. The solar simulator consists of a xenon arc lamp which is filtered to approximate the standard AM1.5G solar spectrum. Prior to use, the solar simulator lamp is switched on and allowed to stabilise. Following this warm-up period, the solar simulator lamp current is adjusted so that the reading from a reference silicon photovoltaic cell (type RS-OD4, Czibula & Grundmann GmbH), being the photovoltage generated across an integrated high-precision resistor, is equivalent to 100 mW cm^{-2} . The incident power is further adjusted to account for the spectral mismatch factor, M , which is given by

$$M = \frac{\int_{\lambda_2}^{\lambda_1} E_{AM1.5G}(\lambda) S_{ref}(\lambda) d\lambda}{\int_{\lambda_2}^{\lambda_1} E_{AM1.5G}(\lambda) S_T(\lambda) d\lambda} \frac{\int_{\lambda_2}^{\lambda_1} E_{sim}(\lambda) S_T(\lambda) d\lambda}{\int_{\lambda_2}^{\lambda_1} E_{sim}(\lambda) S_{ref}(\lambda) d\lambda} \quad (3.1)$$

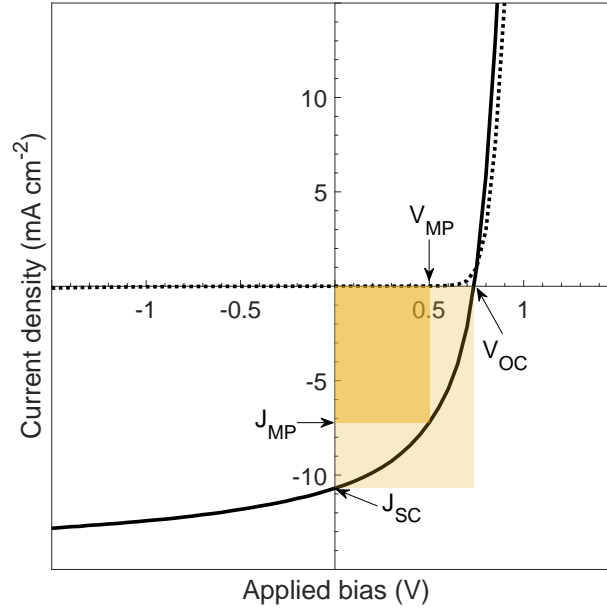


Fig. 3.1 Example J-V curve measured from a PCDTBT:PC₇₁BM OPV in the dark (dashed line) and under 1-sun solar simulator illumination (solid line). Short-circuit current density (J_{SC}), open-circuit voltage (V_{OC}) and maximum power point current-density (J_{MP}) and voltage (V_{MP}) are marked

where E is spectral irradiance and S is detector response. The subscripts *AM1.5G* and *sim* refer to the AM1.5G solar spectrum standard and the spectrum of the solar simulator used to test the devices. The subscripts *ref* and *T* refer to the reference silicon photovoltaic cell used to set the solar simulator power and the test cell respectively.[72] The spectral response of the test cell, $S_T(\lambda)$ is taken from the measured η_{EQE} as described in section 3.3.1.

η_{PCE} can be found from equation 3.3 following the evaluation of short-circuit photocurrent (J_{SC}), open-circuit voltage (V_{OC}) and fill-factor (F_F) from the J-V curve as illustrated in figure 3.1. Fill factor can be found from equation 3.2 where V_{MP} and J_{MP} are the voltage and current density at the maximum power point. It can be visualised as the ratio of the two shaded rectangles in figure 3.1. P is the incident power under 1-sun conditions multiplied by the device area.

$$F_F = \frac{J_{MP}V_{MP}}{J_{SC}V_{OC}} \quad (3.2)$$

$$\eta_{PCE} = \frac{J_{SC}V_{OC}F_F}{P} \quad (3.3)$$

3.4 Light-emitting diode characterisation

In this thesis, performance of an OLED is characterised by measurement of the electroluminescence spectrum and the subsequent determination of emission colour in the Commission Internationale de l'Éclairage (CIE) 1931 colour space [73] and by measurement of the current-density and luminance output of the device as a function of applied forward bias and the subsequent determination of V_{on} and η_{eqe} .

3.4.1 Electrical characterisation

The current flowing through a device is measured as a function of applied bias using a Keithley 2635 source-meter. The current-density is calculated by simply dividing the measured current by the pixel area of 4.5 mm^2 and is denoted by the letter J .

The on-axis photon flux per steradian (Φ_0) is calculated from measurement using a calibrated silicon photodiode positioned directly above the OLED and equation 3.4

$$\Phi_0 = \frac{V_{pd}}{\Omega C q R} \quad (3.4)$$

where V_{pd} is the voltage output of the photodiode connected through a transimpedance amplifier with feedback resistance $R = 1 \text{ M}\Omega$, q is the charge of an electron ($1.602 \times 10^{-19} \text{ C}$), Ω is the solid angle subtended by the circular 1 cm^2 photodiode at a distance of 15 cm from the OLED surface and C is the average quantum efficiency of the photodiode (η_{qe}) weighted over the incident electroluminescence spectrum in terms of photon intensity, p_{el} , and is found from equation 3.5

$$C = \frac{\int \eta_{qe}(\lambda) p_{el}(\lambda) d\lambda}{\int p_{el}(\lambda) d\lambda} \quad (3.5)$$

The angular emission of planar OLEDs with randomly orientated transition dipole moments is found to follow a Lambertian profile at angles θ to the normal as shown in equation 3.6.[74]

$$\Phi(\theta) = \Phi_0 \cos \theta \quad (3.6)$$

Therefore by integrating the photon emission over the hemisphere bounded by the device surface and dividing by the rate of electron injection, the η_{eqe} can be found from equation 3.7

$$\eta_{eqe} = \frac{\Phi_0 q \pi}{I} \quad (3.7)$$

where I is the electrical current flowing through the device.

How bright an OLED appears is described by the luminance, measured in units of cd m^{-2} . It is dependent on the overlap between the electroluminescence spectrum and the standard photopic luminosity function ($P(\lambda)$), which is analogous to the efficiency of the human eye as a function of wavelength, in units of lumens per watt. Similarly to equation 3.5 a quantity, K , can be defined as

$$K = \frac{\int P(\lambda) p_{el}(\lambda) \frac{hc}{\lambda} d\lambda}{\int p_{el}(\lambda) d\lambda}. \quad (3.8)$$

The luminance is then given by

$$L = \frac{\Phi_0 K}{a}, \quad (3.9)$$

where a is the device pixel area.

3.4.2 Spectral characterisation

Electroluminescence spectra were measured using either an Edinburgh Instruments FLS980 spectrometer or an Ocean Optics Flame mini-spectrometer. The CIE chromaticity coordinates (x, y) were then calculated from the colour matching functions $(\bar{x}, \bar{y}, \bar{z})$ via tristimulus values X, Y and Z as shown in equations 3.10-3.14, where $L_e(\lambda)$ is the spectral radiance as a function of wavelength of the electroluminescence.

$$X = \int_{380}^{789} L_e(\lambda) \bar{x}(\lambda) d\lambda \quad (3.10)$$

$$Y = \int_{380}^{789} L_e(\lambda) \bar{y}(\lambda) d\lambda \quad (3.11)$$

$$Z = \int_{380}^{789} L_e(\lambda) \bar{z}(\lambda) d\lambda \quad (3.12)$$

$$x = \frac{X}{(X + Y + Z)} \quad (3.13)$$

$$y = \frac{Y}{(X + Y + Z)} \quad (3.14)$$

3.5 Absorption

The absorption spectrum can reveal the energy and cross-section of transitions between electronic states, either from the ground-state to excited states in the case of steady-state measurement or between excited states in the case of transient absorption spectroscopy.

3.5.1 UV-Vis absorption

The steady-state absorption spectra of thin film samples can be measured in the ultra-violet and visible ranges using a transmission method. The sample absorbance is calculated by comparison of transmission of monochromated white light through a blank substrate (I_0) with the transmission through the film sample of thickness t (I_t) as a function of wavelength. The decadic absorbance, A , and if t is known the absorption coefficient, α , can be calculated using equations 3.15 and 3.16.

$$A = \log_{10} \left(\frac{\Phi_0}{\Phi_t} \right) \quad (3.15)$$

$$\alpha = \left(\frac{A}{t} \right) \ln(10) \quad (3.16)$$

Solution measurements can be made in a 1 mm path length quartz cuvette and referenced to the equivalent measurement with pure solvent. The molar extinction coefficient, ϵ , can then be calculated from the path length, l , concentration, c , and absorbance.

$$\epsilon = \frac{A}{cl} \quad (3.17)$$

Steady-state absorption spectra in the ultra-violet and visible range have been measured at room temperature using a Hewlett Packard 8453 UV-Vis spectrometer. Low temperature absorption measurements have been made using a Cary 6000i spectrometer with solid film and solution samples cooled to 80 K in an Oxford Instruments CF-V helium cryostat under high-vacuum (10^{-6} mbar).

3.5.2 Photothermal deflection spectroscopy

Photothermal deflection spectroscopy (PDS) provides a sensitive measure of the onset of absorption and can be used to quantify the level of electronic disorder in the absorption tail. The lowest energy absorptive transitions will be between tail states and the absorption onset is empirically found to vary exponentially with photon energy (E_γ)

$$\alpha = e^{(E_\gamma/E_u)}, \quad (3.18)$$

where E_u is called the Urbach energy and is used as a measure of electronic disorder.[75, 76] E_u can therefore be calculated by exponential fitting to the absorption tail. Organic semiconductors may typically display Urbach energy of approximately 50 meV in comparison

to approximately 10 meV for inorganic semiconductors such as gallium arsenide, cadmium telluride or crystalline silicon or approximately 15 meV for lead-based perovskites.[77]

In a PDS measurement the sample is immersed in FC-72 Fluorinert (3M Company). A monochromated light is then directed onto the sample. Absorption in the sample causes a heating effect and hence a temperature gradient in the surrounding medium. This causes a change in refractive index of the fluorinert which can be detected by the deflection of a continuous wave laser beam passing through it. PDS data shown in this thesis were measured by Mojtaba Abdi-Jalebi.

3.5.3 Transient absorption spectroscopy

Transient absorption (TA) spectroscopy is a method for determining the lifetimes and inter-related kinetics of excited states in materials by measuring the change in optical transmission at varying times following excitation. A monochrome laser at a high repetition rate is used to create excited states in the sample. The transmission of a broadband probe pulse is then measured as a function of wavelength and compared with the probe transmission in the absence of a pump beam. The delay between pump and probe is varied by physically changing the optical path length of the probe beam. The TA signal ($\frac{\Delta T}{T}$) is the ratio of the change in transmission (ΔT) between the pump-on and pump-off measurements and the transmission in the pump-off case (T) as shown in equation 3.19.

$$\frac{\Delta T}{T} = \frac{T_{Pump\ On} - T_{Pump\ Off}}{T_{Pump\ Off}} \quad (3.19)$$

A two-dimensional ($\frac{\Delta T}{T}$) map is produced with one axis being the probe wavelength and the second axis being the pump-probe delay time. The main features observed in TA spectra are a ground state bleach, stimulated emission and photoinduced absorption. Their spectral positions, shapes and lifetimes can all be assessed and used to determine properties and kinetics of excited states in the sample.

TA data in this thesis were measured by Alexander Gillett. The pump beam was supplied by a Yb³⁺ laser (PHAROS Light Conversion) operating at a 38 kHz repetition rate and approximately 250 fs pulse length at 1030 nm wavelength. Pump wavelength was selected by tuning a TOPAS optical parametric amplifier. The broadband probe pulse is generated in an yttrium aluminium garnet (YAG) crystal.

3.6 Photoluminescence

Photoluminescence is the emission of light by a material following initial excitation by a light source. As stated by Kasha's rule, the emitting level of a given multiplicity is usually the lowest excited level of that multiplicity.[1] Consequently the fluorescence spectrum of a material reveals the energy of the S_1 state in relation to the ground state, and similarly for the T_1 state in a phosphorescence spectrum. Another corollary to Kasha's rule is that the photoluminescence spectrum will not usually vary with excitation wavelength as long as the excitation energy remains larger than the HOMO-LUMO gap.

3.6.1 Steady-state photoluminescence

Steady-state photoluminescence has been measured using an Edinburgh Instruments FLS980 fluorometer. The excitation source is a xenon arc lamp with an in-built monochromator for excitation wavelength selection. The detector is a photomultiplier tube. A diffraction grating is used to scan through emission wavelengths for detection.

3.6.2 Transient photoluminescence

Time-resolved photoluminescence measurements were made using an Andor iStar DH740 intensified charge coupled device (iCCD) with an Andor Shamrock 303i spectrometer. An iCCD comprises a photomultiplier tube coupled to a CCD detector. Incident photons are first spectrally separated by a diffraction grating in the spectrometer before being incident on a photo-cathode. Electrons released from the photocathode are accelerated through an electric field and release secondary electrons from a microchannel plate and hence cause signal amplification. The secondary electrons are then incident on a phosphor which emits photons to be detected by the CCD. Time resolution is achieved through electrical gating of the potential in the photomultiplier tube.

Transient photoluminescence data in this thesis were measured by Emrys Evans and Saul Jones.

3.6.3 Photoluminescence quantum efficiency

Photoluminescence quantum efficiency (η_{plqe}) is the ratio of the number of photons emitted by a material under optical excitation to the number of photons absorbed by the material. η_{plqe} is dependent on the balance between the rate of radiative decay of excited states to the ground state and the rate of non-radiative decay. As such it is a limiting factor in the η_{eqe} of

OLEDs as shown by equation 2.20 and may indicate the presence or absence of damaging non-radiative decay pathways in OPV.

The measurement of η_{plqe} is made according to the method of de Mello et al. [78] Laser excitation is coupled into an integrating sphere through a small aperture. Scattered laser light and photoluminescence from a sample at the centre of the sphere are detected by an optical fibre-coupled Andor Shamrock spectrometer and Andor iDus CCD array. Three experimental measurements are made: (a) the laser excitation incident on an otherwise empty sphere, (b) the sample present but the laser excitation only directly incident on the wall of the integrating sphere, and (c) the laser excitation directly incident on the sample. This method allows the separation of effects from direct laser incidence and scattered light in the sphere. The η_{plqe} can then be calculated as

$$\eta_{plqe} = \frac{P_c - (1 - A)P_b}{L_a A}, \quad (3.20)$$

where P_c and P_b are the photoluminescence quanta measured in experiments (c) and (b) respectively, L_a is the laser quanta measured in experiment (a) and A is the fraction of directly incident laser light absorbed in experiment (c) and is in turn given by

$$A = 1 - \frac{L_c}{L_b}. \quad (3.21)$$

3.7 Ellipsometry

Ellipsometry is the measurement of the change in polarisation of incident elliptically polarised light on reflection at surfaces and interfaces in semiconductor materials and can be used to determine the thickness and optical constants of thin films. A Woollam M-2000 spectroscopic ellipsometer was used to calibrate the quartz crystal microbalance thickness sensors used in vacuum thermal evaporation fabrication of organic semiconductor films. The WVASE software package was used for data analysis and fitting. A Cauchy model was used to fit the ellipsometry data at wavelengths greater than the absorption onset, assuming isotropic films. It is worth noting that, having determined film thickness, modelling may be applied across all wavelengths to find the optical constants of organic semiconductors.[79]

3.8 Atomic force microscopy

Atomic force microscopy (AFM) is a technique to measure the topography of a surface with sub-nanometre resolution. A cantilever holding a sharp tip with radius of curvature less than

10 nm is made to oscillate at its resonance frequency. When the tip is brought close enough to the sample surface, van der Waals forces between the tip and the surface will damp the oscillation of the cantilever. In tapping mode AFM the tip is scanned across the sample surface in a raster pattern while a feedback mechanism keeps the amplitude of the cantilever oscillation constant by adjusting the cantilever height above the surface. In this way the surface topography can be mapped.

3.9 Grazing incidence wide angle X-ray scattering

X-ray scattering methods can be used to determine structural properties of a sample. The interference pattern produced by X-ray scattering from a material is determined by Bragg's law (equation 3.22) where d is the spacing of scattering objects, θ is the scattering angle, n is an integer and λ is photon wavelength. X-ray scattering can hence be used to determine the level of crystallinity in a sample at length scales similar to the incident photon wavelength.

$$2d \sin \theta = n\lambda. \quad (3.22)$$

In a grazing incidence wide angle X-ray scattering (GIWAXS) experiment a high-intensity X-ray beam is scattered from the surface of a solid film sample at a small angle of incidence. A large-area detector is held at a short beam length from the sample to detect scattered X-rays over a large angular distribution.

GIWAXS measurements were made using 10 keV X-rays at the Diamond Light Source, U.K, on the I07 beamline. A Pilatus 2M detector was used to measure the scattered X-ray intensity. The measured scattering angles were calibrated using silver behenate powder which displays clear diffraction features at known positions.

3.10 Electron spin resonance

As discussed in section 2.4.4, spin interactions, zero-field splitting and triplet formation mechanisms can be probed by electron spin resonance (ESR). ESR measurements presented in this thesis were made at the Centre for Advanced Electron Spin Resonance (CAESR) at the University of Oxford with the assistance of Dr. William Myers.

Measurements were made on a Bruker E680 spectrometer using an X-band microwave source at a fixed frequency of 9.5 GHz with a Bruker EN 4118X-MD4 resonator. The resonator was cooled to 80 K inside an Oxford Instruments nitrogen flow cryostat. At $B_0 = 0$ the resonator was tuned by manually adjusting an iris to ensure that the critical

coupling condition was achieved. When the resonator is critically coupled to the microwave source all the incident microwave power is dissipated in the cavity with no microwave power reflected back out of the cavity. Emission or absorption of microwaves by the sample at a resonant B_0 strength will change the coupling condition and therefore lead to the detection of microwaves from the cavity. Transient ESR (TrESR) measurements were made under continuous microwave irradiation. Laser photoexcitation was provided by an OpoTek Opolette 355 tunable optical parametric amplifier with an integrated Nd:YAG pump laser. Following each laser pulse, the ESR signal was recorded as a function of time at a fixed B_0 field. Measurements were made and summed over a number of laser pulses to improve the signal to noise ratio (SNR). B_0 was then stepped so that a two-dimensional TrESR dataset could be acquired with signal recorded as a function of both B_0 and time after the laser pulse.

Chapter 4

Carbene-metal-amides

4.1 Introduction

Carbene-metal-amides (CMAs) are a new class of emitter materials for OLEDs consisting of a cyclic (alkyl)(amino)carbene (CAAC) linked via a metal — typically copper(I), silver(I) or gold(I) — to a carbazolate or diphenylamide ligand.[80] Highly efficient solution-processed green CMA OLEDs have previously been demonstrated, with champion devices exhibiting $\eta_{eqe} = 27.5\%$. However, a large device-to-device variation was observed with the average peak η_{eqe} closer to 18%.[81] The use of coinage metal complexes as emitting materials in OLEDs could have large advantages over traditional phosphorescent materials based on iridium, such as greater material abundance and lower cost. Additionally, coinage metals have fully occupied outer d-orbitals so are not susceptible to the non-radiative loss channel through dd^* states which can limit the efficiencies of blue phosphorescent OLEDs. The carbene moiety forms strong chemical bonds with metals and hence CMAs may be more resistant to molecular fragmentation than established phosphorescent materials.[82, 83] CMAs therefore have great potential for use in high efficiency blue OLEDs. Indeed, copper-centred CMAs have been reported to show blue electroluminescence with peak $\eta_{eqe} = 9.0\%$, albeit at low brightness.[84]

As a note on nomenclature, there are large degrees of freedom in CMA molecular design and somewhat inconsistent naming conventions in the literature.[81, 84–87] The CMA materials investigated in this chapter share a common CAAC ligand but vary in their central metal and side group substitutions on a carbazole electron-donor moiety. For clarity and self-consistency, molecules will be named in the format metal-carbazole-side group substitution, as will be detailed in table 4.1.

Figure 4.1 shows the molecular structure of the archetypal gold-centred CMA molecule, Au-Cz. Also shown are density functional theory (DFT) calculations of the wavefunctions

of electrons in the LUMO and HOMO, as published by Di et al.[81] CMAs are donor-bridge-acceptor type molecules which — similarly to all-organic TADF molecules — show a separation between the HOMO, which is predominantly located on the amide donor subunit, and the LUMO, which is predominantly located on the carbene acceptor. The geometric separation of HOMO and LUMO reduces the exchange interaction between unpaired electrons in the intra-molecular CT excited state formed between the HOMO and LUMO. This results in a low ΔE_{ST} and hence the possibility of efficient reverse intersystem crossing and delayed fluorescence from the S_1 state. The electron density of the HOMO and LUMO do overlap across the metal bridge, which may also provide the opportunity for a substantial spin-orbit coupling interaction to mix the spin character of excited states and hence allow emission through a phosphorescence channel. The possible existence of two radiative decay channels for triplets may help reduce the excited state lifetime of CMAs in comparison to other phosphorescent or TADF emitter materials used in OLEDs. Short excited state lifetimes due to fast radiative decay would have consequent advantages for the efficiency of emission and device lifetime.

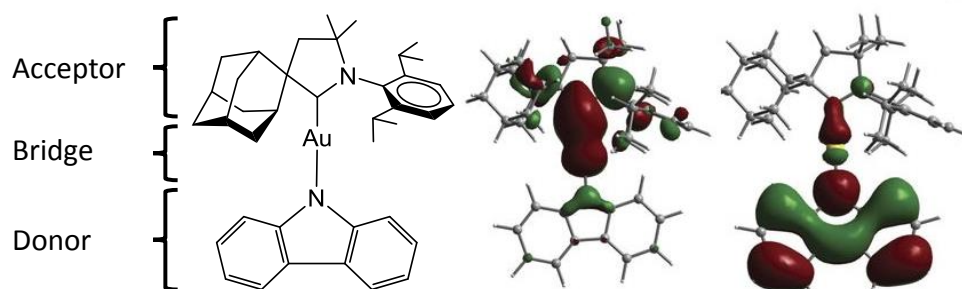


Fig. 4.1 The chemical structure of Au-Cz demonstrating the donor-bridge-acceptor structure typical of CMAs (left) and density functional theory calculations of LUMO (centre) and HOMO (right) wavefunctions as reported by Di et al.[81]

Both the oscillator strength and ΔE_{ST} in CMA compounds are calculated to depend on the dihedral angle between the carbene and amide ligands about the carbon-metal-nitrogen axis and on deformation of the carbon-metal-nitrogen bond, both of which have been shown to vary in the solid state with strong Raman modes evident at around 20 to 30 cm^{-1} (corresponding to ≈ 3 meV).[81, 88, 89] Due to their conflicting requirements on the overlap of HOMO and LUMO wavefunctions, it is typically assumed that a compromise must be made between a low ΔE_{ST} and a high oscillator strength to achieve efficient emission. The ability to control the distribution of rotational conformers, for example through alternative processing methods,

may result in emissive layers exhibiting different photophysical properties, which in turn will affect device performance.

CMAs are highly polar molecules; the ground state dipole moment of Au-Cz has been calculated to be 15 D directed along the C-Au-N axis from the carbene to the carbazole.[88] Upon excitation to form the intramolecular CT state an electron is moved from the carbazole to the carbene. This electron transfer causes a change in direction of the dipole moment, which in the excited state points from the carbazole to the carbene with a magnitude of 5 D.

In this chapter, the first demonstration of CMA OLEDs fabricated through vacuum thermal evaporation will be shown.[85] Au-Cz OLEDs with maximum $\eta_{eqe} = 26.9\%$ and improved reproducibility when compared to solution-processed variants have been achieved. Further, effective emission colour tuning is shown through control of the CMA molecular environment and specifically through the polarity of host materials. For example, using Au-Cz in varying host environments, electroluminescence could be shifted from CIE co-ordinates (0.24, 0.46) in the mid-green to (0.22, 0.35) in the sky-blue while maintaining high η_{eqe} . It has also been found that the emission colour can be tuned over a much wider range using molecular design. Using side group substitutions of varying electron-donating or electron-withdrawing character, electroluminescence can be shifted from yellow emission with CIE co-ordinates (0.38, 0.55), to deep blue (0.16, 0.05). Despite poor device performance in the deep-blue, high-efficiency blue-emitting OLEDs are demonstrated with maximum $\eta_{eqe} = 18.9$, peak wavelength 460 nm and CIE co-ordinates (0.17, 0.20). The energy of ligand-centred local excited states is found to be a limiting factor on emission colour and device efficiency. Further it has been discovered that CMA materials tend to be resistant to concentration-dependent luminescence quenching and this property has been used to successfully fabricate high efficiency host-free OLEDs. A maximum $\eta_{eqe} = 23.1\%$ is demonstrated for a host-free Au-Cz device, which could allow for a simplification of device architecture with consequent advantages for industrial manufacture. Additionally, the first demonstration of OLEDs incorporating mononuclear silver complexes as emitters is made, which opens the design space for new molecules.[86]

4.2 Collaborator contributions

CMA materials were synthesised by Dr Alexander Romanov, who also determined their HOMO and LUMO energies (E_{HOMO} and E_{LUMO}) by cyclic voltammetry and the 3LE and 1CT state energies ($E_{^3LE}$ and $E_{^1CT}$) by photoluminescence measurement in 2-methyltetrahydrofuran solution at room temperature and 77 K. Transient photoluminescence measurements were made by Saul Jones and Dr Emrys Evans. Campbell Matthews assisted with device fabri-

cation for Au-Cz-(CF₃)₂ and Au-Cz-(^tBu)(CF₃) emissive layers. GIWAXS measurements were performed by Dr Andrew Pearson. Molecular ground state dipole moments of host materials have been found through density functional theory calculations run by Dr Emrys Evans and Jiale Feng. Photothermal deflection spectroscopy measurements were made by Mojtaba Abdi-Jalebi. Photoluminescence quantum efficiency measurements were made by Dr Simon Dowland, Dr Alexander Romanov and myself.

4.3 Experimental methods

OLED devices were fabricated by high-vacuum (10^{-7} Torr) thermal evaporation on indium tin oxide (ITO)-coated glass substrates with sheet resistance of $15 \Omega \square^{-1}$. Prior to deposition, the substrates were sonicated sequentially in a non-ionic detergent, deionised water, acetone and propan-2-ol and subject to an oxygen plasma treatment for 10 minutes. Oxygen plasma treatment is known to increase the workfunction of the ITO and hence reduce injection barriers into the OLED.[90]

The OLED device architectures used are as shown in figure 4.2 and the associated material energy levels are shown in figure 4.3. The HOMO and LUMO energies of host, transport and blocking layers are taken from literature sources.[59, 91–96] Architecture 1 comprised a 40 nm thick layer of 1,1-bis[4-[N,N-di(4-tolyl)amino]phenyl]-cyclohexane (TAPC) used as both the EBL and HTL. The EML comprised a CMA material either in a host-free layer or dispersed in a host material at varying concentration between 5 wt.% and 50 wt.%. 1,3-bis(N-carbazolyl)benzene (mCP) and 1,3,5-tris(carbazol-9-yl)benzene (TCP) were used as host materials. A 10 nm hole-blocking layer of 1,4-bis(triphenylsilyl)benzene (UGH2) was lightly doped with 10 wt.% of 1,3,5-tris(2-N-phenylbenzimidazole-1-yl)benzene (TPBi) which was found to improve the yield of operational pixels. A 40 nm thick layer of TPBi was used as the ETL. The deposition rate for all organic layers was 0.2 nm s^{-1} . To incorporate more than four different organic materials into the device structure, it was necessary to break vacuum following deposition of a given layer, before re-evacuating and continuing. This was done either following the deposition of the HTL or EML. No variation in device performance was linked to the layer at which the vacuum was broken. Following the deposition of the ETL, the vacuum was broken for a second time to allow the insertion of a shadow mask through which the cathode was deposited. The cathode was formed of a 1 nm thick layer of lithium fluoride and a 100 nm thick layer of aluminium to form eight 4.5 mm^2 pixel areas on each substrate, as defined by the overlap area of the shadow mask and ITO stripe. A thin interlayer of lithium fluoride has previously been shown to reduce OLED turn-on voltages by reducing the injection barrier for electrons into organic semiconductor layers.[97, 98]

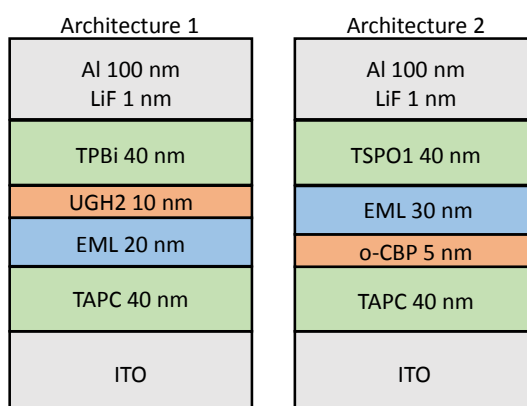
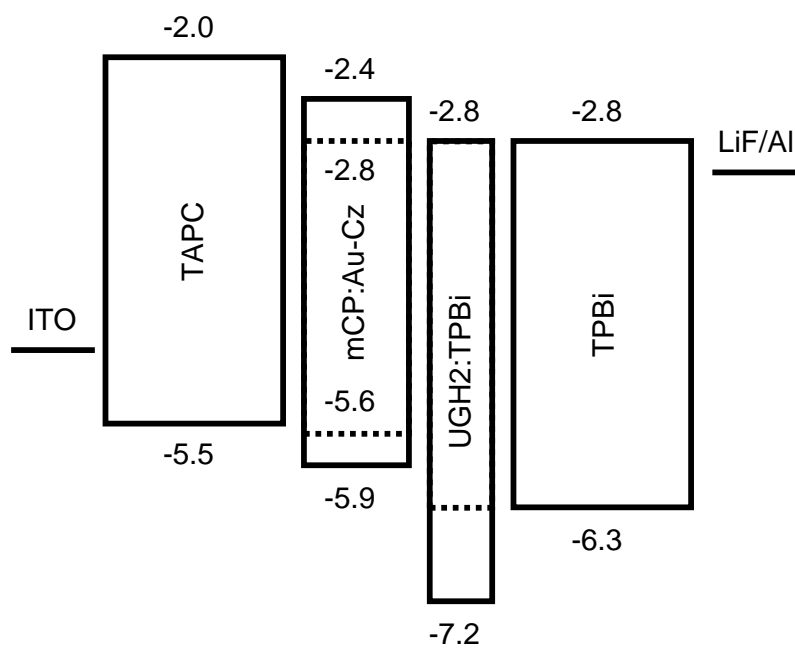
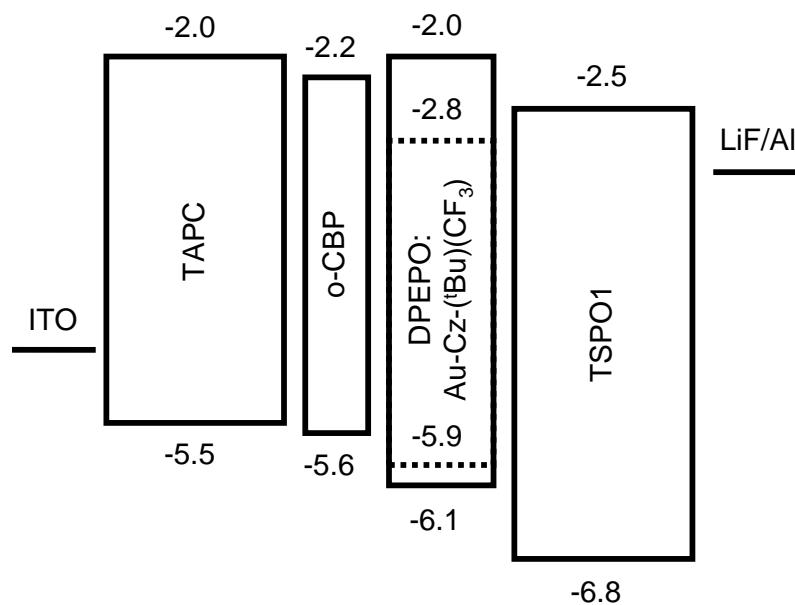


Fig. 4.2 Device architectures used in CMA OLEDs

Architecture 2 was used for blue-emitting CMA materials. In variation to architecture 1, a 40 nm layer of diphenyl-4-triphenylsilyl-phenylphosphine oxide (TSPO1) was used as electron-transport and hole-blocking layer. Due to the deep HOMO of TSPO1, at -6.8 eV, and T_1 energy of 3.4 eV, the additional HBL of UGH2 used in architecture 1 was not necessary.[96] A 5 nm layer of 9,9'-Biphenyl-2,2'-diylbis-9H-carbazole (o-CBP), with T_1 energy of 3.1 eV was used as a blocking layer to avoid triplet transfer to, or formation of interfacial states with the TAPC in the HTL.[94] Due to their high triplet energies, o-CBP and bis[2-diphenylphosphino)-phenyl]ether oxide (DPEPO) — which has a T_1 energy of 3.4 eV — were used as hosts for the blue-emitting CMAs.[95] The chemical structures of the materials used in this chapter are shown in figure 4.4, while table 4.1 details the variations in CMA molecular structure investigated. HOMO and LUMO energies were determined by cyclic voltammetry and the energies of ^1CT and ^3LE states were determined from photoluminescence measurements at room temperature and at 77 K in 2-methyltetrahydrofuran solution according to a literature method.[87]



(a) Architecture 1



(b) Architecture 2

Fig. 4.3 Proposed energy levels in OLED devices at open circuit a) architecture 1 and b) architecture 2

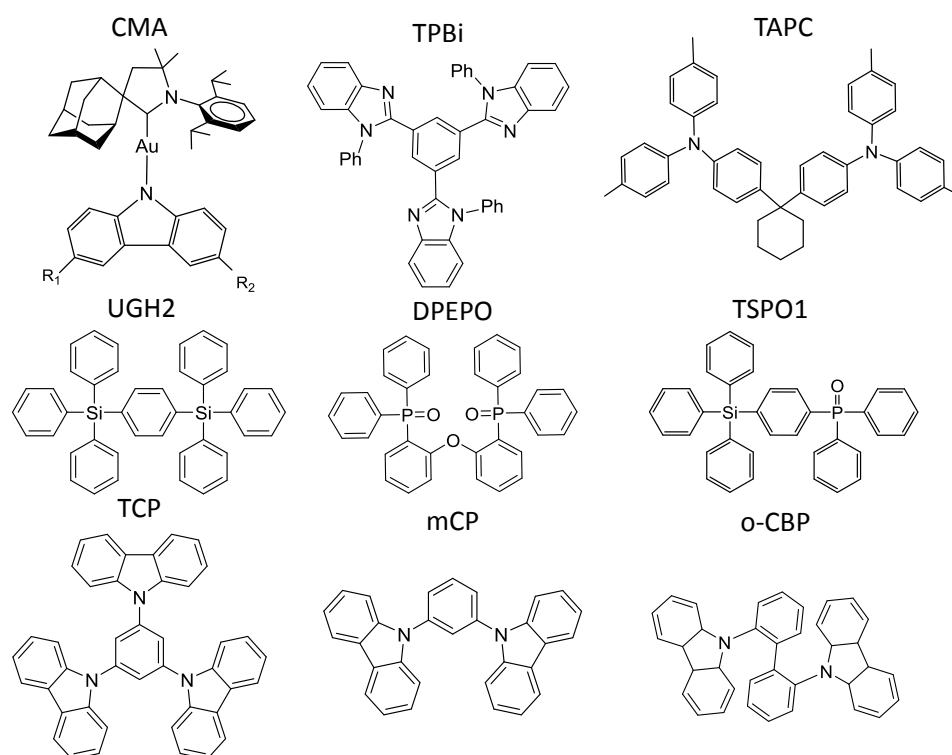


Fig. 4.4 Chemical structures of materials used in CMA OLEDs. The variations in R_1 , R_2 and central metal in CMA materials are outlined in table 4.1

Table 4.1 Molecular composition of CMA materials

CMA material	Central metal	R_1	R_2	E_{HOMO} (eV)	E_{LUMO} (eV)	$E_{1\text{CT}}$ (eV)	$E_{3\text{LE}}$ (eV)
Au-Cz	Au	H	H	-5.6	-2.8	2.76	2.96
Au-Cz-(^t Bu) ₂	Au	^t Bu	^t Bu	-5.5	-2.6	2.62	2.92
Au-Cz-(CF ₃) ₂	Au	CF ₃	CF ₃	-6.1	-2.9	3.09	3.04
Au-Cz-(^t Bu)(CF ₃)	Au	^t Bu	CF ₃	-5.9	-2.8	2.90	2.93
Ag-Cz	Ag	H	H	-5.5	-2.9		
Ag-Cz-(^t Bu) ₂	Ag	^t Bu	^t Bu	-5.3	-2.8		

4.4 Results

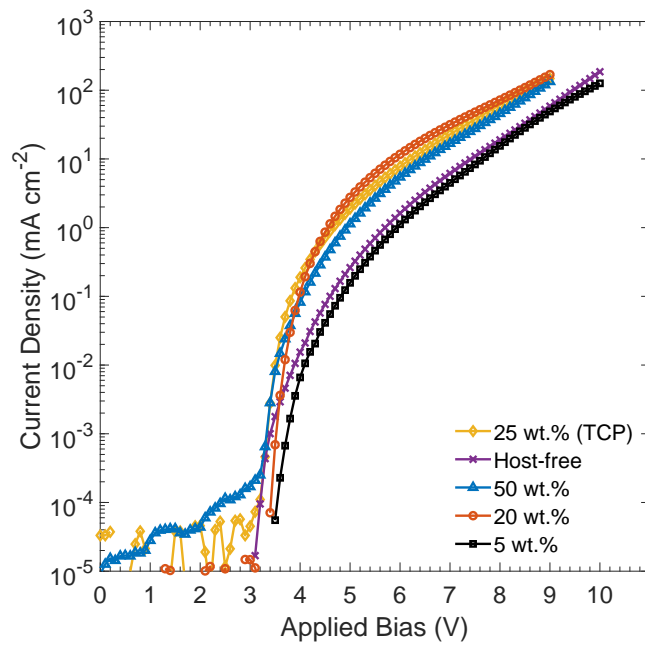
Figure 4.5 shows the current-density and luminance -voltage characteristics of champion Au-Cz evaporated devices with varying dopant concentrations in the emissive layer. Leakage currents at low applied bias are in the range of 10^{-5} mA cm⁻² for representative pixels. However $\approx 50\%$ of pixels displayed a large leakage current, on the order of 10^{-2} mA cm⁻² at forward biases below the electroluminescence turn-on. The bimodal variation in leakage current is thought to be due to inhomogeneity in the relatively rough UGH2 hole-blocking layer, which in some cases may allow a leakage current of holes through the device. The UGH2 layer was lightly doped with TPBi in an attempt to alleviate this problem. The AFM images in figure 4.6 show 10 nm thick UGH2 and UGH2:TPBi layers deposited on top of a layer of 20 wt.% mCP: Au-Cz. The root mean square roughness of the UGH2 and UGH2:TPBi films are similar at 7 nm and 8 nm, however the surface topography is substantially changed. The shallow LUMO of CMA1 limits the choice of available hole-blocking materials that could form a smoother layer while still allowing barrier-free electron transfer to the EML.

In this thesis, V_{on} is defined to be the applied forward bias at which luminescence exceeds 1 cd m⁻²; as shown in table 4.2, this is 4 V or lower for all emissive layer concentrations. This suggests an absence of large barriers to carrier injection, transport through the device, or transfer to the emitting CMA1 molecules.

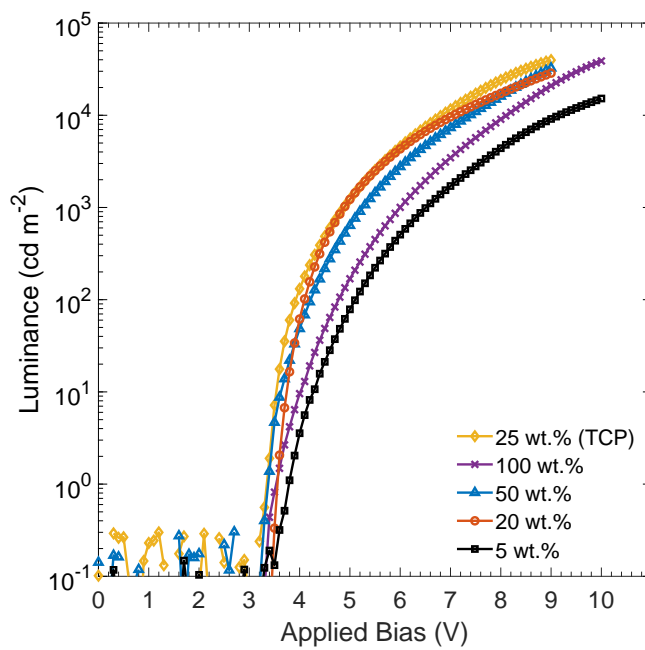
Table 4.2 Summary of champion (average \pm standard deviation) OLED V_{on} and η_{eqe} performance at varying EML doping concentration and brightness

Au-Cz concentration (wt.%)	V_{on} (V)	η_{eqe} (Max.) (%)	η_{eqe} (100 cd m ⁻²) (%)	η_{eqe} (1000 cd m ⁻²) (%)	CIE (x,y)
5	3.8 (4.0 \pm 0.1)	19.8 (17.8 \pm 1.6)	18.8 (15.8 \pm 1.0)	15.7 (12.6 \pm 1.1)	(0.22, 0.35)
20	3.5 (3.6 \pm 0.1)	24.3 (22.2 \pm 0.8)	22.5 (21.6 \pm 0.5)	19.4 (19.3 \pm 0.6)	(0.22, 0.36)
50	3.4 (3.4 \pm 0.1)	23.4 (22.0 \pm 0.9)	23.3 (21.9 \pm 0.9)	21.8 (20.7 \pm 0.7)	(0.23, 0.38)
100 (Host-free)	3.5 (3.4 \pm 0.1)	23.1 (18.5 \pm 2.6)	23.0 (18.4 \pm 2.7)	22.0 (17.7 \pm 2.5)	(0.24, 0.46)
25 (TCP host)	3.3 (3.4 \pm 0.1)	26.9 (26.0 \pm 0.6)	26.4 (25.6 \pm 0.8)	24.9 (24.4 \pm 0.6)	(0.24, 0.42)

Figure 4.7 shows η_{eqe} as a function of current density for champion evaporated Au-Cz OLEDs with varying emissive layer concentration in a host of mCP and at 25 wt.% in



(a) J-V characteristic



(b) L-V characteristic

Fig. 4.5 a) Current density-voltage and b) luminance-voltage characteristics for host-free CMA1 OLEDs, in a TCP host and varying concentration in an mCP host

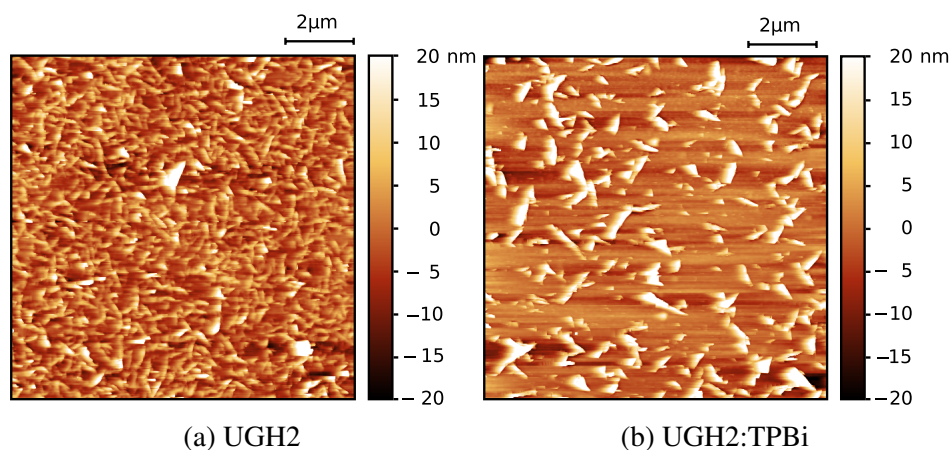


Fig. 4.6 Atomic force microscopy images of UGH2 hole-blocking layers a) with and b) without a 10 wt.% doping of TPBi

TCP. Performance data for champion devices are summarised in table 4.2 alongside average and standard deviation values. The highest recorded η_{eqe} was 26.9% for a TCP:CMA1 emissive layer with an average \pm standard deviation of $\eta_{eqe} = 26.0 \pm 0.6\%$. Using mCP as host peak $\eta_{eqe} = 22.2 \pm 0.8\%$ for the 20 wt.% emissive layer with $\eta_{eqe,max} = 24.3\%$ and $\eta_{eqe} = 22.0 \pm 0.9\%$ with $\eta_{eqe,max} = 23.4\%$ for the 50 wt.% emissive layer. These high η_{eqe} values imply very effective triplet harvesting in devices. High η_{eqe} was observed across a wide range of emissive layer concentrations, including a champion peak $\eta_{eqe} = 23.1\%$ for a host-free emissive layer. Efficient host-free OLEDs are a rarely reported result in the literature and this is believed to be a record performance for a host-free device with previously reported examples displaying $\eta_{eqe} < 20\%$.^[99]

Good roll-off characteristics are observed, especially for the 50 wt.% mCP: Au-Cz and host-free devices where the luminance at 90% of the peak η_{eqe} is 1500 and 2200 cd m^{-2} respectively, which is comparable to other well-performing OLEDs.^[68] The good roll-off performance means that high η_{eqe} values can be achieved at luminance levels relevant to either display or large-area lighting applications. This is further supported by the champion host-free devices η_{eqe} at 1000 cd m^{-2} of 22.0 % and 24.9% for TCP: Au-Cz. It is noted that although peak η_{eqe} reaches an optimum at 20 wt.% in an mCP host the η_{eqe} at 1000 cd m^{-2} continuously increases with CMA concentration. This apparently improved roll-off behaviour in higher CMA concentration devices could be due to reduction in the incidence of exciton-exciton annihilation events at high current density due to a lower excitation density per molecule.

Histograms of peak η_{eqe} as shown in figure 4.8 show a normal distribution of peak η_{eqe} for 20 wt.% mCP: Au-Cz devices but a multimodal distribution for host-free devices. This results

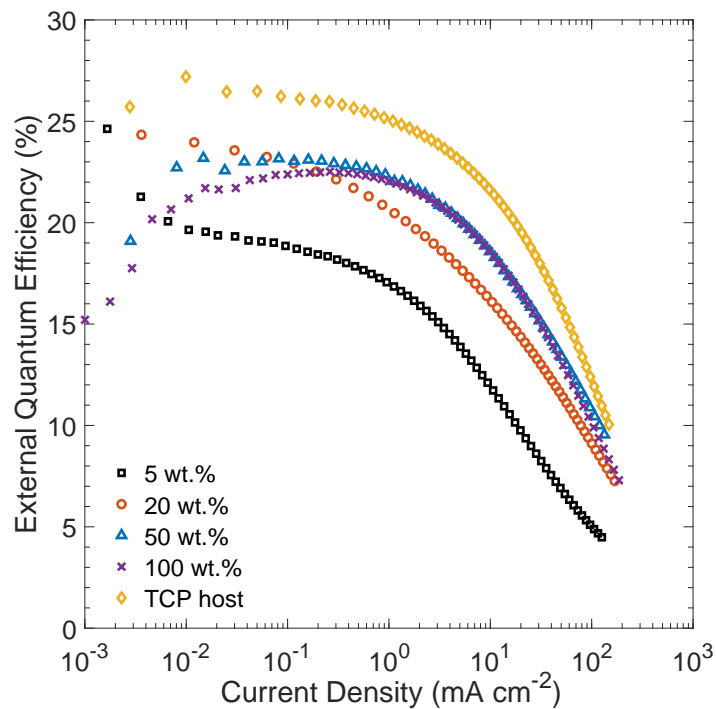


Fig. 4.7 η_{eqe} as a function of current density for Au-Cz OLEDs of varying dopant concentration in mCP, in a TCP host and in a host-free device

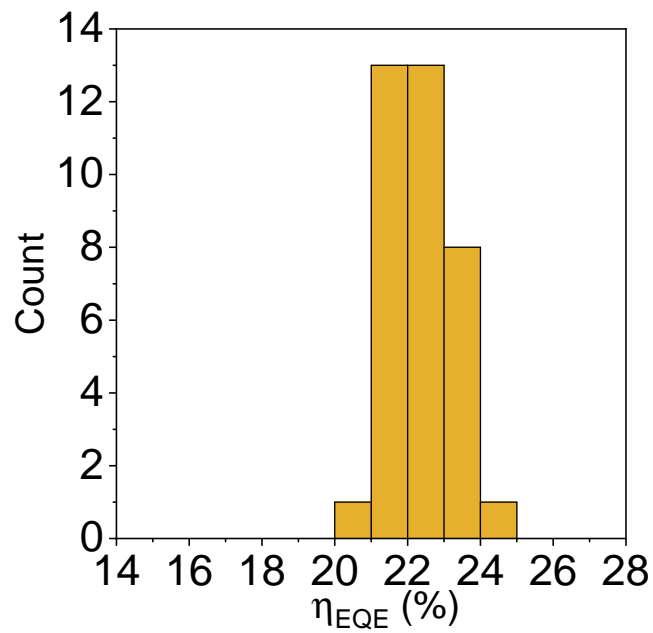
from good intrabatch reproducibility but increased variability between batches fabricated on different occasions. The effect is further illustrated in figure 4.9 which displays η_{eqe} as a function of current density for all working samples with 20 wt.% mCP: Au-Cz and host-free Au-Cz emissive layers. The three distinct populations of η_{eqe} curves in figure 4.9b represent three different fabrication dates. The decreased intrabatch reproducibility in host-free devices suggests a greater sensitivity to uncontrolled variations in processing conditions. The worst performing batch tends to show an increase in η_{eqe} with current density at low current, which is indicative of poor charge balance. It can also be seen in figure 4.10 that both the current and luminance are higher at a given applied bias in the lowest η_{eqe} batch. While this sharper turn on behaviour indicates a lower overall resistance in the device, it is apparent that the difference in current between batches is greater than the difference in luminance. It is therefore likely that there is a variation in leakage current between batches, possibly due to uncontrolled variation in thickness or morphology of the EML. The primary electronic role of the host is therefore likely to be to ensure good charge balance and consistent electronic properties of the EML, rather than dilution of guest molecules. The standard deviation of peak η_{eqe} between pixels is 2.6% for the host-free devices and less than or equal to 1.6% for all other emitting layer concentrations. This represents a much improved device-to-device

variation in comparison to the previously published solution-processed devices and hence represents a clear advantage to vacuum thermal evaporation as a fabrication technique for Au-Cz OLEDs.[81]

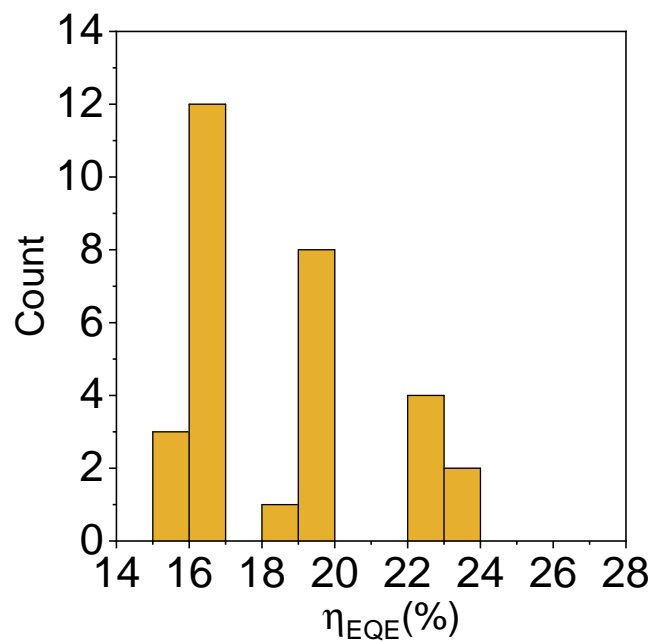
η_{eqe} was calculated as described in section 3.4 assuming Lambertian emission. To test the validity of this assumption, the angular distribution of emission was measured by mounting test devices onto a rotating sample holder. Manual adjustments were made to ensure that the selected pixel was aligned with the axis of rotation. The light intensity was measured using a 1 cm^2 photodiode at a distance of 30 cm. The device was rotated to vary the detection angle, θ , in 10° increments from $-90^\circ \leq \theta \leq 90^\circ$. To reduce any effect of device degradation the measurement was repeated by rotating in the opposite direction and an average was taken of the clockwise and anti-clockwise scans. As shown in figure 4.11 the resultant angular dependent emission intensity data was fitted with the function $\Phi = \cos^n(\theta + \beta)$. The parameter n determines the width of the distribution with $n = 1$ representing Lambertian emission, $n < 1$ representing relatively higher off-axis emission intensity and $n > 1$ representing relatively lower off-axis intensity. The parameter β accounts for a systematic offset in the emission angle originating from experimental uncertainty. As shown in figure 4.11, the n values fitted for 20 wt.% and 50 wt.% Au-Cz in mCP were 0.93 and 0.79 respectively and $n = 0.88$ for the host-free device. This represents super-Lambertian emission suggesting that the stated values of η_{eqe} may be underestimates, however no correction was made.

The measurement of η_{eqe} values greater than 20% suggests not only efficient triplet utilisation but also effective light outcoupling. Making the assumption that the charge carrier balance factor, γ , was equal to unity in champion devices and substituting η_{plqe} and maximum η_{eqe} into equation 2.20 suggests optical outcoupling efficiency of 28% for both the host-free and 20 wt.% mCP:CMA1 devices. Enhanced optical outcoupling can sometimes be attributed to favourable molecular dipole alignment.[100] However, in the case of increased dipole alignment parallel to the plane of the substrate, it would be expected to observe an increase in emission intensity along the direction normal to the substrate. As has been seen in angular dependence of emission measurements in figure 4.11, this is not the case.

GIWAXS measurements were made to investigate the molecular packing within solid films of Au-Cz. As shown in figure 4.12 a comparison was made between vacuum-deposited films of host-free Au-Cz, mCP: Au-Cz (20 wt.%) and a drop-cast film of Au-Cz. The diffraction pattern observed from the drop-cast film in figure 4.12a shows multiple sharp scattering features indicating a polycrystalline morphology. In contrast when Au-Cz films are processed by vacuum thermal evaporation, either as host-free films (figure 4.12b) or in an mCP host (figure 4.12c) the morphology appears to comprise nanoscale aggregations

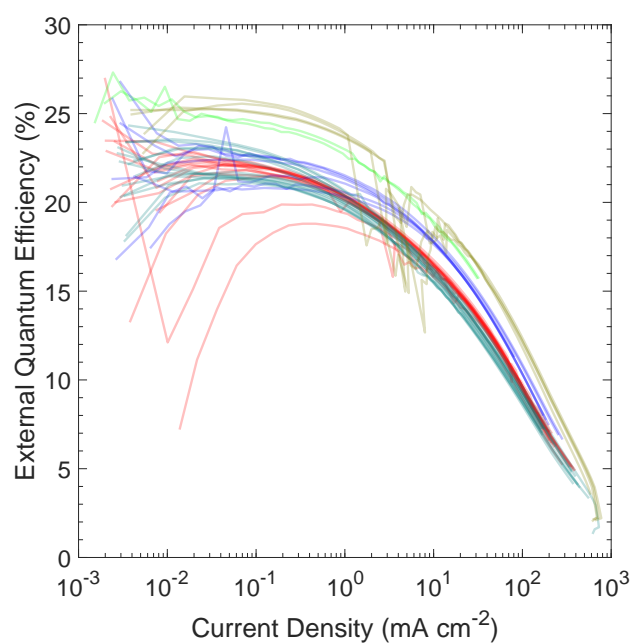


(a) mCP: Au-Cz 20 wt. %

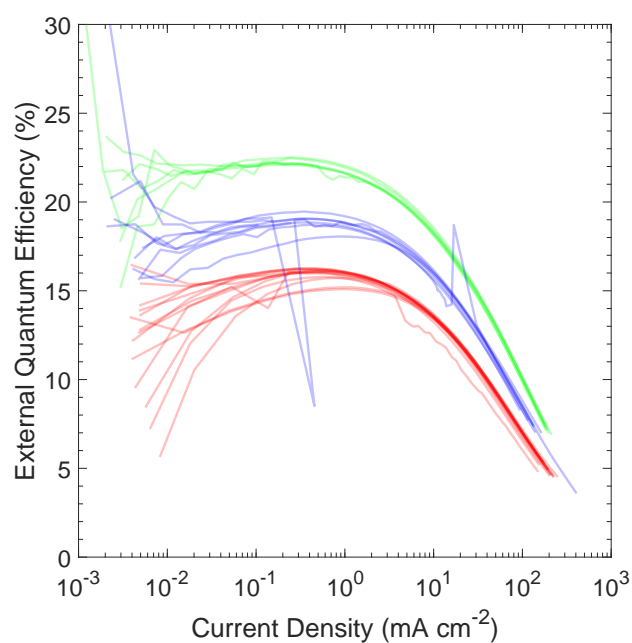


(b) Host-free Au-Cz

Fig. 4.8 Histograms of peak η_{eqe} for Au-Cz OLEDs in a) an mCP host and b) host-free devices. c) and d) η_{eqe} as a function of current density for all samples included in the histograms

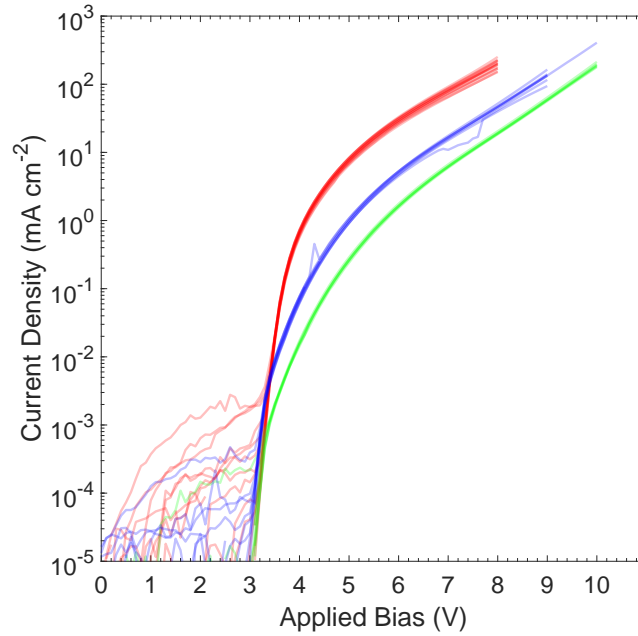


(a) mCP:Au-Cz 20 wt. %

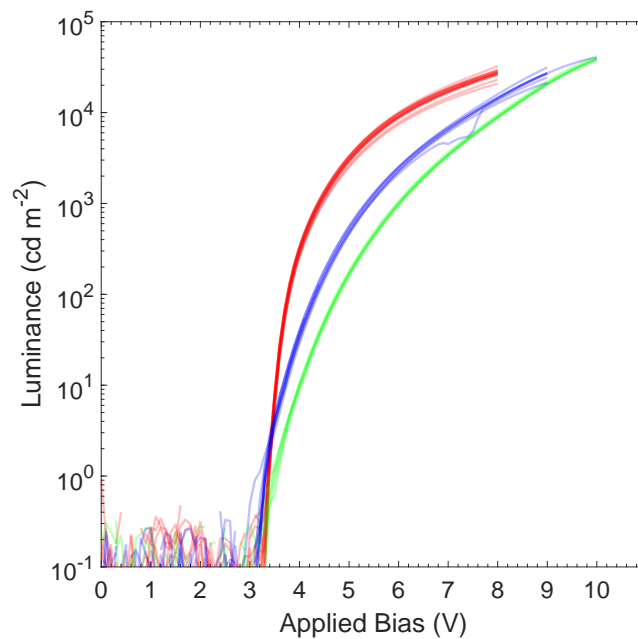


(b) Host-free Au-Cz

Fig. 4.9 η_{eqe} as a function of current density for all tested devices with a) mCP:Au-Cz and b) host-free Au-Cz emissive layers. The line colours represent different device fabrication batches

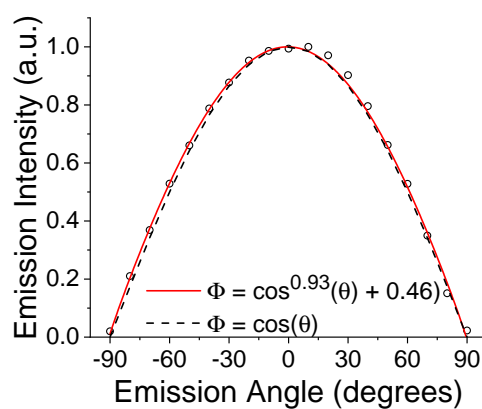


(a) J-V characteristic

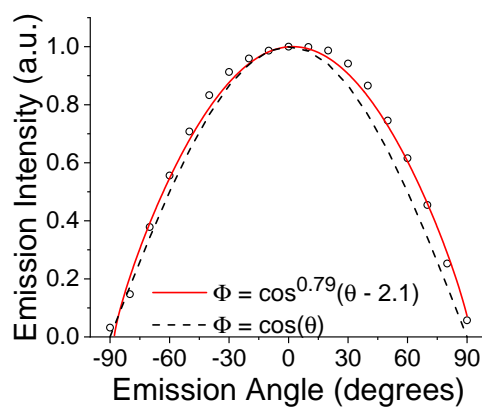


(b) L-V characteristic

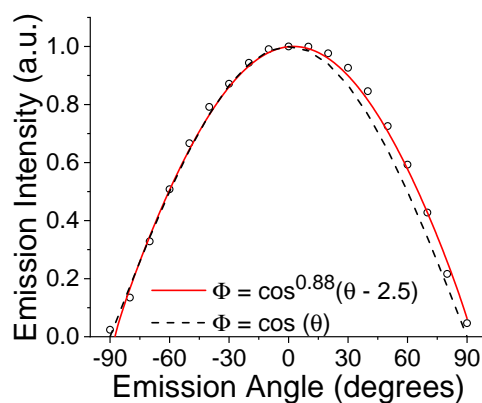
Fig. 4.10 Reproducibility of a) J-V and b) L-V characteristics for host-free Au-Cz OLED devices. The line colours represent different device fabrication batches



(a) mCP:Au-Cz 20 wt. %



(b) mCP:Au-Cz 50 wt. %



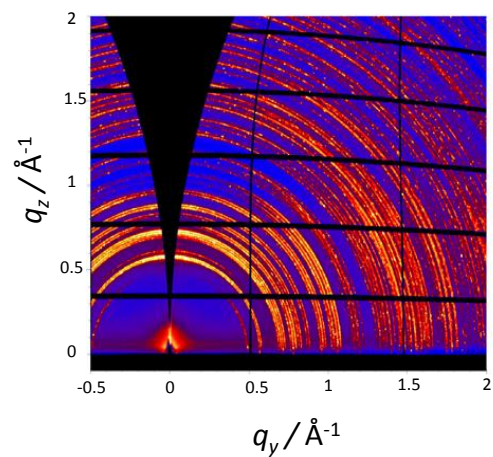
(c) Host-free Au-Cz

Fig. 4.11 The angular intensity dependence of Au-Cz OLEDs at varying concentration in mCP. The red line shows the fitted angular dependence function while the black dashed line shows $y = \cos(x)$ for indication

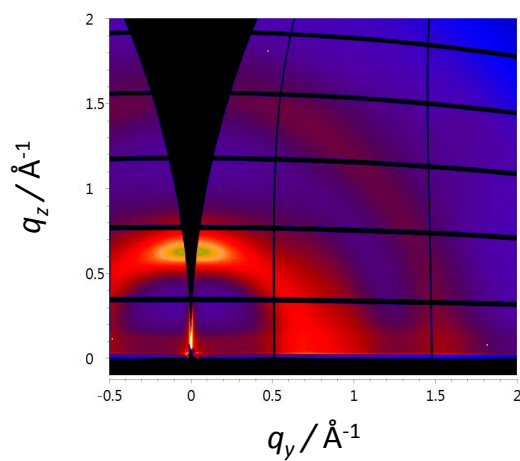
with limited internal order. The scattering ring present at $q \approx 0.63 \text{ \AA}^{-1}$ is broad and has no associated higher order reflections. Given the mostly amorphous nature of the Au-Cz films and only weak preference for packing out of plane, as inferred from the higher intensity of X-ray scatter along this direction, evidence has not been found for any preferential molecular alignment which would cause a significant enhanced optical outcoupling effect in OLED devices.

The weak relationship between Au-Cz concentration in mCP and device performance, and the impressive performance of host-free devices implies that the concentration-dependent luminescence quenching observed for most OLED emitters is largely absent in Au-Cz. To investigate this, η_{plqe} was measured under a flow of nitrogen with continuous wave laser excitation at $\lambda_{Ex} = 405 \text{ nm}$ for 20 wt.% and host-free films. The 20 wt.% film exhibited a η_{plqe} of 86% while the host-free film exhibited a very similar η_{plqe} of 83%. By contrast the η_{plqe} of the green phosphorescent emitting material Ir(ppy)₃ decreases from 97 % at low concentration in the common host CBP to 3 % in a host-free film.[101] The observation of high η_{plqe} in both host:guest and host-free films suggests that intermolecular interactions between Au-Cz molecules are relatively weak such that aggregation does not contribute to luminescence quenching.

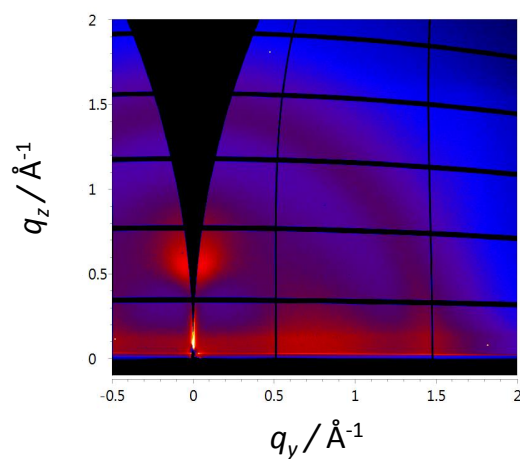
Electroluminescence and photoluminescence spectra are shown in figure 4.13. Photoluminescence was measured through photoexcitation of Au-Cz at 390 nm in a complete device. Electroluminescence was measured at a current density of 0.2 mA cm^{-2} , equivalent to a luminance of approximately 100 cd m^{-2} . It has been verified that the electroluminescence spectrum does not vary with current density for these devices. For the emitter concentrations between 5 and 50 wt.% in mCP, the electroluminescence peak is at $\lambda = 475 \text{ nm}$. At higher concentrations the emission broadens with an increasing contribution from a shoulder at $\lambda = 540 \text{ nm}$. The spectral positions of the peaks at $\lambda = 475 \text{ nm}$ and $\lambda = 540 \text{ nm}$ do not shift appreciably, nor does the emission onset, but a relative change in peak intensity is observed. The host-free device shows unstructured electroluminescence at $\lambda = 500 \text{ nm}$. This is coincident with the electroluminescence peak from the TCP-host devices but corresponds to a 100 meV change in the peak emission energy between a 20 wt.% mCP-host and host-free devices. A shift of 80 meV is observed in the high energy onset of the emission when moving from mCP: Au-Cz host-guest to host-free devices. The consequent evolution in CIE colour co-ordinates is shown in figure 4.14, which also shows that the electroluminescence spectrum of vacuum-processed devices is blueshifted in comparison to the previously reported solution-processed OLEDs. The associated steady-state photoluminescence spectra are also shown in figure 4.13 exhibiting unstructured emission centred at $\lambda = 472 \text{ nm}$ in the 5 wt.% layer and 480 nm in the host-free and TCP: Au-Cz layers. For mCP: Au-Cz films the photolu-



(a) Drop cast Au-Cz



(b) Evaporated host-free Au-Cz



(c) Evaporated mCP: Au-Cz 20 wt. %

Fig. 4.12 2D GIWAXS patterns of drop-cast Au-Cz and thermally evaporated Au-Cz host-free and mCP: Au-Cz films. The intensity of X-ray scatter is presented on a common colour scale

minescence and electroluminescence peaks are coincident although the photoluminescence displays a lower intensity low-energy tail. In host-free Au-Cz or TCP: Au-Cz layers the photoluminescence is blue-shifted in comparison to the electroluminescence.

There are a number of differences in the origins of photoluminescence and electroluminescence which may explain the observed spectral variation. Firstly, on photoexcitation the depth-distribution of excited states follows an exponential decay according to the Lambert-Beer law. As found from UV-Vis absorption spectroscopy and thickness determination from ellipsometry, the absorption coefficient of a host-free Au-Cz film at 390 nm is $4.4 \times 10^4 \text{ cm}^{-1}$ and $0.9 \times 10^4 \text{ cm}^{-1}$ for 20 wt.% films in either mCP or TCP hosts. Therefore photoexcitation at $\lambda_{Ex} = 390 \text{ nm}$ would lead to relatively uniform excitation. The variation in excitation density with depth is only $\approx 2\%$ in the case of a 20 nm Au-Cz layer at 20 wt.% in an mCP or TCP host and $\approx 8\%$ in the case of a 20 nm host-free Au-Cz layer. In contrast the position and distribution of the recombination zone in an OLED under electrical excitation is dependent upon the charge balance in the emissive layer and can be pinned to the interface between the EML and HTL or ETL.[69, 102] In this case the electroluminescence may be affected by interface effects to a greater extent than photoluminescence. It is speculated that interface effects may be more prominent in mCP: Au-Cz devices than in TCP: Au-Cz or host-free Au-Cz devices and that this could be the source of the shoulder peak at $\lambda = 540 \text{ nm}$ that is evident only in the electroluminescence of mCP: Au-Cz devices. This could possibly be investigated by a strip-doping method where a thin layer of the EML is doped with an exciton quenching material, which may be poorly emissive or have spectrally distinct emission from Au-Cz.[102] The subsequent reduction in Au-Cz electroluminescence intensity and/or increase in dopant emission as a function of position of the dopant in the EML can give information about the position, extent and distribution of the recombination zone. Electroluminescence relies on the transport of charges prior to recombination. Given that charge transport is most favoured when moving from a higher energy site to a lower energy site it is therefore more likely for electroluminescence to originate from lower energy sites and hence to observe a red-shift in comparison to photoluminescence. This could explain the shift seen in host-free and TCP hosted devices.

It has been proposed that reorganisation of molecular dipoles plays an important role in the emission of Au-Cz in solid host-guest films, since CMA molecules exhibit a large static dipole moment in their ground state which changes sign upon excitation.[88] Using photothermal deflection spectroscopy a blue-shift of the Au-Cz absorption edge of approximately 30 meV is observed when Au-Cz is dispersed in an mCP host (figure 4.15). mCP has a static dipole moment of 1.4 D as found through density functional theory (DFT) calculation. However the concomitant blueshift in electroluminescence indicates that any reorganisation of the

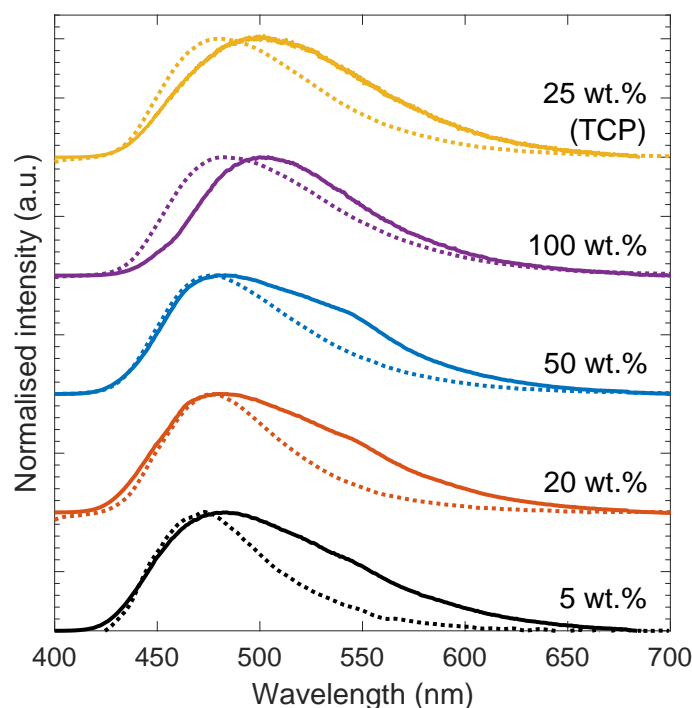


Fig. 4.13 Electroluminescence (solid lines) and photoluminescence (dashed lines) at excitation wavelength $\lambda_{Ex} = 390$ nm for host-free Au-Cz, in a TCP host and at varying concentrations in an mCP host

host-guest composite to accommodate the excited state dipole occurs on longer timescales than that of luminescence. The electroluminescence peak and absorption onset of TCP: Au-Cz films are coincident with those of host-free Au-Cz films. Due to its symmetrical structure, TCP is largely non-polar with only a small static dipole moment calculated to be 0.3 D. This suggests that Au-Cz behaves as a relatively non-polar environment, which may be consistent with the amorphous nature of host-free Au-Cz films observed through GIWAXS measurements.

Time resolved photoluminescence measurements were made using $\lambda_{Ex} = 400$ nm under high-vacuum (10^{-5} mbar) to determine the impact of the evaporated host-guest morphology on emission kinetics and to clarify the role of triplets. Figure 4.16 shows room temperature (≈ 295 K) photoluminescence kinetics integrated over all wavelengths for evaporated films of host-free Au-Cz and 20 wt.% Au-Cz in mCP and TCP hosts. Less than 1% of the total emission occurs in the first 5 ns after excitation, which indicates that prompt singlet emission is quenched. Since the high neat-film η_{plqe} value shows that the nonradiative decay rate must be slow, we assign this quenching to rapid intersystem crossing to the triplet state. The subsequent emission pathway must therefore come from the triplet state such

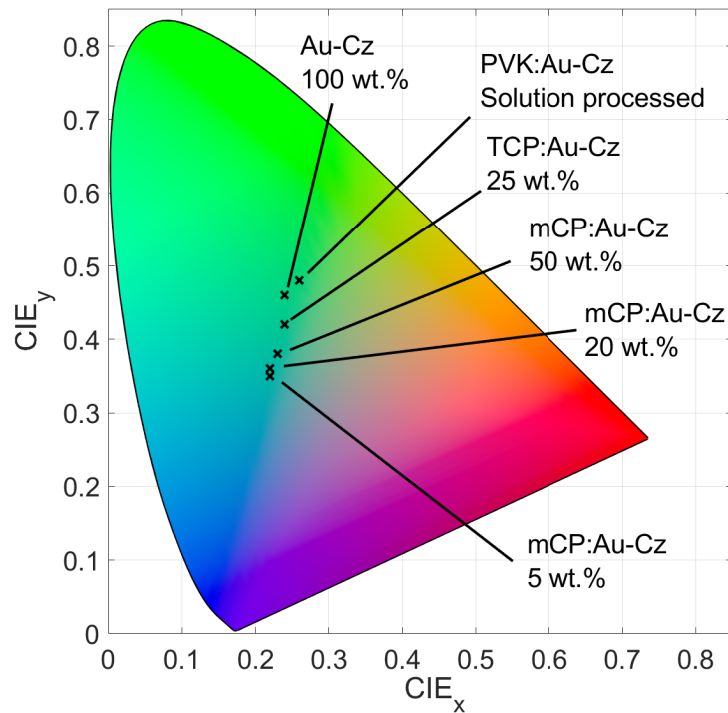


Fig. 4.14 CIE Colour space diagram for Au-Cz OLEDs. The datum for PVK: Au-Cz solution-processed device is taken from [81]

that photoluminescence and electroluminescence follow similar pathways despite having different initial population ratios of singlets and triplets. The decay kinetics for host-free Au-Cz, mCP: Au-Cz and TCP: Au-Cz at room temperature are non-exponential and the emission spectra in figure 4.16b redshift over time, consistent with an ensemble of molecular configurations with different intrinsic lifetimes. A characteristic photoluminescence decay time was found for each sample, being the time taken for the integrated emission to reach a fraction $(1 - \frac{1}{e})$ of the total. This allows easy comparisons to be made with lifetimes of other emitters extracted from monoexponential decays. The characteristic decay times were found to be 755 ns for the host-free film, 881 ns for the mCP host film and 972 ns for the TCP host film. At room temperature, the photoluminescence of the mCP: Au-Cz and host-free Au-Cz films redshifts by 135 ± 10 meV between 20 ns and 5 μ s following excitation. The TCP: Au-Cz films shows a redshift of 84 meV over the same timescale. At early times (0-100 ns), the mCP: Au-Cz photoluminescence spectrum is blueshifted compared to the host-free and TCP: Au-Cz spectra, which is consistent with measurements of electroluminescence and absorption onset. However, at later times (500-5000 ns) the photoluminescence of mCP: Au-Cz and TCP: Au-Cz films both peak at 510 nm (compared to 530 nm for host-free

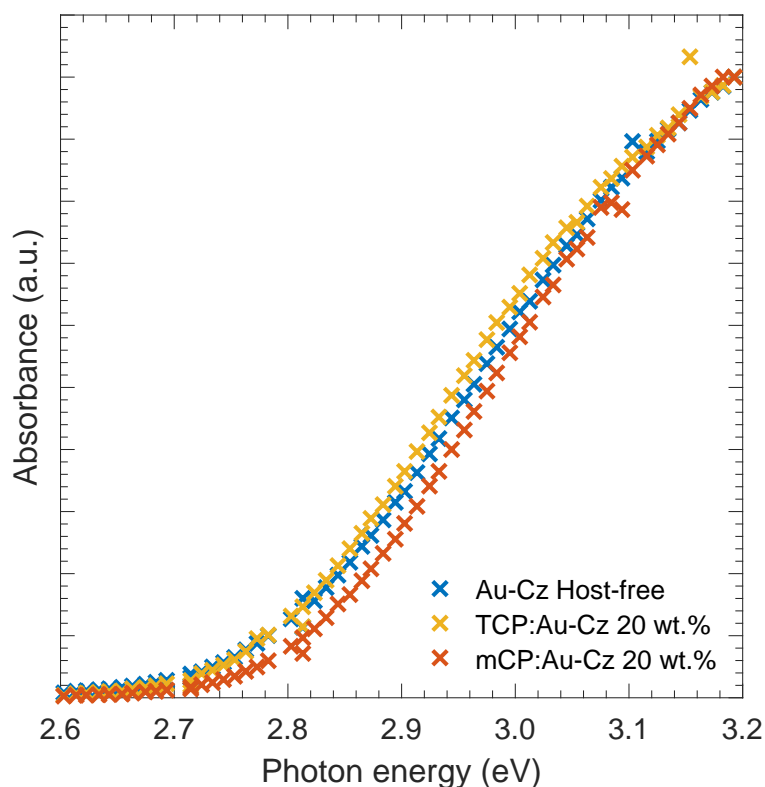


Fig. 4.15 The absorption onset of a host-free Au-Cz film and in a TCP and mCP host as measured by photothermal deflection spectroscopy

Au-Cz). This spectral diffusion suggests migration of excitons occurs on similar timescales to emission and implies a relatively high energetic disorder is present in the chromophore population. The level of energetic disorder can be evaluated by Urbach energy, which has been calculated from PDS data in the 68 ± 7 meV range for all films. This disorder may represent static configurational variation or the ability of individual chromophores to access a range of geometric configurations over time.

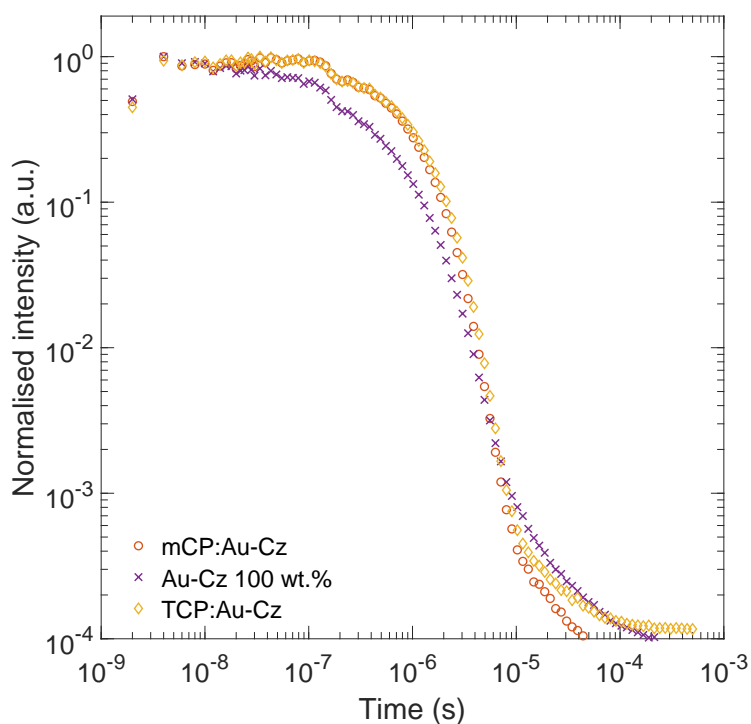
Photoluminescence decay kinetics at varying temperature between 50 K and 295 K are shown in figure 4.17a. The associated characteristic decay times are shown in the Arrhenius plot in figure 4.17b. Emission is found to be thermally activated with a temperature-independent emission regime revealed below 100 K. By fitting the data above 100 K to an Arrhenius equation an activation energy of 73 meV is found. However, fitting to all the data and including a temperature-independent offset gives a slightly higher activation energy of 79 meV. This is consistent with a TADF-type emission process where T_1 is weakly

coupled to S_0 but thermal excitation allows access to intermediate states offering stronger coupling to S_0 . The temperature-independent component could be due to phosphorescent emission. It is noted that room temperature emission is dominated by the thermally activated component. Figure 4.16b shows the room-temperature emission spectra to be broad and unstructured, consistent with the emissive state having CT character. Figure 4.18a shows that photoluminescence spectra remain unstructured at all temperatures i.e. the emissive state retains CT character even in the absence of thermal energy, and no ligand-centred local triplet with lower energy is revealed. This is in agreement with previously reported quantum chemical calculations and state energies found in 4.1. [81, 88, 89]. The emission energy blueshifts at low temperature, which is interpreted to mean that relaxation modes for the CT excitons are progressively frozen out. Given the sub-microsecond emission lifetimes at room temperature and the presence of a heavy element, it is inferred that spin-orbit coupling is the most likely mediating interaction between the triplet and singlet states.

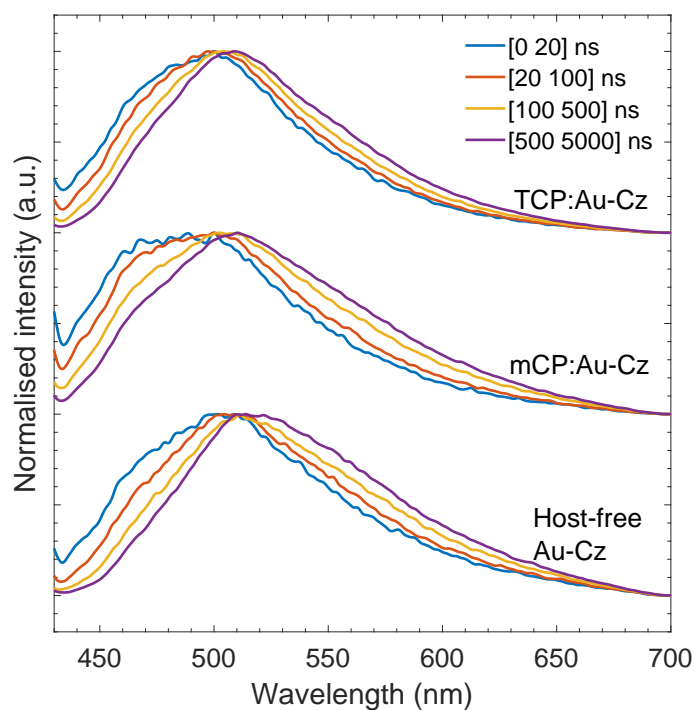
4.4.1 Colour tuning through molecular design

The addition of molecular side groups of varying electronegativity to the donor moiety can be used to perturb the HOMO and hence alter the intra-molecular CT state energy and ultimately the emission colour. As seen in the work of Di et al., the addition of electron-donating tertiary-butyl side groups in Au-Cz-(^tBu)₂ produced similar η_{eqe} performance to Au-Cz in solution-processed devices but with red-shifted emission. This is likely to be due to the increased electron-donating strength of the tertiary-butyl substituted carbazole causing a decreased CT state energy.

To further investigate the effect of side group electronegativity a series of materials was composed as detailed in table 4.1. The Au-Cz molecular motif was modified by the addition of electron-withdrawing and electron-donating side groups on the carbazole donor moiety in the R₁ and R₂ positions indicated in figure 4.4. As previously observed, the use of electron-donating side groups such as tertiary-butyl in Au-Cz-(^tBu)₂ has the effect of reducing the intra-molecular CT state energy and would be expected to red-shift the emission. Conversely, the addition of electron-withdrawing groups such as CF₃ in Au-Cz-(CF₃)₂ increases the CT state energy and would be expected to blue-shift emission. The use of mixed tertiary-butyl and CF₃ groups was also found to raise the CT state energy but by a more moderate amount than in the case of double-CF₃ substitution. In all cases it is found that the CT state energy is modified by a greater magnitude than the lowest energy ligand-centred triplet exciton state (³LE). As such it is possible to modulate the energy gap between CT and ³LE states by varying side group substitutions. Investigating the device properties of OLEDs incorporating these materials can reveal whether excited state dynamics

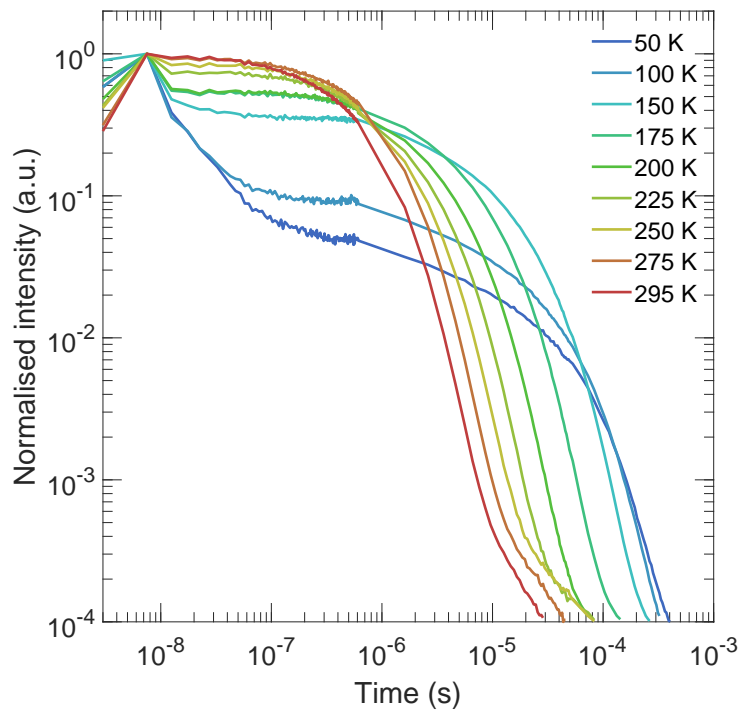


(a) Transient photoluminescence kinetics

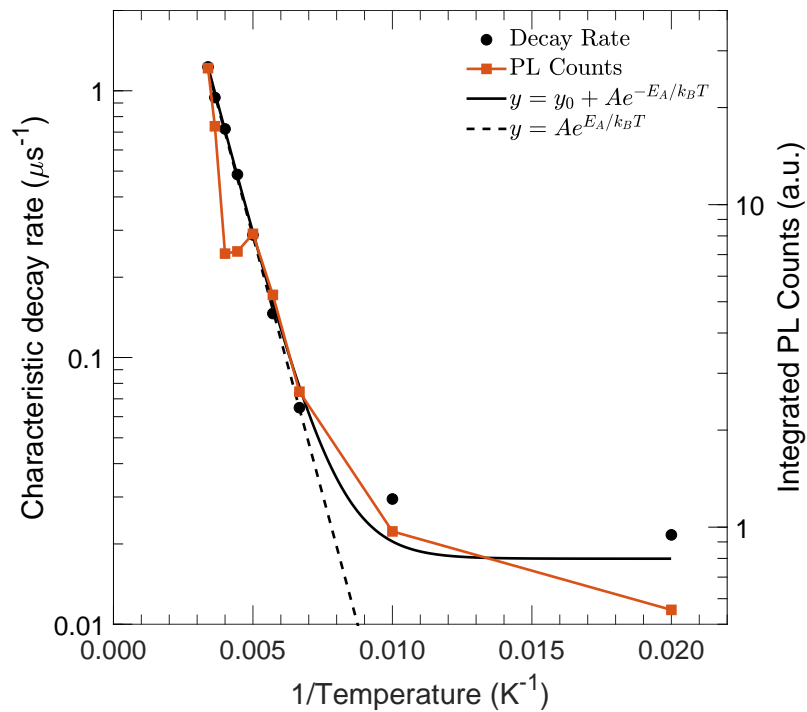


(b) transient photoluminescence spectral evolution

Fig. 4.16 Transient photoluminescence a) kinetic and b) spectral evolution for a host-free Au-Cz film and at 20 wt.% in mCP and TCP hosts. $\lambda_{Ex} = 400$ nm

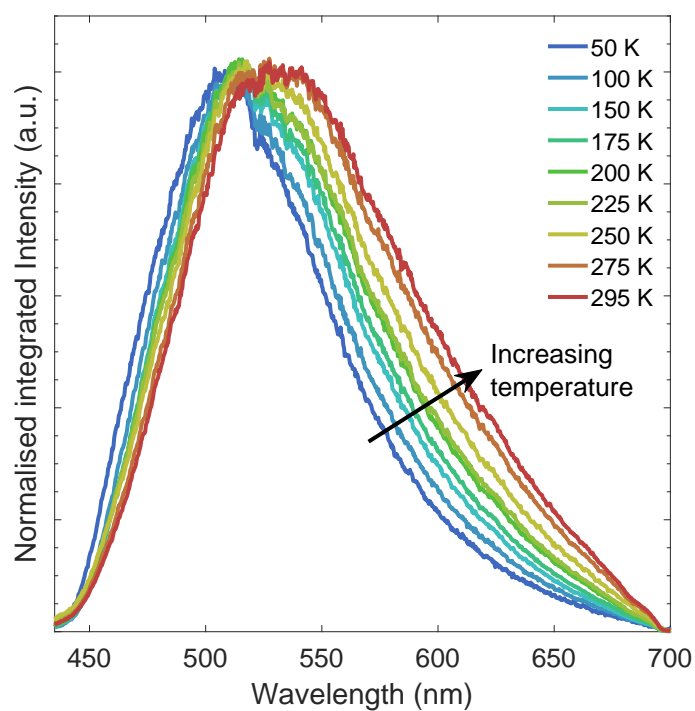


(a) Transient photoluminescence kinetics

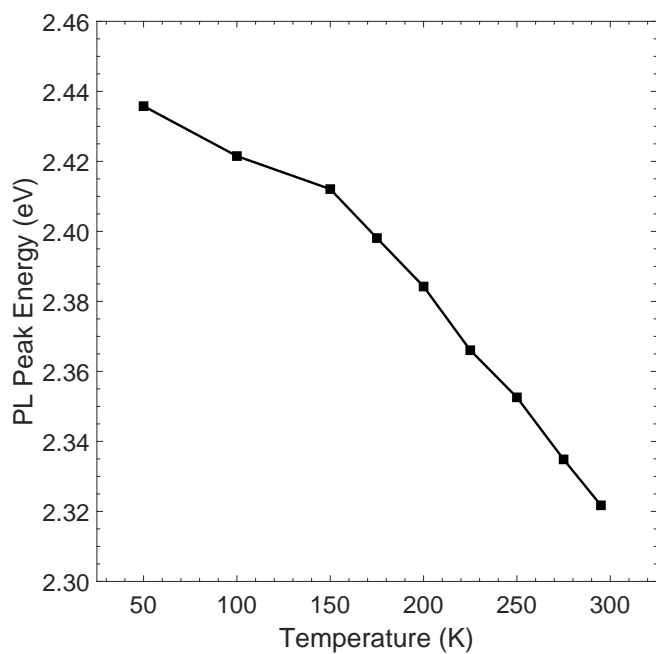


(b) Arrhenius-type plot

Fig. 4.17 a) Transient photoluminescence decay kinetics of a host-free Au-Cz film at varying temperature with $\lambda_{Ex} = 400$ nm b) Arrhenius plot with associated curve fitting. The solid line shows the fitting of $y = y_0 + Ae^{-E_A/k_B T}$ to all temperature points. The dashed line shows the fitting of $y = y_0 + Ae^{-E_A/k_B T}$ excluding the 50 K and 100 K data points



(a) Temperature dependent photoluminescence spectra



(b) Temperature dependent photoluminescence peak energy

Fig. 4.18 a) Temperature dependent photoluminescence spectra and b) peak energy shift for an Au-Cz solid film. $\lambda_{Ex} = 400$ nm

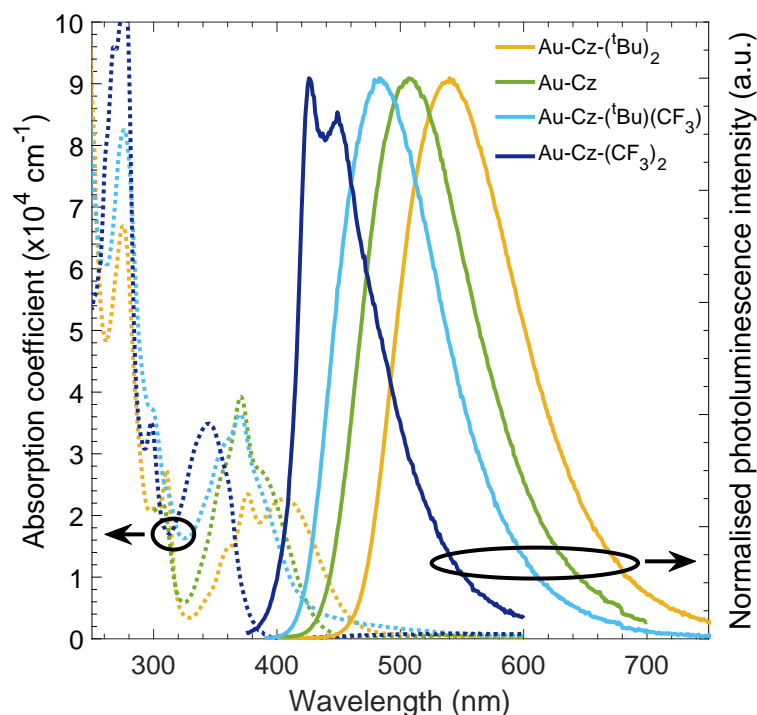


Fig. 4.19 Absorption coefficient (dotted line, left-hand axis) and photoluminescence (dotted line, right-hand axis) of gold-centred CMA materials with varying side group substitutions. The excitation wavelength for photoluminescence measurements was 375 nm

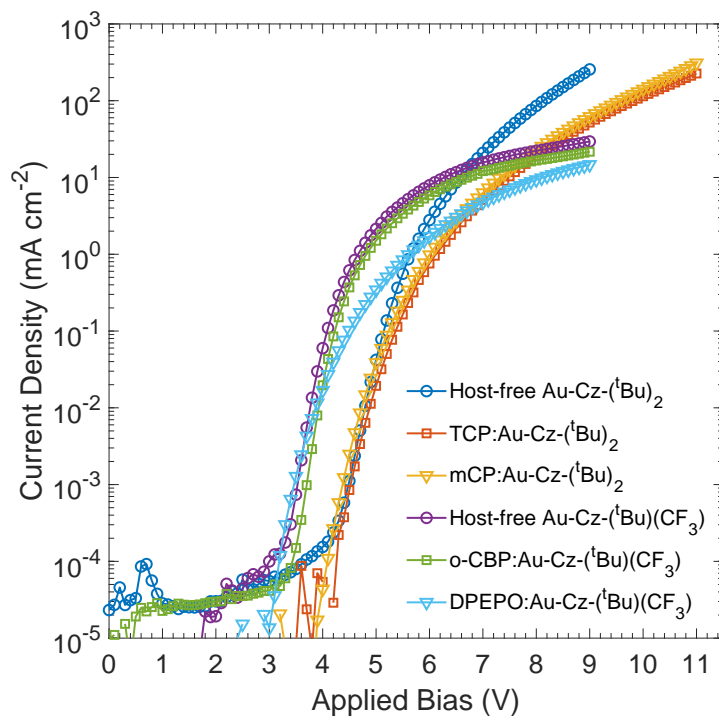
between the CT and ^3LE states affect the radiative pathway as has been claimed in the case of all-organic TADF materials.[14] The photoluminescence and absorption spectra of pure films of Au-Cz-(^tBu)₂, Au-Cz, P74 and Au-Cz-(CF₃)₂ are shown in figure 4.19. Clear spectral separation is observed with peak wavelengths at 540, 507, 483 and 426 nm for Au-Cz-(^tBu)₂, Au-Cz, Au-Cz-(^tBu)(CF₃) and Au-Cz-(CF₃)₂ respectively. In the case of Au-Cz-(^tBu)₂, Au-Cz and Au-Cz-(^tBu)(CF₃), broad and featureless spectra are consistent with emission from the intra-molecular CT state. Conversely, for Au-Cz-(CF₃)₂ the observed structure in the emission is characteristic of a vibronic progression of a transition from the ligand-centred excited state to the ground state. This is consistent with the energies of CT and ^3LE states shown in table 4.1 where for Au-Cz-(CF₃)₂ the strong electron-withdrawing effect of the double-CF₃ substitution has forced the CT state energy above that of the ^3LE state.

OLED devices were fabricated in architecture 1 (figure 4.2) in the case of Au-Cz-(^tBu)₂, and architecture 2 for Au-Cz-(CF₃)₂ and Au-Cz-(^tBu)(CF₃) to ensure confinement of excited states within the EML for the blue-emitting materials. To investigate whether spectral shifts observed in Au-Cz could be generalised to other CMA materials, devices were fabricated with host-free EMLs and EMLs incorporating hosts of varying polarity. DPEPO, with a

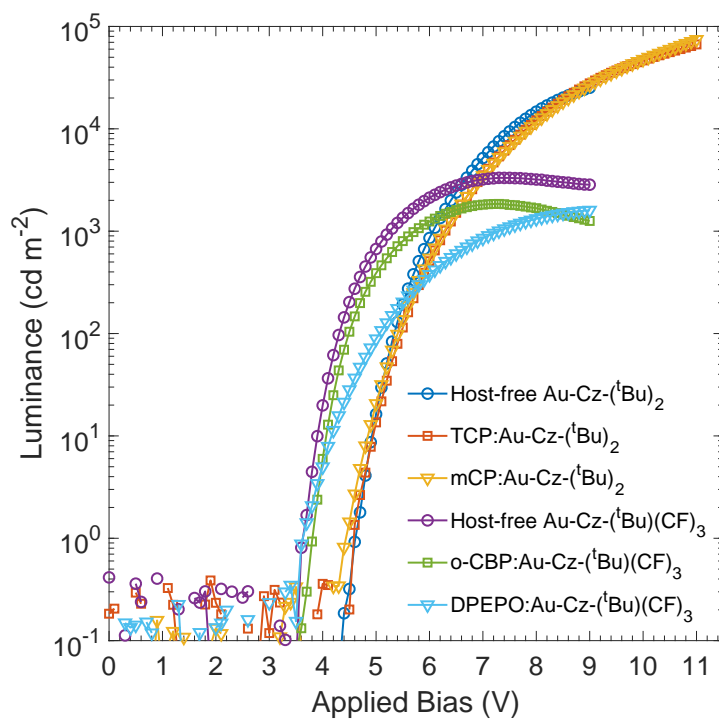
ground state dipole moment of 8 D, was used as a highly polar host for the blue emitting materials Au-Cz-(CF₃)₂ and Au-Cz-(^tBu)(CF₃).[96] Given its HOMO and LUMO energies of -6.4 eV and -2.0 eV and high T₁ energy of 3.4 eV, DPEPO is expected to provide good charge and excited state confinement in the blue emitting materials.[95] TCP and mCP were used as non-polar and polar hosts for Au-Cz-(^tBu)₂ but were deemed unsuitable for use in blue devices on account of both materials having T₁ energy of 2.9 eV and would hence potentially provide poor excited state confinement.[59, 103] Phosphine oxide based materials such as DPEPO are often used as hosts in blue-emitting OLEDs on account of their high triplet energies. However they are often highly polar. Identifying lower polarity host materials with sufficiently high triplet energies can be a challenge. In this case o-CBP, with ground state dipole moment 2.2 D, was used as a low-polarity host for blue emitters and can be used to show the progression in electroluminescence spectrum between host-free devices and those incorporating low and high-polarity hosts. The J-V and η_{eqe} -J characteristics of Au-Cz-(^tBu)₂ and Au-Cz-(^tBu)(CF₃) OLED devices are shown in figure 4.20 and the associated η_{eqe} curves are shown in figure 4.21. Au-Cz-(^tBu)₂ OLEDs typically show turn-on voltages of 4.5 V which, surprisingly, is higher than those seen for Au-Cz OLEDs despite using the same device structure and having similar HOMO and LUMO energies. Also contrary to the behaviour observed in Au-Cz, the η_{eqe} of Au-Cz-(^tBu)₂ appears to be heavily host dependent with peak values of 11.8 %, 18.7 % and 21.4 % for host-free Au-Cz-(^tBu)₂, mCP: Au-Cz-(^tBu)₂ and TCP: Au-Cz-(^tBu)₂ emissive layers respectively. The lower η_{eqe} for host-free devices is reflected in η_{plqe} measurements. The η_{plqe} of host-free Au-Cz-(^tBu)₂ was found to be 43% using an excitation wavelength of 405 nm. This compares with 78% in an mCP: Au-Cz-(^tBu)₂ film and 65% in a TCP: Au-Cz-(^tBu)₂ film. However it should be noted that these measurements, similarly to device characterisation, were made in air. While the lower measured η_{plqe} of host-free Au-Cz-(^tBu)₂ is consistent with device behaviour, it could possibly also be an effect of triplet quenching by oxygen, which may be suppressed in host:guest films. Au-Cz-(^tBu)(CF₃) OLEDs show $V_{on} \approx 3.7$ V which is more similar to those seen in Au-Cz and suggests that, despite the shallow LUMO of TSPO1, there are not significantly larger potential barriers to charge injection or transfer in architecture 2 than architecture 1. The η_{eqe} performance of Au-Cz-(^tBu)(CF₃) OLEDs is similar between varying hosts with peak $\eta_{eqe} = 17.2\%$ for both host-free and o-CBP: Au-Cz-(^tBu)(CF₃) emissive layers. It was not possible to make a reliable measurement of η_{plqe} for Au-Cz-(^tBu)(CF₃) as the absorption is too weak at the highest-energy excitation wavelength available of 405 nm. Additionally there is significant spectral overlap between the tails of photoluminescence and laser emission. However it can be inferred from the similar device performance between host-free Au-Cz-(^tBu)(CF₃) and o-

CBP: Au-Cz-(^tBu)(CF₃) emissive layers that Au-Cz-(^tBu)(CF₃) does not display a significant concentration-dependent luminescence quenching effect. Efficient blue emission at CIE co-ordinates (0.17, 0.20) and $\eta_{eqe} = 18.9\%$ has been achieved from Au-Cz-(^tBu)(CF₃) in a DPEPO host. While phosphine oxide based materials such as DPEPO are usually considered to be primarily electron transporting and carbazole based materials such as o-CBP are usually considered to be primarily hole transporting, no clear difference in charge balance was observed between devices containing DPEPO or o-CBP hosts. It should be noted that the luminance of Au-Cz-(^tBu)(CF₃) devices appears to be limited to $\sim 10^3$ cd m⁻². On further increases to the current density the luminance begins to decrease in a non-reversible process, possibly suggesting the onset of material degradation.

Electrical characterisation of devices incorporating Au-Cz-(CF₃)₂ as the emissive material was not possible due to rapid degradation on timescales of ~ 1 s including spectral bleaching of the emission. However it is apparent that the trend in electroluminescence emission spectrum with varying side group substitutions, as shown in figure 4.22, is similar to the photoluminescence trend. Additionally the blue shift observed on dilution of Au-Cz and subsequent further blue shift with increasing host polarity is seen in both Au-Cz-(^tBu)₂ and Au-Cz-(^tBu)(CF₃). A blue shift in emission is not observed in Au-Cz-(CF₃)₂ on dilution in DPEPO, which is consistent with the interpretation that emission is coming from a ³LE state, the energy of which will not be affected by a polar environment. Through the substitution of side groups it is therefore possible to shift peak electroluminescence from 549 nm in Au-Cz-(^tBu)₂ to 424 nm in Au-Cz-(CF₃)₂ with a change in CIE colour co-ordinates from (0.38, 0.55) to (0.16, 0.05). The wide range of electroluminescence colours spanned by this series of CMA molecules is shown in the CIE colour space chart in figure 4.22b and demonstrates the versatility of the CMA molecular motif. It is again noted that despite the deep-blue electroluminescence emission, viable devices could not be fabricated using Au-Cz-(CF₃)₂ as the emitting material due to rapid degradation. However, efficient blue OLED devices have been demonstrated using an emissive layer of Au-Cz-(^tBu)(CF₃) doped in DPEPO with peak $\eta_{eqe} = 18.9\%$ at CIE co-ordinates (0.17, 0.20).



(a) J-V characteristics



(b) L-V characteristics

Fig. 4.20 a) J-V and b) L-V characteristics of OLED devices incorporating Au-Cz-(^tBu)₂ and Au-Cz-(^tBu)(CF₃)

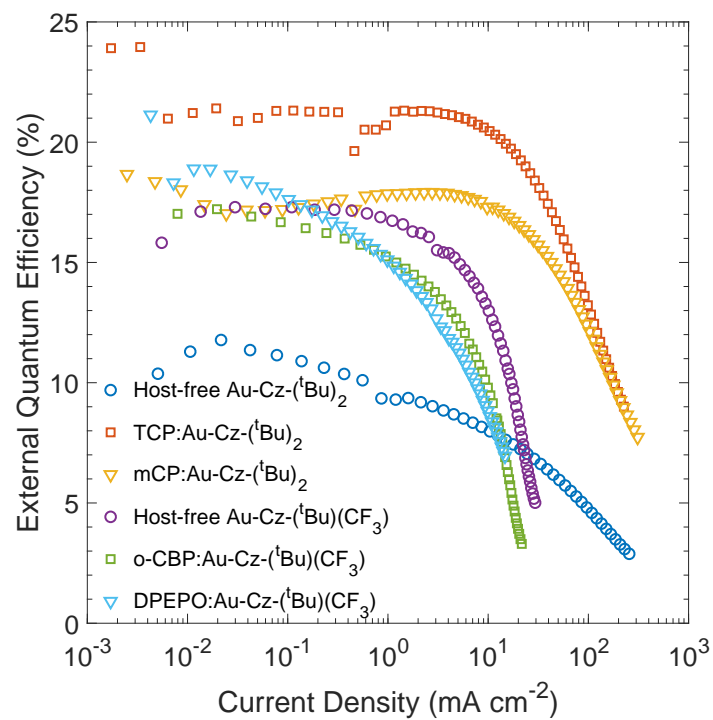
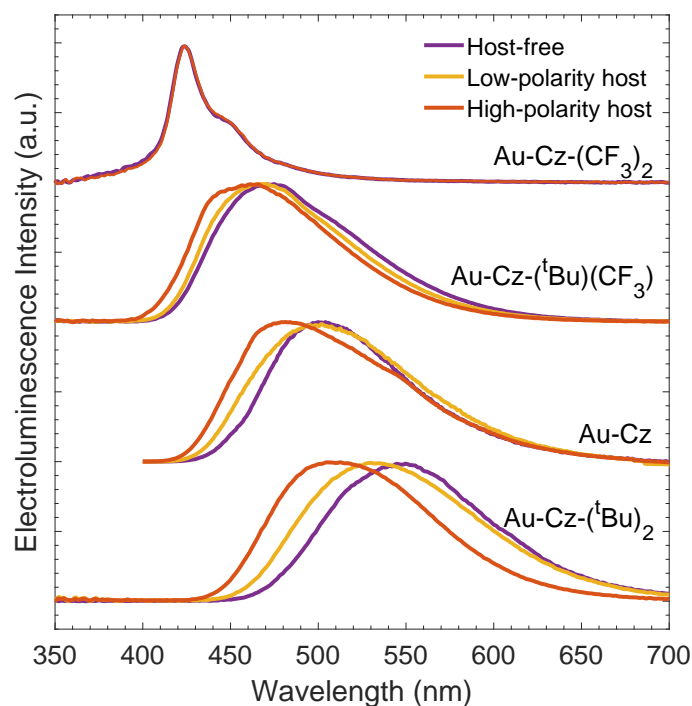
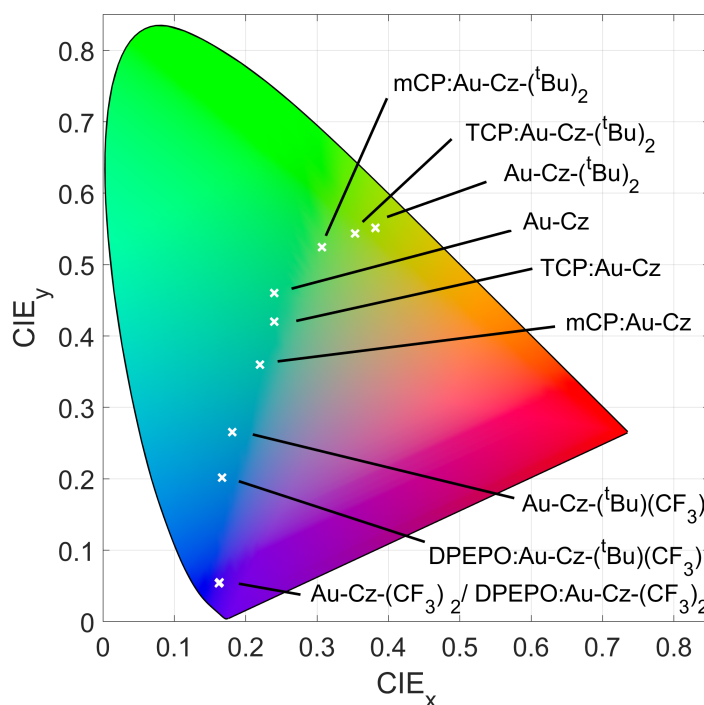


Fig. 4.21 η_{eqe} as a function of current density for Au-Cz-(^tBu)₂ and Au-Cz-(^tBu)(CF₃) OLEDs of varying host polarity



(a) Electroluminescence spectra



(b) CIE colour space

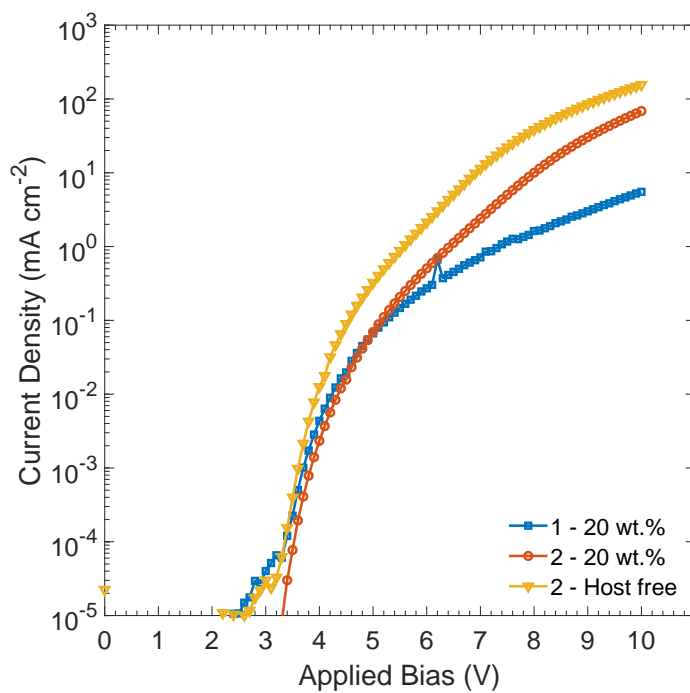
Fig. 4.22 a) Electroluminescence spectra and b) CIE colour space diagram for OLED devices incorporating gold-centred CMA emitters. Spectra were measured at approximately 100 cd m⁻²

4.4.2 Silver-centred CMA OLEDs

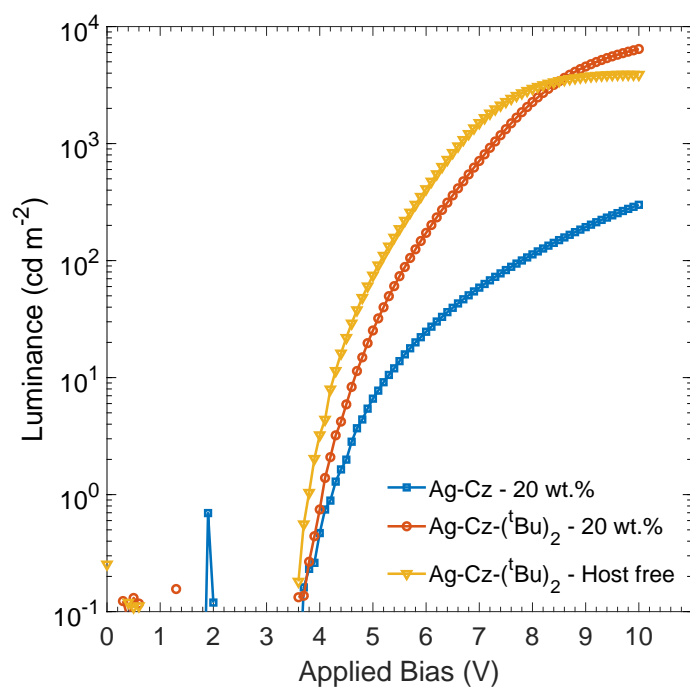
The central metal atom plays an important role in CMA molecules. The metal creates geometrical separation between electron-donating amide and electron-accepting carbene moieties while also creating a weak electronic bridge through its d orbitals.[84] Additionally the presence of the metal provides enhanced spin-orbit coupling in comparison to all-organic materials. As discussed, efficient emission and high-performance devices have been demonstrated using gold-centred CMA materials. Further emitter optimisation and elucidation of the role of the metal can be investigated by substitution through the coinage metal series.

Various organometallic compounds based on copper have previously been investigated for their emission properties. On account of its lower atomic number, the phosphorescent lifetime of copper compounds are often orders of magnitude longer than conventional iridium or platinum emitters.[63, 104] However TADF behaviour has been observed in some organocopper compounds which could allow their use in efficient OLEDs with large cost advantages over iridium or platinum.[65] Copper-centred CMA materials have been reported in OLED devices displaying blue-shifted electroluminescence in comparison to their gold-centred analogues but with lower device η_{eqe} and longer photoluminescence emission lifetimes.[81, 84]

In spite of previous reports of both gold and copper-centred emitting materials, there are no previous reports of OLEDs based on mononuclear silver in the literature. In this thesis OLED devices utilising silver-centred analogues of Au-Cz and Au-Cz-(^tBu)₂ were investigated. The molecular structures of compounds Ag-Cz and Ag-Cz-(^tBu)₂ are detailed in table 4.1. Due to the similarity in their HOMO and LUMO levels to Au-Cz, the silver-centred materials were substituted into device architecture 1 (figure 4.2). Figures 4.23a and 4.23b show current density and luminance plotted against applied bias for Ag-Cz and Ag-Cz-(^tBu)₂ dispersed in mCP as a host at 20 wt.% and in a host-free configuration for Ag-Cz-(^tBu)₂. The turn-on voltage is 4.3 V for both materials in an mCP host and 4.0 V for Ag-Cz-(^tBu)₂ in a host-free device. It can be seen that the current density tends to be lower at a given applied bias in devices containing compound Ag-Cz, possibly indicating lower charge mobilities. It is apparent from figures 4.23b and 4.24 that the luminance and the η_{eqe} are also much lower for Ag-Cz than for Ag-Cz-(^tBu)₂. This is in contrast to a similar comparison between gold-centred CMA materials with and without tertiary-butyl side groups and suggests that the effect of substituent groups on device performance is multi-parametric.



(a) J-V Characteristic



(b) L-V Characteristic

Fig. 4.23 a) Current density - Voltage and (b) Luminance - Voltage characteristics for silver-centred CMA OLEDs

The η_{eqe} is displayed as a function of current density in figure 4.24. The highest efficiency was found for mCP:Ag-Cz-(^tBu)₂ which showed a stabilised η_{eqe} of 13.0%. While this is lower than has been observed in devices incorporating equivalent gold-centred materials, it still implies some emission originating from triplet states. However efficiency roll-off is more severe than was seen in gold-centred materials with luminance at 90% of peak η_{eqe} equal to only 313 cd m⁻². Additionally substantially lower performance is seen in host-free devices with peak $\eta_{eqe} = 8.8\%$ suggesting that concentration-dependent luminescent quenching is a larger problem for silver-centred CMA emitters than has been seen for gold-centred materials. Devices based on Ag-Cz showed surprisingly poor performance, especially in comparison to analogous Au-Cz devices. The peak η_{eqe} of 4.1% is too low to provide evidence of triplet utilisation. The device performance can be correlated with η_{plqe} measurements which was found to be 19% for a film of Au-Cz and 45% for Au-Cz-(^tBu)₂.

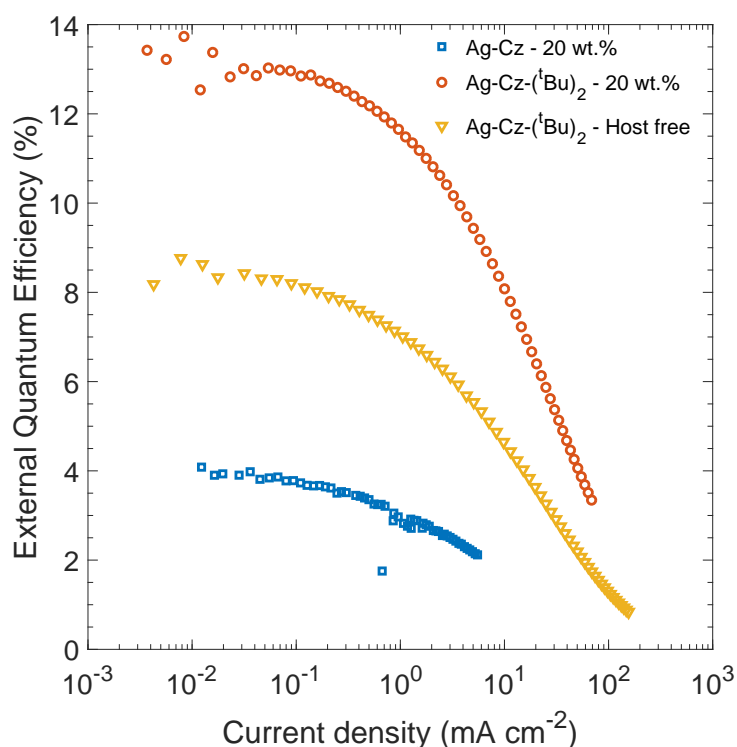


Fig. 4.24 η_{eqe} as a function of current density for silver-centred CMA OLEDs containing compounds Ag-Cz and Ag-Cz-(^tBu)₂ in an mCP host and host-free emissive layers

Room temperature time-resolved photoluminescence data for Ag-Cz and Ag-Cz-(^tBu)₂ are shown in figure 4.25. It is evident that prompt fluorescence is much more significant for Ag-Cz than for its gold-centred equivalent, Au-Cz. In Ag-Cz 20% of emission occurs within the first 5 ns which suggests either that intersystem crossing is slower or that non-radiative

triplet decay is faster than in Au-Cz. Prompt fluorescence is also significant in Ag-Cz-(^tBu)₂ with 6% of emission occurring in the first 5 ns. This is taken to indicate that intersystem crossing is less efficient in silver-centred CMA materials, which could further indicate that spin-orbit coupling mediated by the metal atom is the primary method for exciton spin interconversion in CMA materials. The lower atomic number of silver in comparison to gold may therefore explain the lower performance of Ag-Cz and Ag-Cz-(^tBu)₂ OLEDs in comparison to their gold-centred analogues.

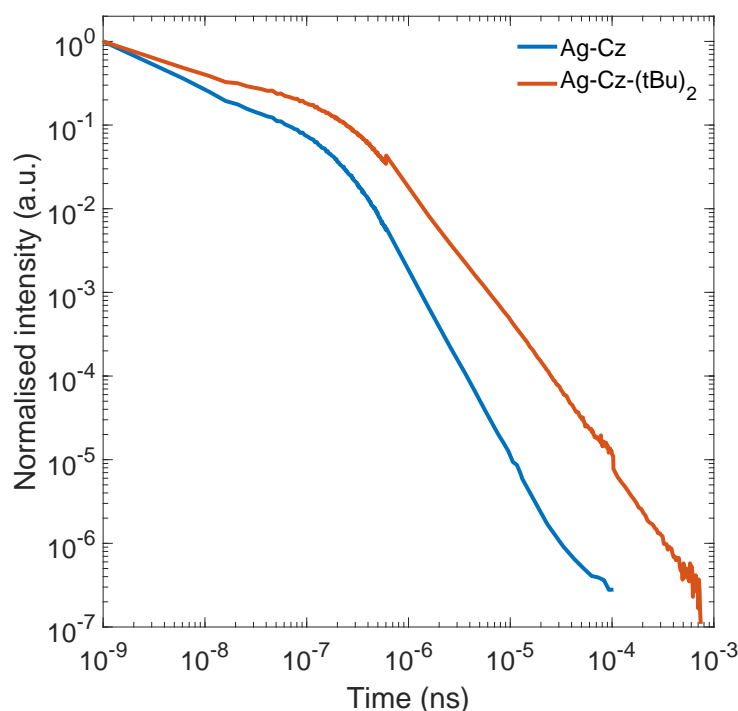


Fig. 4.25 Room temperature transient photoluminescence kinetics of silver-centred CMA materials Ag-Cz and Ag-Cz-(^tBu)₂

4.5 Discussion

Thermally evaporated OLEDs incorporating gold-centred CMA emitters have been demonstrated showing improved reproducibility in comparison to solution-processed variants. $\eta_{eqe} > 25\%$ is consistently achieved for the green emitter, Au-Cz, using a TCP host. Efficient devices with η_{eqe} up to 23.1% have also been produced using a host-free Au-Cz emissive layer, though at a cost to reproducibility. The observed electroluminescence spectrum is in all cases distinct and blueshifted from that seen in solution-processed devices, which is

considered to arise from the different chromophore morphology achieved through vacuum deposition.

The η_{plqe} of evaporated Au-Cz films has been shown to exhibit limited sensitivity to emitter concentration with $\eta_{plqe} = 86\%$ dispersed in an mCP host at 20 wt.% with only a small drop to $\eta_{plqe} = 83\%$ in a host-free film. This insensitivity may offer an insight into the high performance of solution-processed CMA devices previously reported, for which dopant aggregation is difficult to avoid, and explains the surprising effectiveness of host-free evaporated devices. It has been shown that host-free Au-Cz emissive layers exhibit comparably shorter emission lifetimes than those utilising dilute guests, with consequent advantages gained through simplification of the manufacturing process, simpler triplet management, and reduced average triplet density in the emissive layer. Reducing average triplet density has previously been shown to extend device lifetime. [62] Additionally, host materials can themselves pose a source of device instability.[105–107]

It has been found that host polarity can provide a method to shift both the absorption edge and emission peak of Au-Cz ranging from mid-green to sky-blue. Further, an investigation into OLED devices incorporating gold-centred CMA emitters with varying side group substitutions showed that emission colour could be varied over a wide range from yellow, with CIE co-ordinates (0.38, 0.55) to deep-blue, CIE (0.16, 0.05). With the exception of the deep-blue emitter, Au-Cz-(CF₃)₂, the materials exhibited similar emission characteristics with broad, unstructured emission which is symptomatic of an intramolecular CT state. The electron-donating or withdrawing character of the substituent side groups determined the CT state energy and hence modified the emission colour. Critically the ³LE energy is less sensitive to side group substitution and in the case of Au-Cz-(CF₃)₂, with two strongly electron-withdrawing CF₃ groups, became lower in energy than the CT state. Consequently emission from Au-Cz-(CF₃)₂ was found to be structured and insensitive to host environment.

On substitution of the central metal for silver it is apparent that prompt fluorescence contributes a greater component of total photoluminescence. This is possibly a result of a lower rate of intersystem crossing in silver-centred materials. The first reported example of mononuclear silver complexes as OLED emitters has been shown. However the best-performing device η_{eqe} of 13.0% was lower than for equivalent gold-centred materials. This could indicate a lower efficiency of triplet emission in silver-centred materials, possibly due to the lower spin-orbit coupling strength of silver in comparison to gold.

4.6 Conclusion

It is concluded that in evaporated device stacks, dynamic reorganisation of the solid lattice around an excited molecule is unlikely to occur, at least on the timescale of emission. It has therefore been discovered that the CT state energy and hence emission colour can be blue shifted through control of the polar environment surrounding CMA molecules while maintaining efficient sub-microsecond emission from triplet states. However it has also been found that the large ground state dipole of Au-Cz does not itself affect the emission wavelength of adjacent excited molecules. It has been established that these relatively complex molecules maintain their excellent performance characteristics when employed in a vacuum-deposited architecture. The versatility of the CMA molecular motif has been demonstrated with variations to molecular design allowing the possibility of selecting emission colour over a wide range from yellow to blue while maintaining good device performance. Additionally minimising the energy gap between CT and LE states was not found to improve device performance through more efficient triplet utilisation as might be expected if the spin-vibronic model of intersystem crossing could be applied to CMA materials. The LE state is found to impose a high energy limit on how far emission colour can be tuned, which is in the deep blue for carbazole based donor moieties.

Chapter 5

The mechanism of intersystem crossing in a benchmark TADF material

5.1 Introduction

As discussed in section 2.4.4, ESR can be used to detect triplet states and determine their properties. The pattern of absorption and emission features in a triplet ESR spectrum is dependent on the relative populations of the triplet substates and is hence characteristic of the mechanism of triplet formation. Additionally the zero-field splitting parameters D and E can be determined, which can reveal the energy separation of triplet substates at zero field. The first observation of triplet states in organic semiconductors using ESR was made in 1958 in naphthalene.[108] Since then ESR has been used extensively in the study of processes as diverse as photosynthesis, avian magnetoreception and charge separation in OPVs.[109–111]

As discussed in section 2.3.3, there has been much deliberation in the literature on the mechanism of inter-system crossing in TADF materials. The ability of ESR to reveal triplet properties makes it an ideal tool to provide evidence to inform the debate. In one ESR study on TADF materials by Ogiwara et al., it was found that 4CzIPN — a benchmark TADF molecule — in a frozen toluene solution displayed an absorption (A) and emission (E) pattern of AEEAAE indicative of intersystem crossing being mediated by the hyperfine interaction.[112] In contrast, a different study by Evans et al. used the same methods but puzzlingly found a different absorption and emission pattern of EEEAAA which was modelled as being consistent with a spin-orbit coupling mediated intersystem crossing with vibrational coupling allowing a redistribution of the triplet sub-state populations.[21] This result was used to support the spin-vibronic model of ISC in TADF materials discussed

in section 2.3.3, at least in the case of isolated molecules as found in dilute ($\approx 500 \mu\text{M}$) solution.

This lack of reproducibility between nominally similar studies provides justification for further investigation. Additionally the reliance that the prevailing spin-vibronic model places on the vibrational environment of a molecule motivates an ESR study of 4CzIPN in solid films similar to those used in high-efficiency OLED devices. The vibrational behaviour of 4CzIPN is likely to be environment dependent as, for example, torsional motion or dihedral angle variation may be sterically hindered in highly aggregated phases. Olivier et al., found that both ΔE_{ST} and the strength of spin-orbit coupling depended on the torsional angle between the peripheral carbazole units and the central dicyanobenzene in 4CzIPN.[20] It was posited that dynamic twisting on the timescale of TADF emission allows conformational gating of the ISC and RISC processes, even in the bulk phase where it might be expected that proximity to adjacent molecules may hinder motion.

In this thesis, ESR data are presented to confirm the EEEAAA ESR pattern of 4CzIPN in dilute frozen toluene solution. Further, a novel ESR investigation into the intersystem crossing mechanism of 4CzIPN doped in 4,4'-Bis(N-carbazolyl)-1,1'-biphenyl (CBP) in solid film is presented. This mimics the environment in which high-performance OLEDs incorporating 4CzIPN as emitting material have been reported and is hence more relevant to practical uses of the material.[67] Evidence is found for a radical pair mediated intersystem crossing mechanism in low-concentration films, while for high concentration and pure 4CzIPN films it is found that the recombination of spin-correlated radical pair (SCRIP) states necessary for intersystem crossing is quenched by preferential charge separation. A mechanism for the observed concentration-dependent luminescence quenching in 4CzIPN is therefore proposed in contrast to previous hypotheses invoking energy transfer processes.[50, 113]

5.2 Collaborator contributions

ESR measurements were undertaken with the assistance of Dr William Myers at the Centre for Advanced Electron Spin Resonance (CAESR), University of Oxford. Low-temperature absorption measurements were made by Dr Ian Jacobs. Results were discussed extensively with Drs Emrys Evans and Leah Weiss.

5.3 Experimental methods

A solution of 4CzIPN was prepared at low concentration ($100 \mu\text{M}$) in toluene and loaded into a 3 mm diameter quartz ESR tube. The sample was degassed using a repeated freeze-pump-

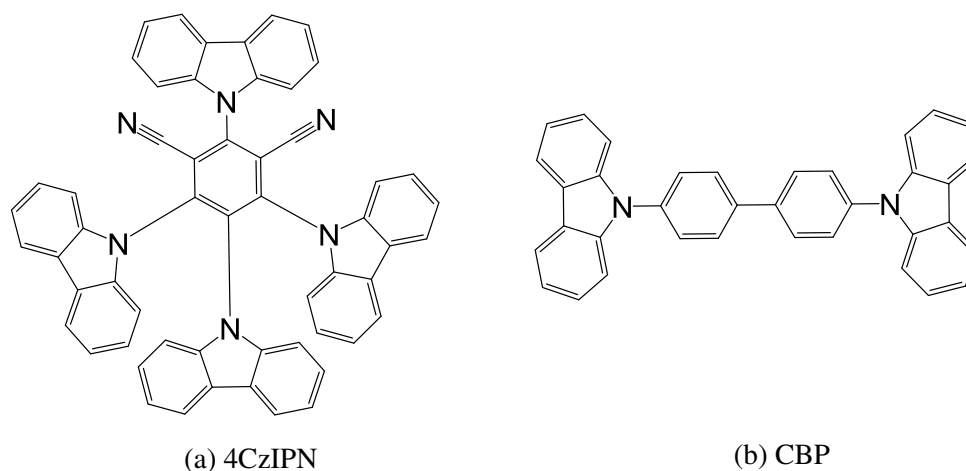


Fig. 5.1 Chemical structures of a) 4CzIPN and b) CBP

thaw method and flame sealed to prevent oxygen ingress. Film samples of pure 4CzIPN and 4CzIPN dispersed in a CBP host at concentrations of 1 wt.%, 5 wt.% and 50 wt.% were prepared by vacuum thermal evaporation onto thin (~ 0.2 mm) borosilicate glass cover slides cut into approximately 2 mm widths. The chemical structures of 4CzIPN and CBP are shown in figure 5.1. Thicker films were desirable to maximise optical density at the excitation wavelength and hence maximise the ESR signal. Given the practical difficulty of fabricating thick films at low 4CzIPN concentration the final film thicknesses at each concentration were 400 nm (1 wt.%), 300 nm (5 wt.%), 200 nm (50 wt.%) and 100 nm (100 wt.%). To further increase the recorded signal, six strips of film were stacked and loaded into each tube. The ESR tubes were evacuated to 10^{-5} mbar to exclude oxygen prior to flame sealing. The samples were frozen in liquid nitrogen and placed into the resonator which was liquid nitrogen cooled to 80 K. Pulsed laser excitation from a tunable optical parametric amplifier with repetition rate 20 Hz was used to excite the samples at 3 mJ per pulse. Under electrical excitation in an OLED device, excitons would be expected to preferentially populate lower energy states. For this reason an excitation wavelength of 460 nm was chosen which lies towards the low energy end of the molecular CT absorption band as shown in figure 5.2. The absorption edge of the host material, CBP, is at approximately 380 nm, so it can be assumed that excitations were solely generated on the 4CzIPN molecules. The absorption spectra of 4CzIPN, CBP and 50 wt.% CBP:4CzIPN films and 4CzIPN solution in toluene were measured at room temperature and 80 K. It was verified that there is no shift in absorption edge of either 4CzIPN or CBP at low temperature. Additionally Evans et al. showed that the ESR signal polarisation in 4CzIPN solutions was independent of excitation wavelength between 355 nm and 460 nm.

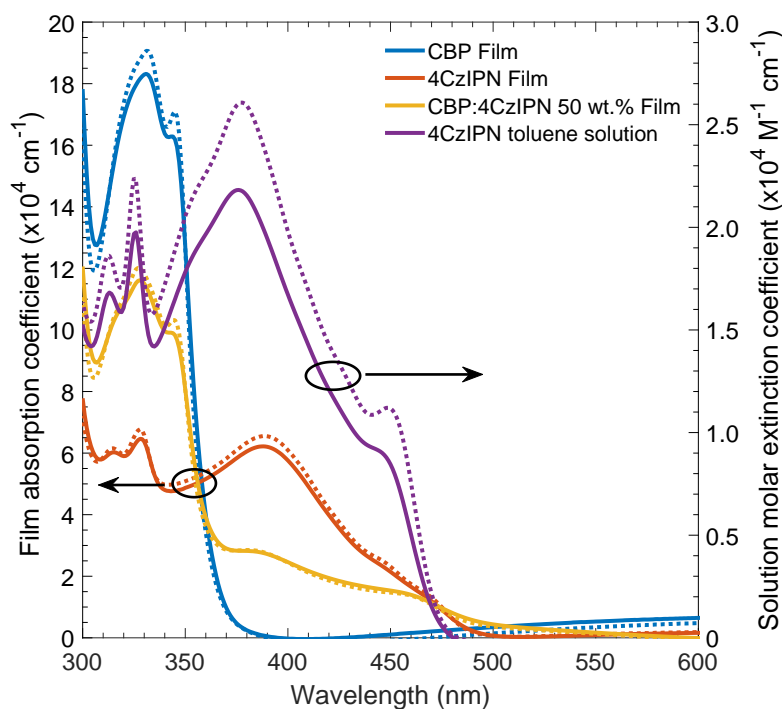


Fig. 5.2 UV-Vis absorption of 4CzIPN thin films and in toluene solution at room temperature (solid lines) and at 80 K (dotted lines)

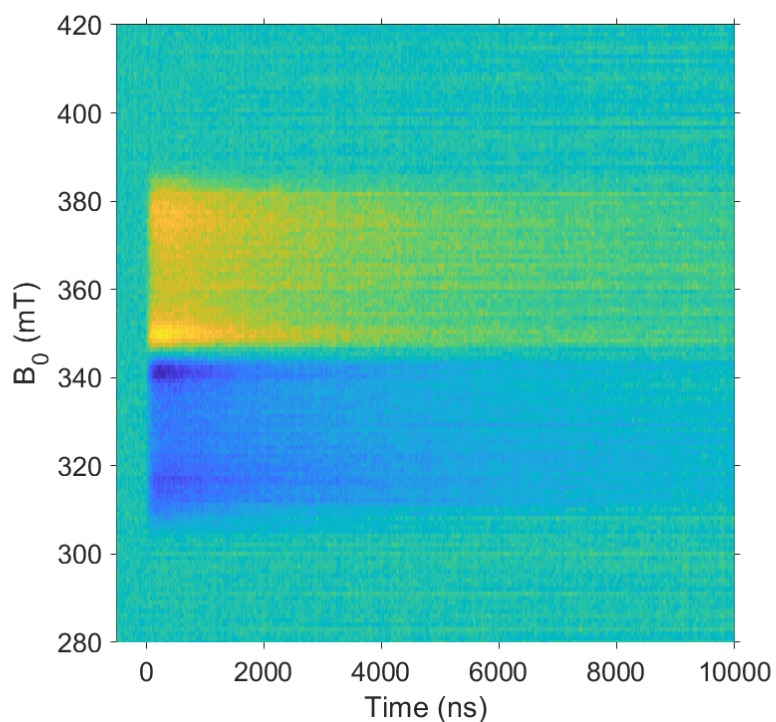
Resultant data were modelled using the EasySpin simulation package.[114] EasySpin calculates ESR transition energies based on the interactions described in section 2.4. The EasySpin function *pepper* accounts for random molecular orientations in a fixed geometry with respect to the magnetic field, B_0 , which we assume for frozen solution samples. In the case of thin-film samples a small correction was made to allow for preferential molecular alignment with the substrate. Simulated ESR spectra can therefore be plotted taking account of Zeeman, hyperfine and dipolar interactions with further line broadening added to account for disorder due to variations in molecular environment.

5.4 Results

Figure 5.3 shows transient ESR data as recorded from a sample of 4CzIPN in frozen 100 μM toluene solution. The ESR absorption/emission pattern is not found to be time dependent and reproduces the EEEAAA signal previously found by Evans et al.[21] The signal intensity initially increases following the laser pulse to a maximum after ~ 200 ns before decaying. The zero-field splitting parameters are found by the relative positions of transitions observed

from the different canonical orientations, as illustrated in figure 5.4, while the value of g is determined by matching the central position of the spectrum. A least-squares fitting method was used to determine the triplet sub-state populations of $P_X = 0.33, P_Y = 0.48, P_Z = 0.18$ and zero-field splitting parameters $|D| = 39$ mT and $|E| = 10$ mT. As shown in figure 5.4, the simulation is in good agreement with both the experimental data and the values of $P_X = 0.35, P_Y = 0.47, P_Z = 0.18$ and $|D| = 40$ mT and $|E| = 11$ mT reported by Evans et al.

(a)



(b)

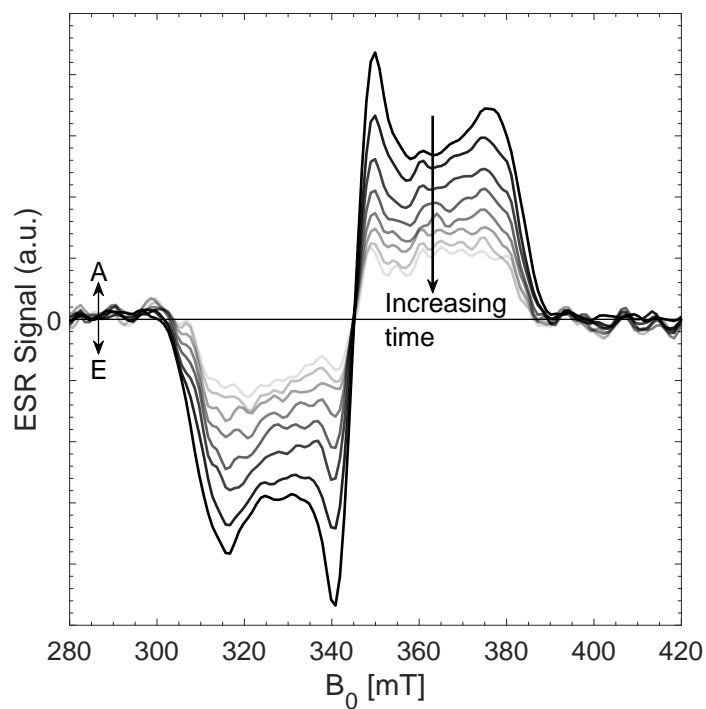


Fig. 5.3 a) Transient ESR data from a 4CzIPN sample in a 100 μ M frozen toluene solution at 80 K b) Time evolution of signal. Each line represents a summation of signal over a 1000 ns interval with earlier times represented by darker shading

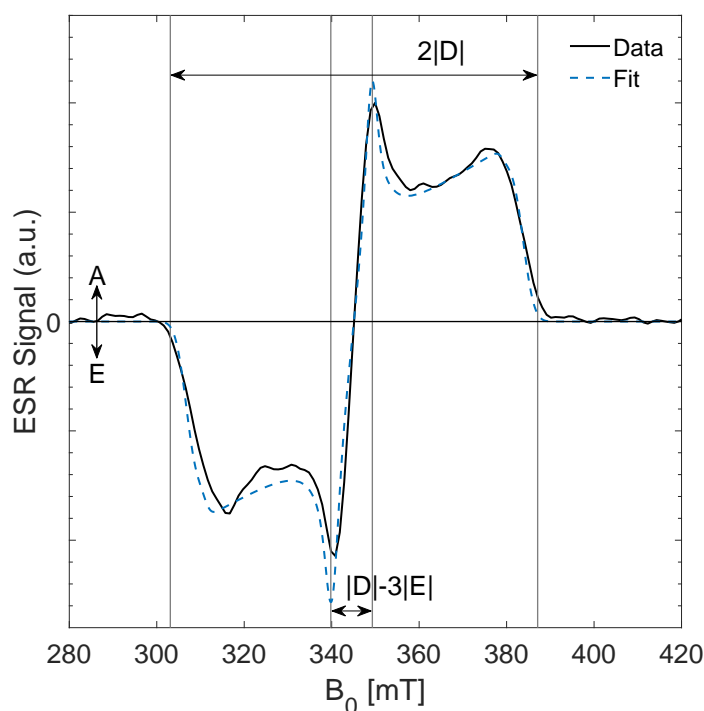


Fig. 5.4 ESR data for 4CzIPN in a frozen 100 μM toluene solution integrated over the first 1 ms following photoexcitation (solid line). The overlaid vertical lines denote positions of transitions along canonical orientations. Simulation (dashed line) parameters were found through a least-squares fitting method

Transient ESR data obtained from CBP:4CzIPN films are shown in figure 5.5. In contrast to the solution data, a time evolution in the ESR signal is evident. The evolution of the ESR spectra for 1 wt.% and 5 wt.% 4CzIPN films can be seen in figure 5.6. For the 5 wt.% film — which is used in optimised devices — a single absorptive peak is observed at times before 500 ns but the spectrum transitions to be dominated by an AEEAAE feature at times greater than 2000 ns. The signal strength initially increases as can be seen from the greater magnitude of the integrated signal from 501 to 1000 ns in comparison to that from 0 to 500 ns. The peak of the early-time signal ($t < 500$ ns) is at 347 mT but is asymmetric with a skew towards the low-field edge. The kinetic in figure 5.8 shows that the signal at 347 mT reaches a maximum at 550 ns before decaying. The more dilute 1 wt.% film shows a similar pattern however the signal to noise ratio is considerably lower due to the reduced optical density. It is noted however that the triplet signal emerges earlier than in the 5 wt.% film with some triplet contribution evident at $t < 500$ ns. Intriguingly the AEEAAE signal seen in the low-concentration 4CzIPN films is qualitatively similar to that observed in a dilute solution by Ogiwara et al.[112]

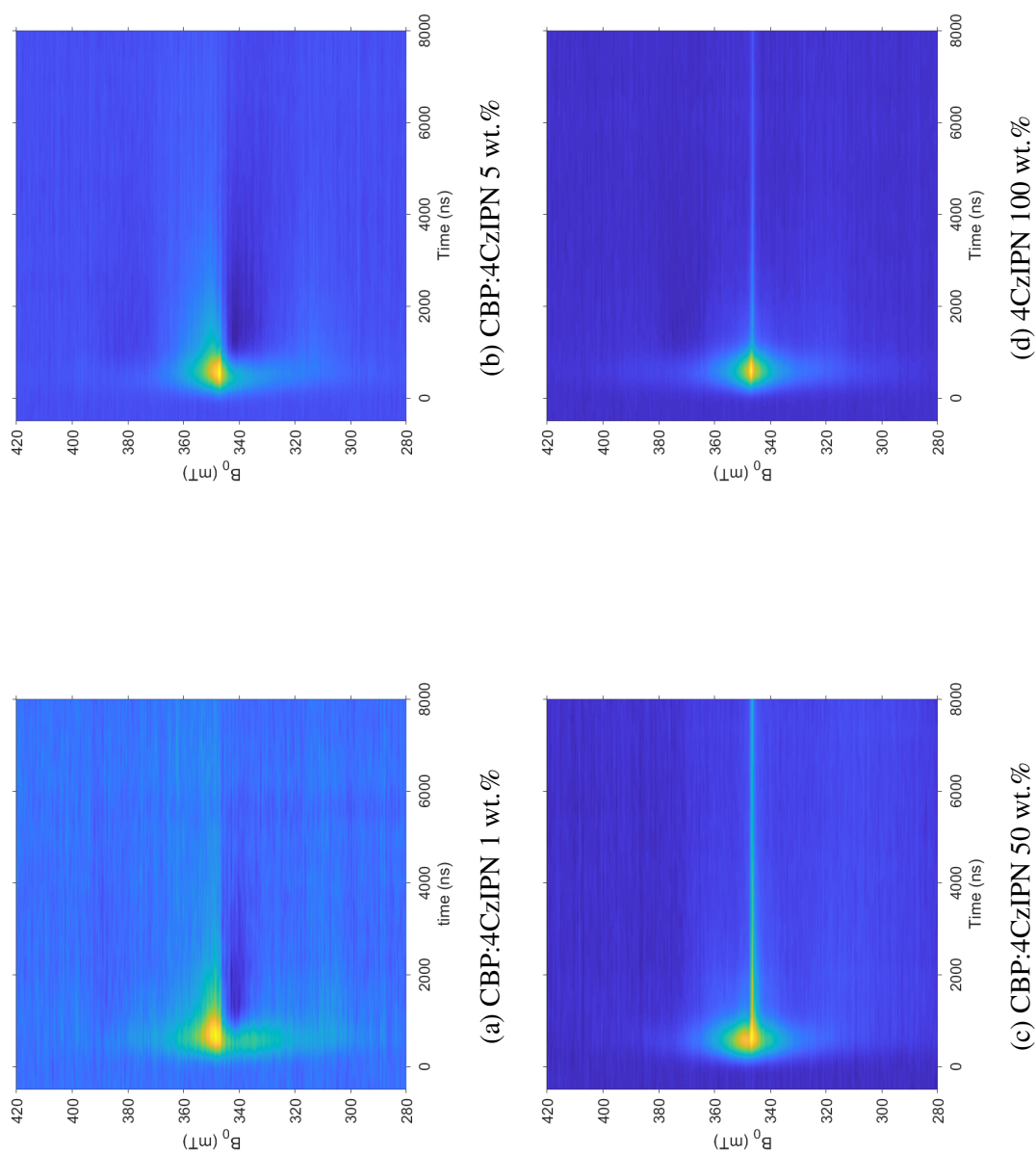
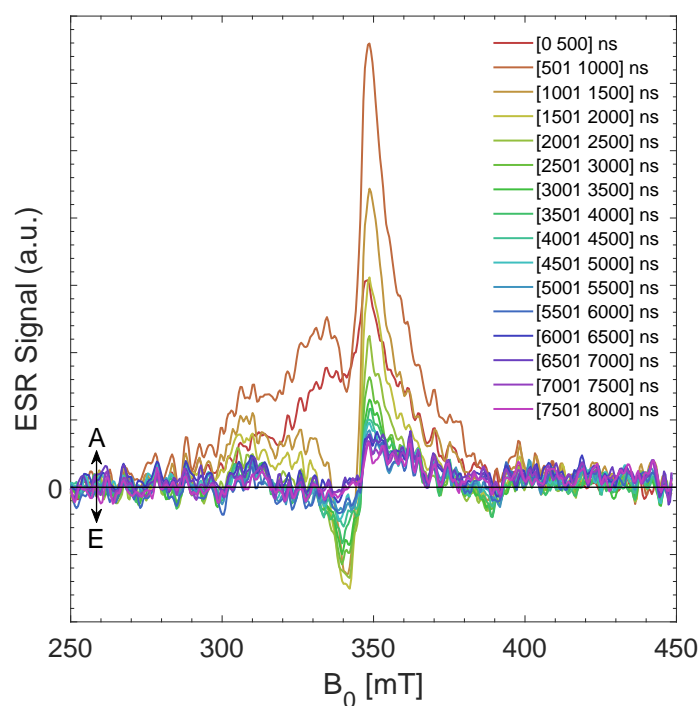


Fig. 5.5 Transient ESR data from thin films of 4CzIPN doped in a CBP host at (a) 1 wt.%, (b) 5 wt.%, (c) 50 wt.% and (d) host-free

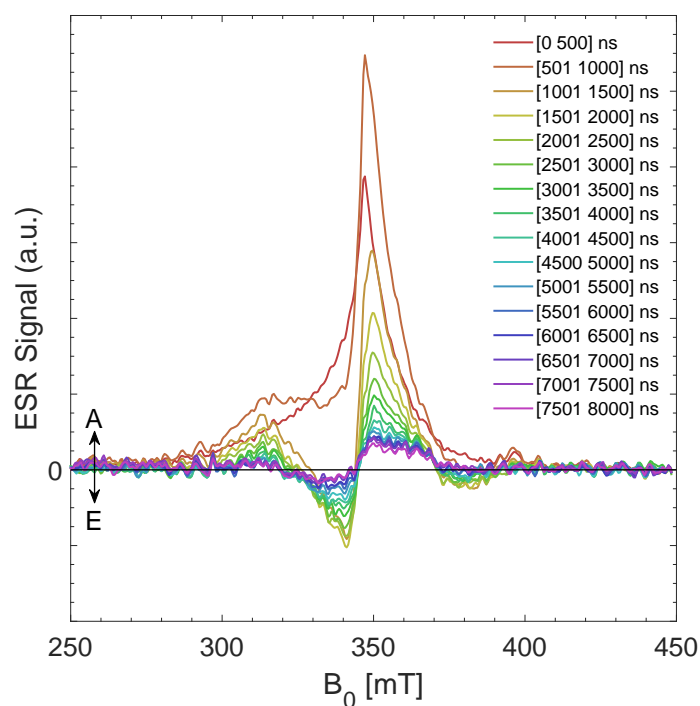
The single absorptive feature seen at early times in the 5 wt.% film is indicative of a $s = \frac{1}{2}$ species and as such is deduced to originate from polarons. As shown in figure 5.7a the broadened and skewed signal shape can be reproduced by simulating two different polarons with slightly shifted g -factors and varying line broadening. This can be rationalised by the differences in wavefunction between the HOMO, which is largely located on the four peripheral carbazole groups and the LUMO, which is primarily located on the central cyano-substituted phenyl group. Variation in the chemical environment of the different carbazole groups and an increase in vibrational and conformational degrees of freedom in comparison to the cyano groups means that it is likely that the broader ESR signal originates from the positive polaron while the narrower signal originates from the negative polaron. The deduction that the broader polaron signal is derived from the cation is supported by previous reports from both theoretical and experimental work that positive charges can delocalise between two or more carbazole moieties in a 4CzIPN molecule.[18, 20]

The AEEAAE feature which emerges after 500 ns and which is dominant at times greater than 2000 ns is characteristic of a triplet exciton which has been formed from the geminate recombination of spin-correlated radical pairs. As discussed in section 2.2.2, SCRPs states originating from a photoexcited singlet have strong mixing between singlet, $|0,0\rangle$, and triplet, $|1,0\rangle$, states. Upon recombination of SCRPs states both singlet and triplet excitons can therefore be formed, however it is only the triplet, and not the singlet, excitons that are detectable in ESR. In an ESR experiment SCRPs-mediated triplets are formed in a high-field condition with the consequence that Zeeman splitting between triplet states of varying m_s makes the $|1,+1\rangle$ and $|1,-1\rangle$ states inaccessible. As a result of both spin-selection and the Zeeman induced energetic offset the $|1,0\rangle$ state is exclusively populated and the observed AEEAAE pattern is produced as a result. The origin of the AEEAAE pattern from exclusive population of the $|1,0\rangle$ state is illustrated in figure 5.9 with arrows representing resonant transitions; absorption (A) is depicted by an upward arrow while emission (E) is depicted by a downward arrow.

Figure 5.10a shows the evolution of ESR spectra with time for films of 50 wt.% of 4CzIPN dispersed in CBP and host-free 4CzIPN. In the case of these higher concentration films it is apparent that the signal is dominated by an $s = \frac{1}{2}$ polaron signature which narrows and decays over time. In both cases, and similarly to the more dilute films, the signal before 1000 ns can be modelled as the sum of two polarons with shifted g -factors relative to each other and variations in broadening with the narrower polaron expected to be attributable to the anion. The early-time modelling of the polaron signal is shown in figure 5.11a for the host-free film. From 1000-2000 ns the anion signal narrows which permits the visualisation of a weak AAEEA triplet signal which is either not present or is masked by

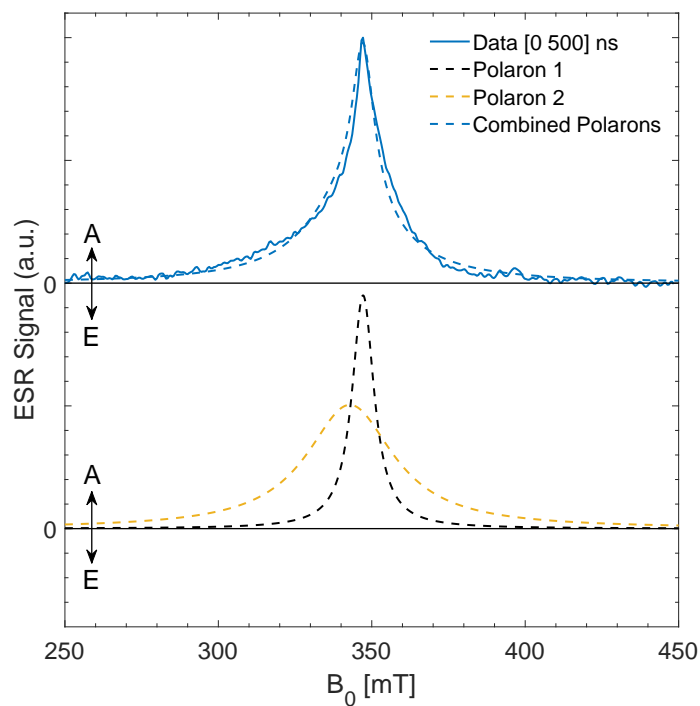


(a) CBP:4CzIPN 1 wt.%

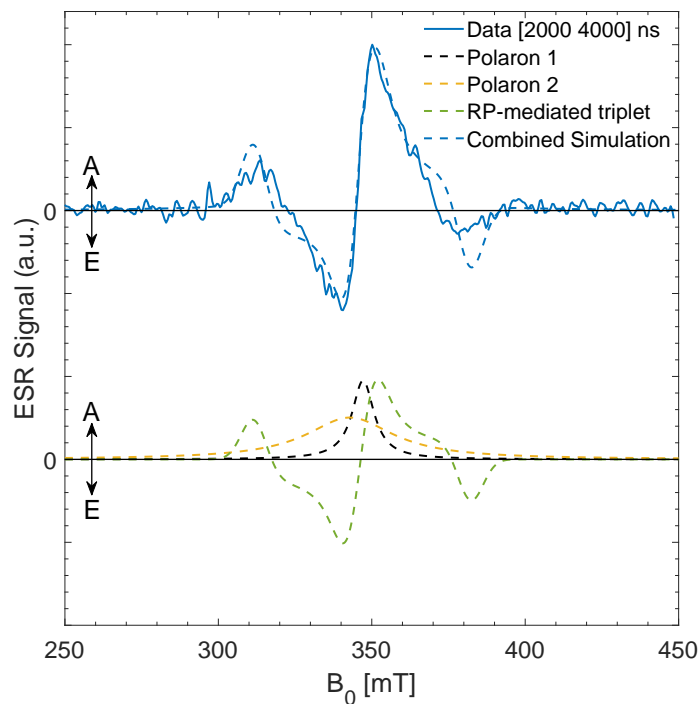


(b) CBP:4CzIPN 5 wt.%

Fig. 5.6 Time evolution of ESR signal for a) 1 wt.% and b) 5 wt.% films of 4CzIPN dispersed in CBP. Each line represents a summation of signal over a 500 ns interval with earlier times represented by redder colours. For clarity raw data has been smoothed using a 5-point moving average equivalent to a 4 mT window width



(a) 0-500 ns



(b) 2000-4000 ns

Fig. 5.7 Tr-ESR data for a film comprising 5 wt.% of 4CzIPN in a CBP host integrated over (a) the first 500 ns and (b) between 2000 ns and 4000 ns post laser pulse, modelled as a combination of polarons and radical-pair mediated triplets

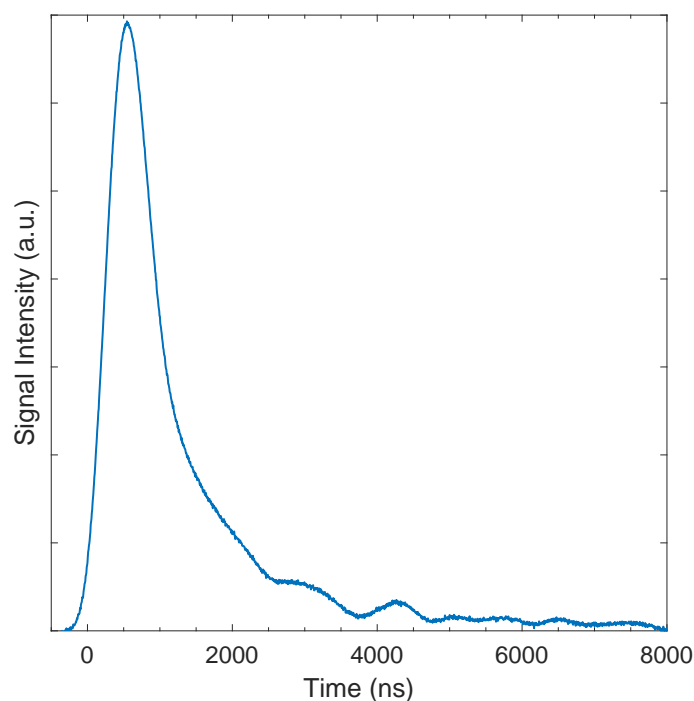


Fig. 5.8 CBP:4CzIPN 5 wt.% transient ESR kinetic at 347 mT

the polaron signal at times less than $t < 1000$ ns. At times greater than 2000 ns the signal decays without further evolution. Interestingly an AAEAE signal is indicative of triplets formed through spin-orbit coupling and, as shown in figure 5.11b, can be simulated assuming triplet sub-level populations $P_Z > P_Y > P_X$. More precise fitting is not possible due to the weak nature of the signal but it is clear that the triplet polarisation pattern is distinct to the populations of $[P_X, P_Y, P_Z] = [0.35, 0.47, 0.18]$ giving rise to an EEEAAA spectrum in solution measurements. This may be expected due to the significantly different steric environments experienced by isolated molecules in a frozen toluene solution and closely packed molecules in a host-free thin film.

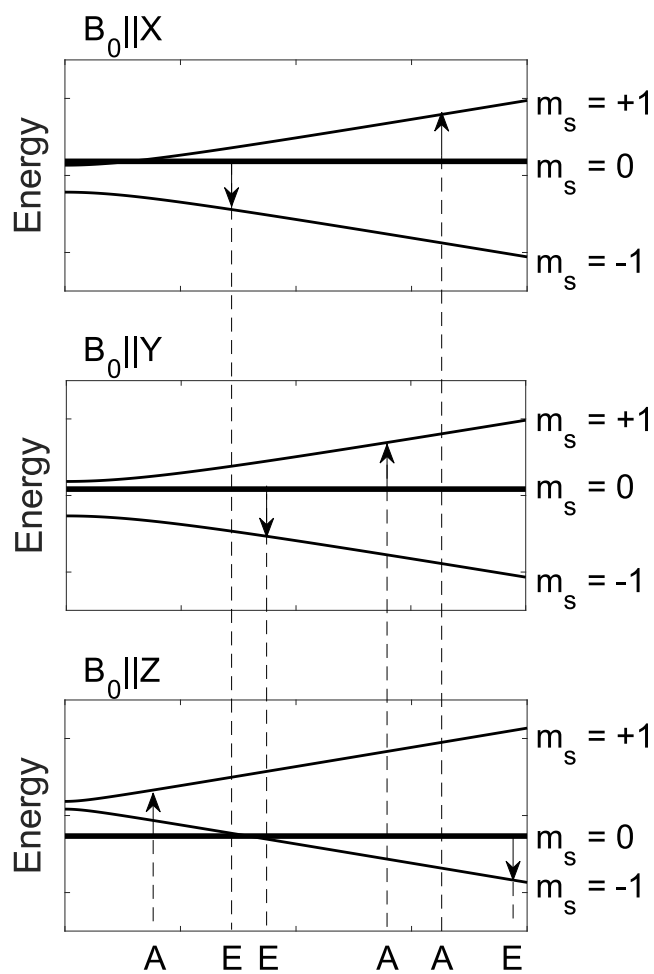
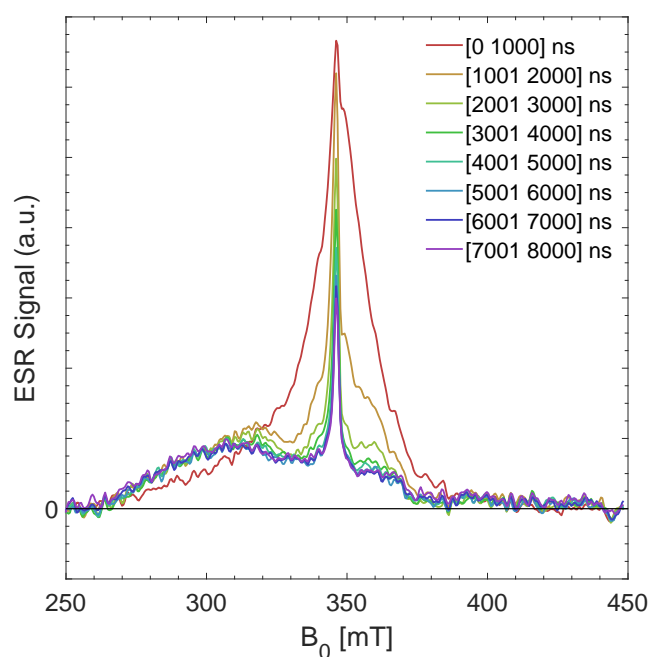
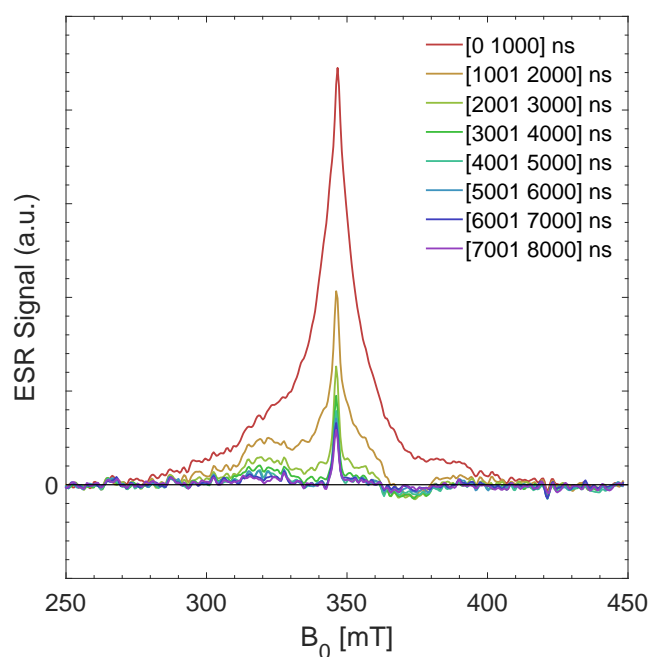


Fig. 5.9 An illustration of absorptive (A) and emissive (E) ESR transitions from an exclusively populated $|1,0\rangle$ state, showing the origin of an AEEAAE signal pattern

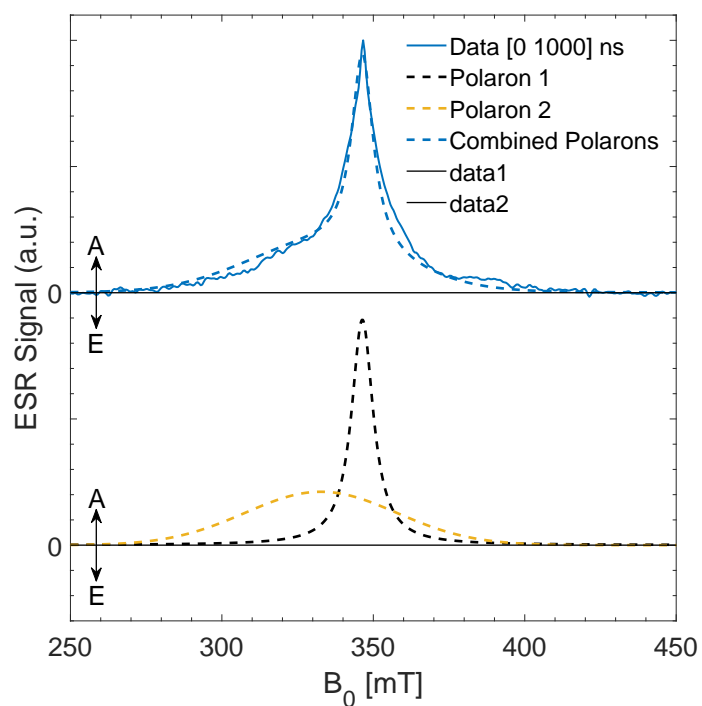


(a) CBP:4CzIPN 50 wt. %

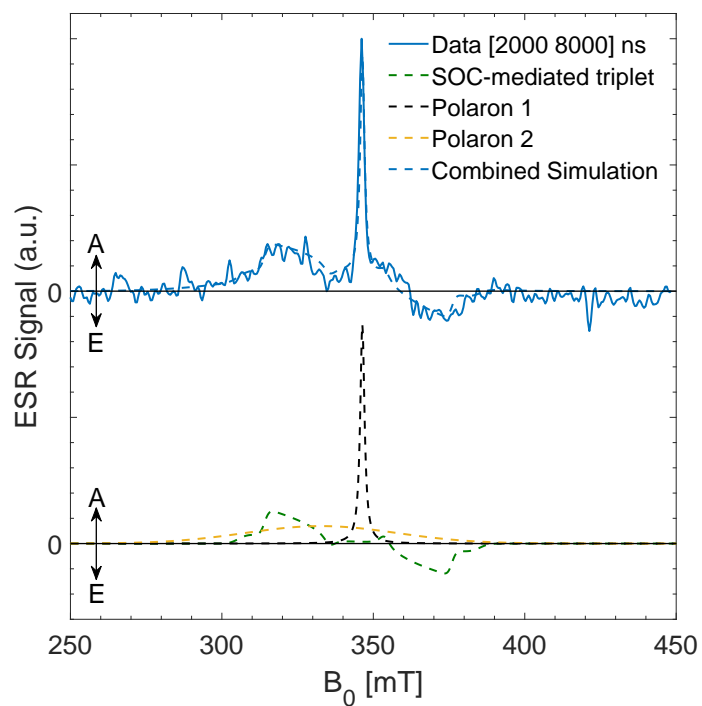


(b) Host-free 4CzIPN

Fig. 5.10 Time evolution of EPR signal for films of a) 50 wt.% of 4CzIPN dispersed in CBP and b) host-free 4CzIPN. Each line represents a summation of signal over a 1000 ns interval with earlier times represented by redder colours. For clarity raw data has been smoothed using a 5-point moving average equivalent to a 4 mT window width



(a) 0-500 ns



(b) 2000-8000 ns

Fig. 5.11 Transient ESR data for a host-free film of 4CzIPN integrated over (a) the first 1000 ns after the laser pulse and (b) between 2000 ns and 8000 ns after the laser pulse and modelled as a combination of polarons and radical-pair mediated triplets

5.5 Discussion

4CzIPN is an archetypal TADF material for OLEDs, so the mechanism of spin conversion from triplet to singlet excitons is of great interest. Transient ESR data from a dilute (100 μM) solution of 4CzIPN frozen in toluene at 80 K have been found to show an AAAEEE spectral pattern. This is consistent with previous measurements from Evans et al., and confirms those results in preference to conflicting results presented by Ogiwara et al. This spectral pattern is characteristic of a triplet exciton formed through spin-orbit coupling. The modelled sub-state populations of $[P_X, P_Y, P_Z] = [0.33, 0.48, 0.18]$ are in good agreement with those previously reported and are consistent with the prevalent spin-vibronic model of inter-system crossing which has been used to describe the excited state kinetics in 4CzIPN and other TADF materials. The observation that triplets form by spin-orbit coupling in frozen 4CzIPN solution suggests that the molecular vibrations, or dynamic torsional motions, deemed necessary for efficient intersystem crossing are not excessively hindered even in a solid matrix at 80 K.

While ESR has been used to support the spin-vibronic model in frozen solution samples of 4CzIPN, the operation of high-efficiency OLEDs is much more closely simulated by the study of solid films. The vibrational modes available to a 4CzIPN molecule in a solid film are likely to vary from those in the case of isolated molecules in dilute frozen solution. Additionally aggregation in solid films allows electronic communication between adjacent molecules. High-efficiency OLED devices can be fabricated using 4CzIPN dispersed at 5 wt.% in the host material CBP. In common with many OLED emitting materials, luminescence becomes less efficient at higher concentrations. It is clear from data presented in this thesis that the ESR signal and dynamics in solid films of 4CzIPN are distinct from those seen in dilute solution measurements. Through transient ESR measurements this study has shown direct experimental evidence that the dominant forward intersystem crossing mechanism in device-relevant 5 wt.% CBP:4CzIPN films is through an intermediate SCR_P state with spin-mixing mediated by hyperfine coupling. This in contrast to the vibrationally assisted spin-orbit coupling model which has been used to explain the forward intersystem crossing in dilute solution ESR measurements. The proposed kinetic scheme is illustrated in figure 5.12. Upon photoexcitation a singlet exciton is produced which undergoes charge transfer to a neighbouring molecule and in so doing creates a spin-correlated radical pair state. A consequence of the spin selection rules for spin-correlated radical pair states discussed in section 2.2.2 is that the photo-generated singlet exciton must produce a SCR_P state with mixed singlet and triplet character. Due to the mixed spin character of the SCR_P state and the low ΔE_{ST} of 4CzIPN, geminate recombination of the SCR_P state to reproduce a molecular exciton can populate either S_1 or T_1 and hence be a mechanism of intersystem crossing.

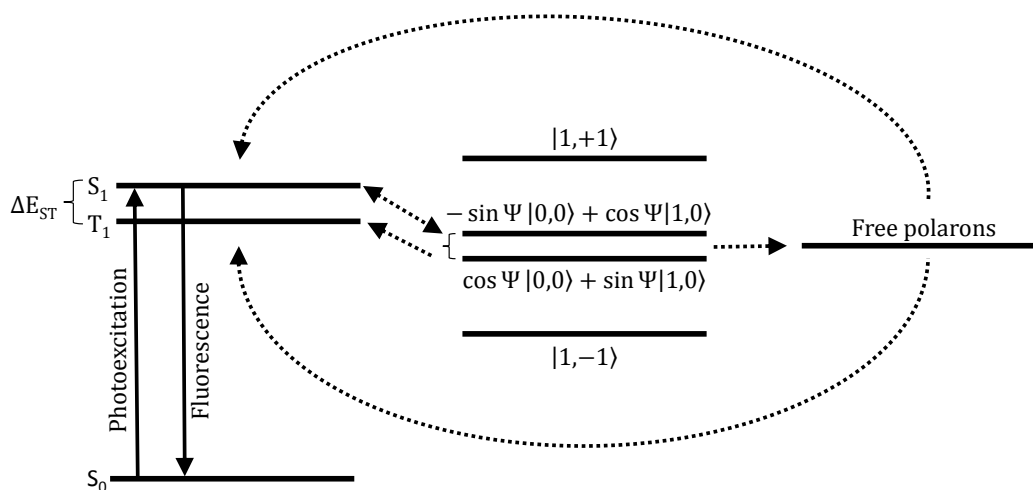


Fig. 5.12 A proposed kinetic model for intersystem crossing in solid films of CBP:4CzIPN in a magnetic field. The ordinate axis has units of energy however relevant energy levels of radical pair states and free polarons have not been measured and are shown in arbitrary positions for illustration. The abscissa has no physical meaning

Back-transfer from an SCRPs state to a molecular exciton is in kinetic competition with charge separation to produce free polarons. In high concentration films of 50 wt.% and host-free 4CzIPN it is apparent that the triplet signal is much weaker than the free polaron signal even at late times. This is in contrast to the low concentration 1 wt.% and 5 wt.% where the triplet signal is dominant at $t > 2000$ ns. As the 4CzIPN concentration increases in films it is likely that delocalisation across larger domains allows a faster rate of charge separation. The back-transfer to molecular excitons is therefore outcompeted and the SCRPs-mediated triplet signal is not observed in host-free 4CzIPN films. Further an increased population of free polarons from efficient charge separation would increase the rate of non-radiative exciton quenching processes such as triplet-polaron annihilation. The kinetic competition between SCRPs-mediated intersystem crossing and charge separation could therefore provide a mechanistic explanation for the observed concentration dependent luminescence quenching in 4CzIPN. Additionally the absence of SCRPs-mediated triplet signal from the host-free film has allowed the emergence of a weak triplet signal to be visualised at times greater than 2000 ns. Interestingly this triplet signal displays a AAEEAEE spectral pattern, which is distinct from those observed in either the frozen solution or low-concentration film data and is characteristic of a triplet exciton formed through spin-orbit coupling with triplet sub-state populations $P_Z > P_Y > P_X$. This represents a shift in population from the P_X to P_Z when moving from the isolated molecule condition in dilute solution to the aggregated condition in

host-free thin films and is likely to reflect a change in the vibrational environment between these two extreme cases.

In an operating OLED device, excitons are generated through the non-geminate recombination of electrically-injected electrons and holes with uncorrelated spin. This produces an exciton population of 25% singlets and 75% triplets, which will include all three triplet sub-states. The intersystem crossing process most relevant to the operation of high-performance OLEDs is therefore the overall endothermic reverse transition from T_1 to S_1 from all three triplet sub-states. However, in the $B_0 = 0$ condition that devices typically operate under, the energetic splitting of the four SCRP states will be minimal and vibronic coupling can overcome the energetic differences between SCRP eigenstates. Consequently it may be possible to infer that the mechanism of intersystem crossing seen here from photogenerated singlet states is applicable to the reverse intersystem crossing mechanism undertaken by electrically-generated triplets in OLED devices. It has been reported that the rates of forward and reverse intersystem crossing are correlated in 4CzIPN and a number of variants. This correlation could further support the suggestion that intersystem crossing following photoexcitation in an ESR experiment follows the same mechanism as reverse intersystem crossing following electrical injection in an OLED device.[115]

5.6 Conclusion

It has been verified that the triplet ESR pattern found from isolated 4CzIPN molecules in dilute solution is consistent with the prevalent spin-vibronic model of intersystem crossing in TADF emitter materials. However, it has been found that in aggregated states an intermolecular charge transfer process becomes important. In low-concentration films relevant to high-performance devices the dominant mechanism of triplet formation from photogenerated singlets is through an intermediate SCRP state. This SCRP-mediated mechanism is in surprising contrast to equivalent measurements in isolated molecules and the prevalent spin-vibronic model of intersystem crossing in TADF materials. This result could have large consequences for rational molecular design for TADF emitters; it may be less important than has been claimed to engineer the relative energies of states such that local triplet excitons are energetically resonant with the CT state. The results presented in this chapter suggest that greater emphasis should be placed on achieving favourable intermolecular charge transfer such that an SCRP state is accessible but that back transfer to the molecular exciton can outcompete charge separation.

Chapter 6

Triplet Excitons in Organic Photovoltaics

6.1 Introduction

In an OPV device, excited states are formed by photoexcitation leading to an initial population of singlet excitons. Triplets can be formed through exothermic intersystem crossing or bimolecular recombination of free charges. Attempts to specifically use triplets to create free charges which can be collected at the electrodes have a long history. During the 1990s, polymers containing heavy metals such as platinum or palladium were used to create a population of triplets in an OPV device through the strong spin-orbit coupling of the metal atom.[116] The longer lifetime of triplet excitons in comparison to singlets favoured charge separation, however this was cancelled by a large ΔE_{ST} value of 0.8 eV which contributed to a higher binding energy for the triplets and caused suppression of charge separation. There was therefore not found to be an overall advantage over contemporary cells which generated free charges primarily from singlet excitons.[117]

Since the development of heterojunction structures for charge separation in OPV the transport properties of excitons have become more important. Charge separation can only happen with maximum efficiency if excitons can reach an interface before recombining. The advent of bulk heterojunction active layer morphologies facilitated efficient charge separation by shortening the average distance between a photon absorption site and an interface at which charge separation could occur. However, morphological optimisation can lead to compromise between small domain sizes for efficient charge separation and the continuity of percolation pathways for charge collection. The longer lifetimes of triplets in comparison to singlets is advantageous as it may allow larger diffusion lengths and hence increased charge separation and collection efficiency. It should however be noted that long-range Förster transfer between an excited molecule and a molecule in the ground state requires that the ground and excited states have the same spin multiplicity. In the case of a triplet excited state,

Förster transfer to an unexcited molecule in the singlet ground state is therefore forbidden and triplets may only diffuse through short-range Dexter transfer. The consequence of this is that despite their longer lifetimes it does not always follow that triplet excitons will have greater diffusion lengths than singlets. Nevertheless some materials, such as the OLED host material CBP, can display very large triplet diffusion lengths of up to 140 nm, albeit at low excitation density; at higher excitation density where triplet-triplet annihilation becomes more significant the diffusion length can fall by a factor of 10.[118, 119] Phosphorescent materials, which give a high yield of triplets due to fast intersystem crossing, have previously been used as triplet sensitisers in OPV devices. However, large ΔE_{ST} values result in energy loss during intersystem crossing and subsequent power conversion efficiency gains are often modest.[120–122]

A further method of utilising triplets in photovoltaic devices is through a triplet-triplet annihilation upconversion process.[123] Semiconductor materials cannot absorb incident light at photon energies below the absorption edge. Lower energy photons will therefore not contribute to the electrical power output of the device; these spectral losses contribute to fundamental efficiency limits to both organic and inorganic photovoltaics.[44] While often an unwanted source of non-radiative recombination in both OLED and OPV devices, triplet-triplet annihilation can also be used to convert two incident low energy photons into a single higher energy photon which may be absorbed by an underlying photovoltaic cell.[124, 125] This upconversion method can be used to widen the spectral response of a photovoltaic system and raise the overall efficiency. However, at incident light intensities relevant to solar photovoltaics it has been found that the triplet-triplet annihilation upconversion effect is too small to generate measurable power conversion efficiency enhancement.[126]

In spite of these notable efforts to utilise triplet excitons in photovoltaics, triplet states are often considered a source of efficiency loss.[46, 47] As discussed in section 2.5.1 an investigation into the use of low ΔE_{ST} materials in OPV devices is motivated by the possibility of avoiding low-lying molecular triplet states which are exothermically accessible from intermolecular CT states. Such low-lying triplet states, a result of the large ΔE_{ST} in typical organic semiconductors, are a source of non-radiative recombination and hence contribute to V_{OC} loss in OPV devices. To ensure that T_1 remains higher in energy than the CT state, ΔE_{ST} must be less than the energy difference between molecular singlet excitons and the CT state. This driving energy can vary between different OPV systems but to facilitate efficient charge separation is often greater than 0.2 eV.[127] An ideal material will therefore have a ΔE_{ST} less than 0.2 eV in addition to good optical absorption and good charge mobility to aid the extraction of photocurrent. In this chapter, a screening study is reported to evaluate

the suitability of low ΔE_{ST} materials in OPV blends. The materials used in this chapter are shown in figure 6.1.

9-H-Thioxanthen-9-one-10,10-dioxide triphenylamine (TXO-TPA) is a TADF emitter comprising a thioxanthone dioxide electron-accepting moiety and a triphenylamine electron-donating moiety. TXO-TPA has a reported ΔE_{ST} of 52 meV and has previously been used to make high-efficiency TADF OLEDs.[128] Despite relatively poor optical absorption it was used in a study to test whether charge separation could be achieved in a bulk heterojunction blend with low energetic offset, low rates of non-radiative recombination and hence low V_{OC} loss in an OPV device.

An investigation was also conducted into the use of near-infrared emitting material 3,4-bis(4-(diphenylamino) phenyl) acenaphtho[1,2-b] pyrazine-8,9-dicarbonitrile (APDC-DTPA). APDC-DTPA is a TADF emitting material with $\Delta E_{ST} = 0.14$ eV and has been used to fabricate NIR OLEDs with $\eta_{EQE} = 10\%$. In line with its near-infrared emission APDC-DTPA films have an absorption profile covering much of the visible light spectrum as is required for efficient photovoltaic applications.

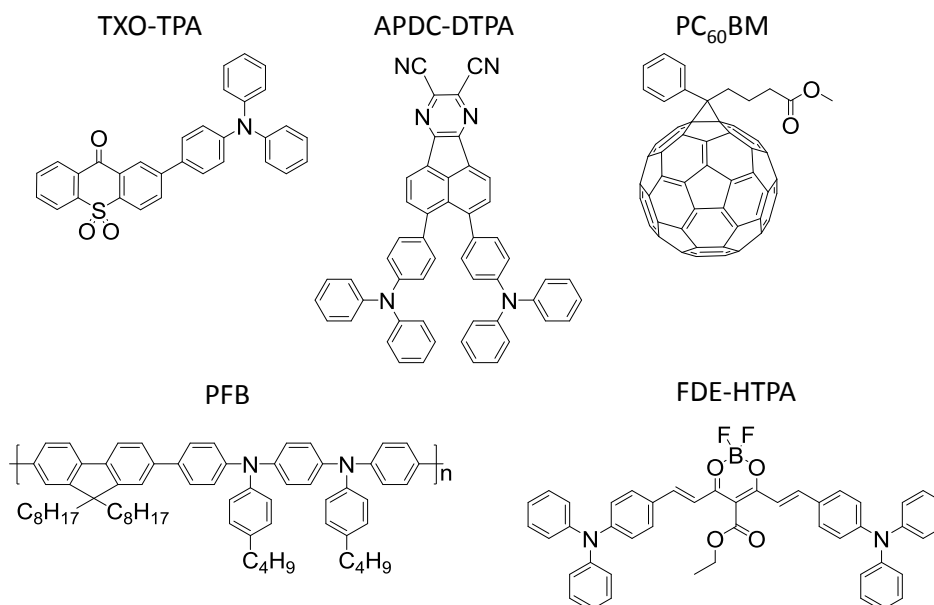


Fig. 6.1 Chemical structures of materials used in OPV device blends

6.2 Collaborator contributions

Transient absorption spectroscopy data in this chapter were measured by Alexander Gillett. FDE-HTPA was synthesised by Dandan Yao

6.3 Experimental methods

OPV devices were fabricated in a structure of ITO/PEDOT:PSS/Active Layer/Ca/Al where PEDOT:PSS is poly(3,4-ethylenedioxythiophene) polystyrene sulfonate. PEDOT:PSS is a conducting polymer mixture which improves hole extraction at the anode due to its workfunction of $\gtrsim 5.1$ eV.[7] ITO substrates were prepared by sequential cleaning in an ultrasonic bath of a non-ionic detergent solution, deionised water, acetone and propan-2-ol. They were subsequently subjected to an O₂ plasma treatment for 10 minutes, which simultaneously helps to remove residual organic contaminants and lowers the work function of the ITO. An aqueous suspension of PEDOT:PSS was filtered through a hydrophilic polypropylene filter (pore size 0.45 μm) and then spin-coated onto the ITO substrates in air at 5000 rpm for 30 s. The PEDOT:PSS layers were heated to 130°C for 20 minutes to remove residual water from the layer. The PEDOT:PSS coated substrates were then transferred to a nitrogen-filled glovebox with oxygen concentration less than 0.1 ppm and atmospheric moisture concentration less than 0.5 ppm where the active layers were deposited by spin-coating from anhydrous and oxygen-free solutions. A cathode comprising 10 nm of calcium and 100 nm of aluminium was deposited onto the devices through vacuum thermal evaporation. A shadow mask was used to create 8-pixels on each substrate defined by the 4.5 mm² overlap area between the cathode and the ITO anode.

APDC-DTPA and TXO-TPA were blended with the wide HOMO-LUMO gap polymer poly(9,9-dioctylfluorene-co-bis(N,N'-(4-butylphenyl))bis(N,N'-phenyl-1,4-phenylene)diamine) (PFB). PFB has a reported HOMO at -5.1 eV which can allow charge separation by hole transfer from the low- ΔE_{ST} materials to the PFB with low energy loss. Additionally PFB has a good hole mobility with reported values of between 10^{-4} - 10^{-3} cm²V⁻¹s⁻¹, which should allow efficient transport of free holes to the anode.[129] In these blends the low- ΔE_{ST} materials are expected to act as electron acceptors or, perhaps more instructively, as hole donors. The wide HOMO-LUMO gap of PFB means that photon absorption in the visible range should be dominated by the low- ΔE_{ST} material. The electroluminescence of PFB peaks at 475 nm, equivalent to an S₁ energy of 2.6 eV.[130] The PFB T₁ energy can then be assumed to be approximately 1.9 eV based on the general rule that $E_{T_1} \approx E_{S_1} - 0.7$ eV for conjugated polymers.[131]. The PFB T₁ energy is therefore greater than the energy difference between

the HOMO of PFB and the LUMO of either APDC-DTPA or TXO-TPA. Hence it is expected that the interfacial CT state will be the lowest energy neutral excited state in the system and that these blends will not suffer from non-radiative losses due to low-lying molecular triplet states.

TXO-TPA and APDC-DTPA were also trialled as electron donors in blends with the commonly used electron acceptor [6,6]-phenyl-C₆₁-butyric acid methyl ester (PC₆₁BM), and in the case of APDC-DTPA with a curcuminoid-type material (*1E,4Z,6E*)-heptatriene, 1,7-*bis*[4-(diphenylamino)phenyl], difluoroboron-3,6- β -diketonate, 5-ethylcarboxylate (FDE-HTPA) which is closely related to materials reported as near-IR OLED emitters and which have been used as electron donors in OPV blends with PC₆₁BM.[132, 133] The PC₆₁BM T_1 energy is 1.5 eV.[134] Given the large HOMO-HOMO offset between either TXO-TPA or APDC-DTPA and PC₆₁BM it is likely that the interfacial CT state energy will therefore be lower in energy than any molecular triplet states, as per the intended design of the system. The T_1 energy of FDE-HTPA has not been assessed but it is assumed to possess a low ΔE_{ST} based on the observation of delayed fluorescence and high-efficiency OLEDs.[133]

A proposed energy level diagram for the materials used in this chapter is shown in figure 6.2. HOMO and LUMO levels for PC₆₁BM, TXO-TPA, PFB and APDC-DTPA have been taken from literature reports.[127, 128, 135, 136] The FDE-HTPA energy levels were found through cyclic voltammetry by Dandan Yao. It should be noted that large discrepancies exist in the quoted energy of the PC₆₁BM LUMO with typical values ranging between approximately -3.7 eV and -4.4 eV.[127, 137–140]. HOMO and LUMO values for PC₆₁BM are usually quoted from cyclic voltammetry measurements; the sources of inconsistency can be due to variation in experimental conditions such as solvent, electrolyte or electrode materials. The values quoted in this thesis have been measured according to a best practice method.[127, 140]

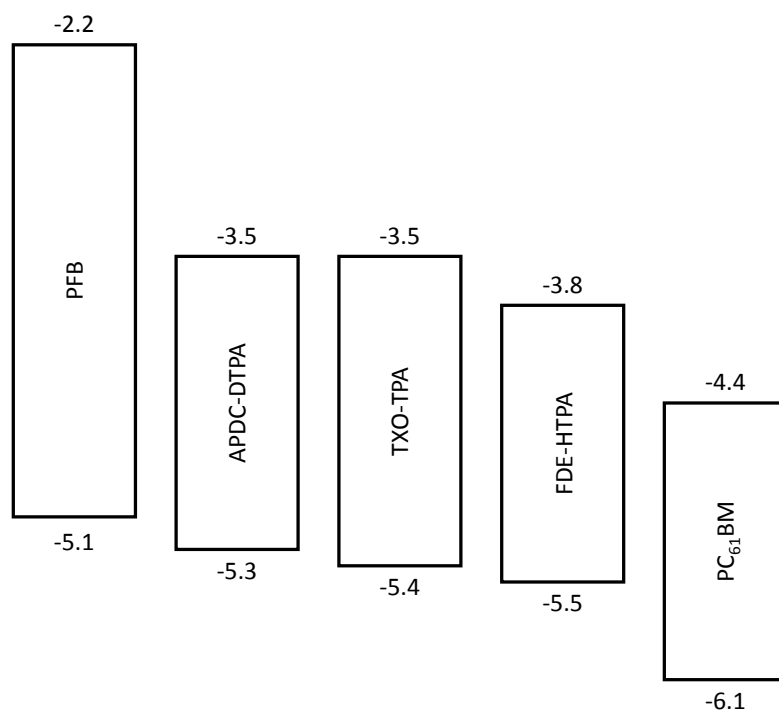


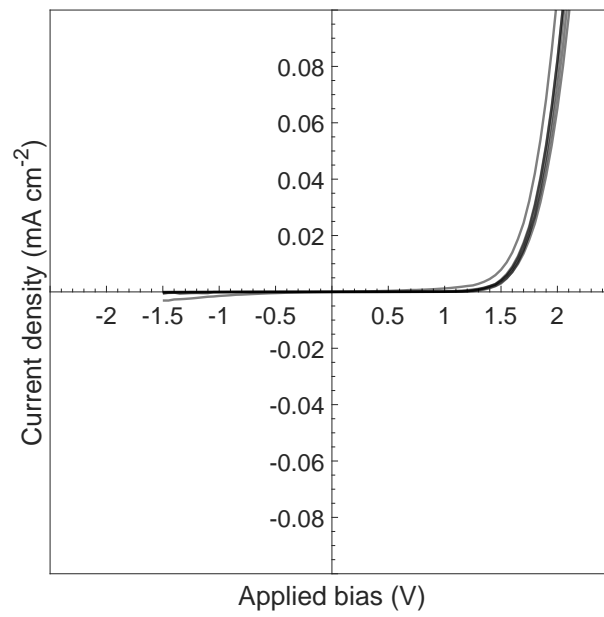
Fig. 6.2 Proposed energy level diagram of materials used in this chapter: PFB, APDC-DTPA, TXO-TPA, FDE-HTPA, PC₆₁BM

6.4 Results

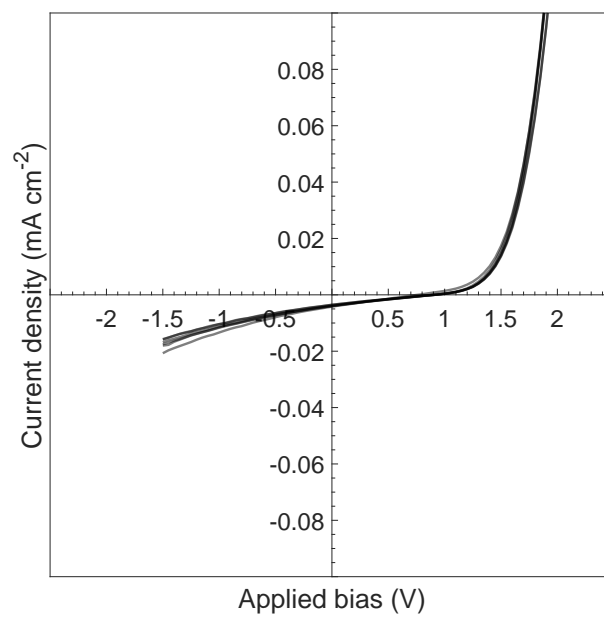
6.4.1 TXO-TPA

The J-V curves shown in figure 6.3b of PFB:TXO-TPA devices measured under solar simulator illumination show an extremely low J_{SC} of $4 \times 10^{-3} \text{ mA cm}^{-2}$. This low photocurrent is due to the low optical absorption shown in figure 6.4 and is consistent with the predicted J_{SC} found from integrating the EQE spectrum at zero applied bias shown in figure 6.5. From comparison of the dark and illuminated J-V curves in figure 6.3 it is clear that the small collected current does constitute a photocurrent. It is also observed that the current increases when the applied bias is reversed, indicating a field-assisted charge extraction effect. This is further illustrated on comparison of the device external quantum efficiency at varying reverse bias shown in figure 6.5 and is taken to imply that there is inefficient collection of generated free charges. Due to the high hole mobility of PFB it is likely that this is a result of poor electron mobility in TXO-TPA which would suppress both J_{SC} and fill factor and hence contribute to the very low measured η_{PCE} of $8 \times 10^{-4}\%$.

Electroluminescence was measured from the PFB:TXO-TPA blend as shown in figure 6.6. The applied bias was 12 V and the current density was 1100 mA cm^{-2} . A broad peak centred at 700 nm was observed. This is significantly red-shifted and broadened in comparison to the known electroluminescence spectra of either TXO-TPA or PFB so is interpreted as emission from the interfacial CT state formed by an electron in the TXO-TPA LUMO and a hole in the PFB HOMO. This is taken as indication that charge separation in the blend occurs through an intermediate CT state with $E_{CT} = 1.75 \text{ eV}$, although the absorption and η_{EQE} spectra shown in figures 6.4 and 6.5 suggest that this may be formed primarily from photoexcitation of PFB, rather than TXO-TPA as intended. The open-circuit voltage of $V_{OC} = 0.90 \text{ V}$ therefore reflects a voltage loss of 0.85 V in comparison to the energy of the CT state. Contrary to the experimental aim this V_{OC} loss is comparatively large and is attributed to recombination due to poor charge extraction.



(a) Dark J-V characteristic



(b) Light J-V characteristic

Fig. 6.3 J-V characteristics a) in the dark and b) under 100 mW cm⁻² illumination from an AM1.5G solar simulator of PFB:TXO-TPA bulk heterojunction OPV cells

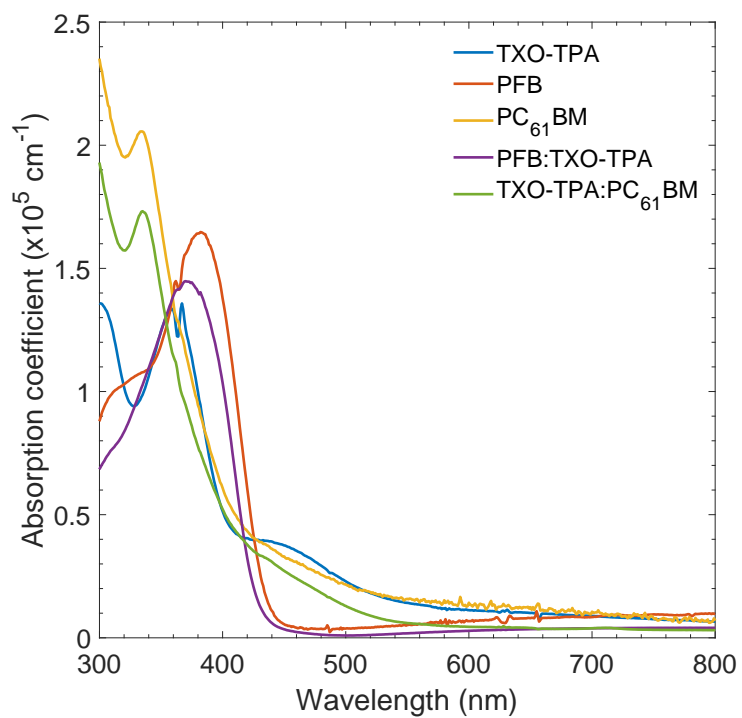


Fig. 6.4 Absorption spectra of TXO-TPA, PFB, PC₆₁BM and blends of PFB:TXO-TPA and TXO-TPA:PC₆₁BM with 20 wt.% of TXO-TPA.

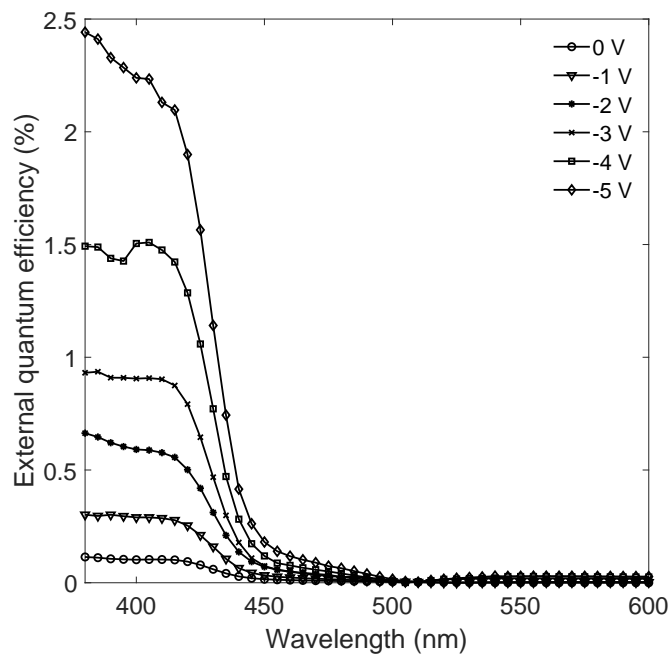


Fig. 6.5 External quantum efficiency as a function of excitation wavelength for PFB:TXO-TPA at varying reverse bias

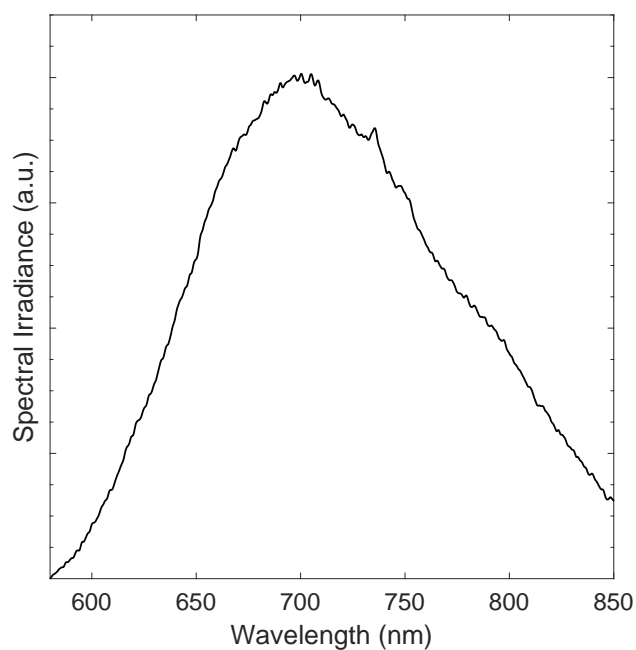
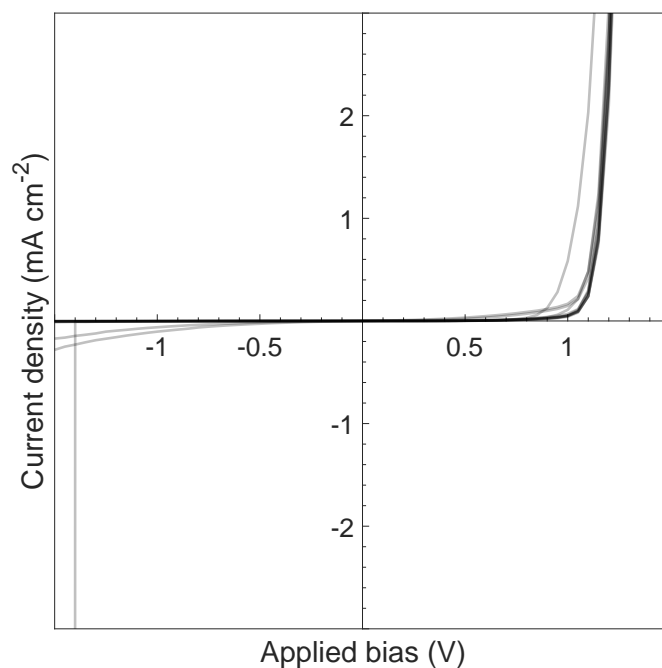
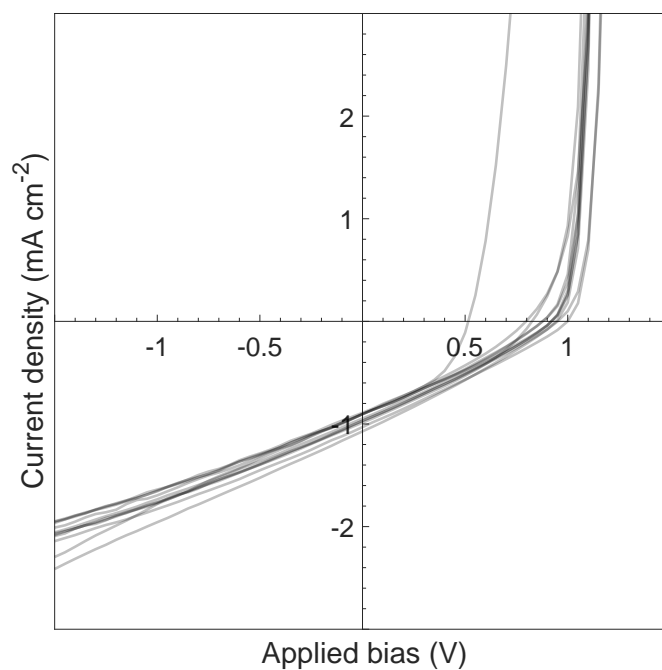


Fig. 6.6 Electroluminescence spectrum of a PFB:TXO-TPA device

TXO-TPA was also used as an electron donor when blended with PC₆₁BM as an electron acceptor. Light and dark J-V curves are shown in figure 6.7 for OPV devices made from a 1:4 by weight blend of TXO-TPA:PC₆₁BM. The film thickness was 100 nm as measured by ellipsometry of a film prepared on a silicon wafer under the same conditions. The device generates a low photocurrent of $J_{SC} = 0.96 \text{ mA cm}^{-2}$. However, similarly to the PFB blend, field-assisted charge extraction is evident at reverse bias in the J-V curve and also in the variation of η_{EQE} with reverse bias as shown in figure 6.8.



(a) Dark J-V characteristic



(b) Light J-V characteristic

Fig. 6.7 J-V characteristics a) in the dark and b) under 100 mW cm⁻² illumination from an AM1.5G solar simulator of TXO-TPA:PC₆₁BM bulk heterojunction OPV cells

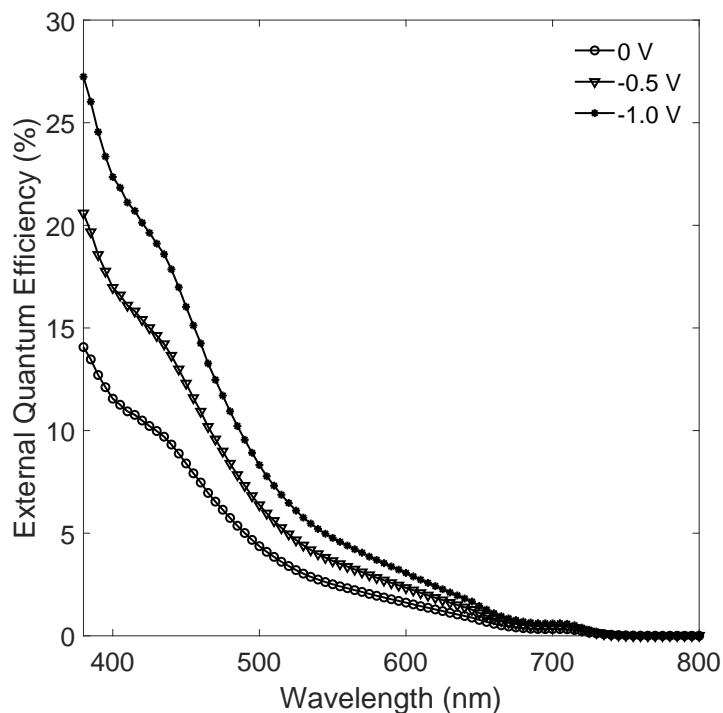


Fig. 6.8 External quantum efficiency as a function of excitation wavelength for TXO-TPA:PC₆₁BM at varying reverse bias

PC₆₁BM is a benchmark electron accepting and transporting material so it is likely that electron extraction is efficient but that hole transport through the TXO-TPA is poor. The electroluminescence spectrum of the TXO-TPA:PC₆₁BM device, measured with an applied bias of 7 V and current density of 7500 mA cm⁻², is shown in figure 6.9 with a peak wavelength of 745 nm equivalent to a photon energy of 1.7 eV. The observed electroluminescence spectrum is reminiscent of that which would be expected from a singlet state of PC₆₁BM.[141] Based on the proposed energy levels shown in figure 6.2 it is likely that the interfacial CT state formed between the HOMO of TXO-TPA and LUMO of PC₆₁BM is lower in energy than the PC₆₁BM S₁ state and may emit at wavelengths greater than 1000 nm which is outside of the sensitive range of the silicon CCD detector. However the strong electroluminescence signal from PC₆₁BM suggests that there is incomplete charge transfer from excited PC₆₁BM molecules to form the interfacial CT state. This could suggest that TXO-TPA is not contributing to the electronic properties of the device blend and that the observed photocurrent could be the result of charge separation and transport solely through domains of PC₆₁BM.

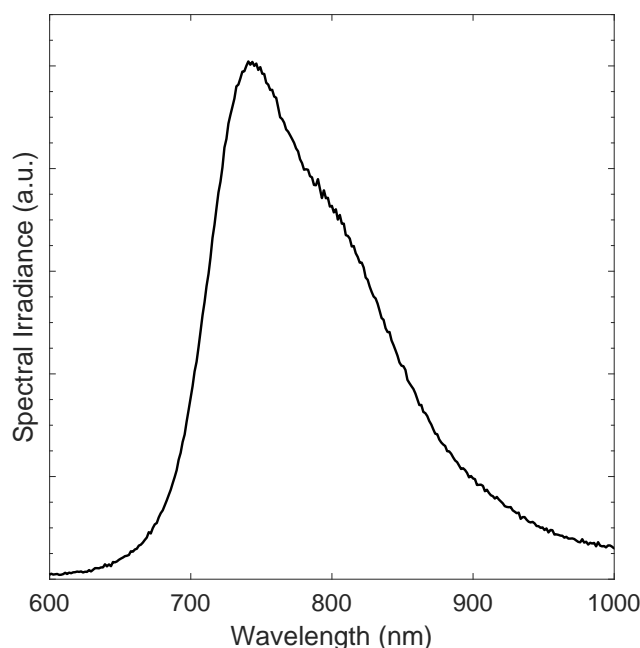
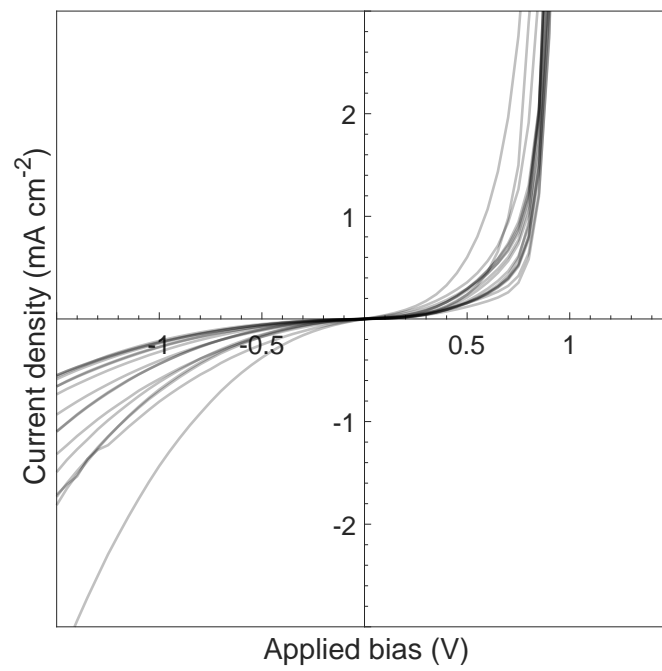


Fig. 6.9 Electroluminescence spectrum of a TXO-TPA:PC₆₁BM device

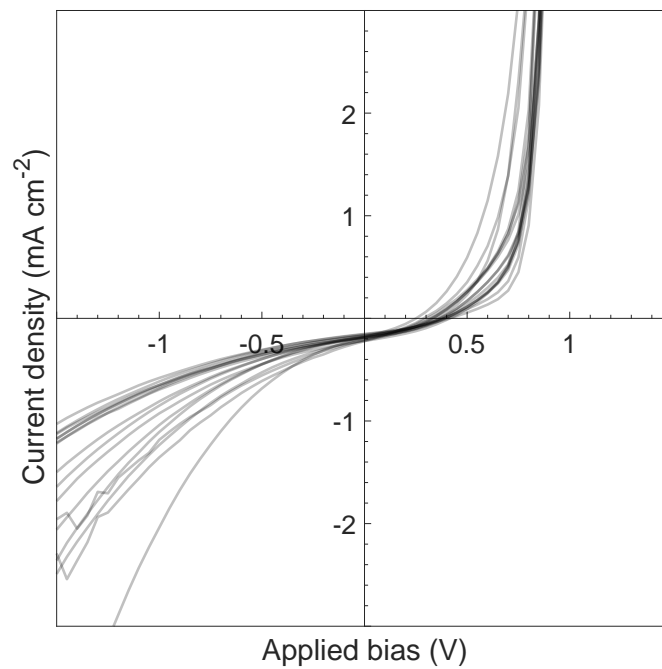
To investigate this, devices were prepared using an active layer of pure PC₆₁BM and with varying concentrations by weight of TXO-TPA. It is evident from the poor device performance of a PC₆₁BM-only device shown in figure 6.10 and the η_{EQE} variation with concentration of TXO-TPA shown in figure 6.11 that charge generation and collection is improved by the presence of TXO-TPA with an optimum concentration within the range 10-50 wt.% of TXO-TPA.

Transient absorption spectroscopy was used to confirm that the positive effect of the presence of TXO-TPA is due to electronic interaction between the donor and acceptor and not, for example, due to morphological changes in the film. Figure 6.12 shows transient absorption data for pure TXO-TPA, pure PC₆₁BM and TXO-TPA:PC₆₁BM films with 20 wt.% TXO-TPA. The TXO-TPA data is dominated by a broad photo-induced absorption feature centred at 780 nm which grows to a maximum at 10 ps while a smaller photo-induced absorption at 870 nm decays. Pure PC₆₁BM shows a broad photo-induced absorption centred at approximately 810 nm and a second, narrower, feature at 540 nm. Both features have a similar magnitude and decay on the same timescale. In the pure films it can be considered that the initial excited state population following the excitation pulse will be S_1 excitons. The transient absorption spectra of the pure films therefore shows energetic transitions from the S_1 state for each material. By comparing the blended film with these pure films it can be inferred whether new states are being formed in the blend, which could indicate the presence

of an interfacial CT state or an increased population of free charges. Figure 6.12c shows that the transient absorption spectrum in the blend film is dominated by a photoinduced absorption feature at 550 nm. This feature does not appear in the TXO-TPA sample and is seen to be slightly shifted and much more prominent than the similar feature in the pure PC₆₁BM. The PC₆₁BM anion is known to have a broad absorption with a sharp peak at around 1000 nm so cannot account for this feature and is outside of the experimental measurement range.[142, 143] Interfacial CT state absorption is usually weak due to the small overlap between electron and hole wavefunctions located on different molecules, so is unlikely to contribute to this strong feature. By a process of elimination it is therefore conjectured that the enhanced photoinduced absorption at 550 nm in the blend film is due to the presence of TXO-TPA⁺ cations. While further investigations would be required to increase the level of confidence, this may be taken as evidence of charge separation in the TXO-TPA:PC₆₁BM blend. However the electroluminescence spectrum suggests that in working devices the rate of charge transfer may be out-competed by recombination of the PC₆₁BM S₁ state.



(a) Dark J-V characteristic



(b) Light J-V characteristic

Fig. 6.10 J-V characteristics a) in the dark and b) under 100 mW cm^{-2} illumination from an AM1.5G solar simulator of pure PC₆₁BM OPV cells

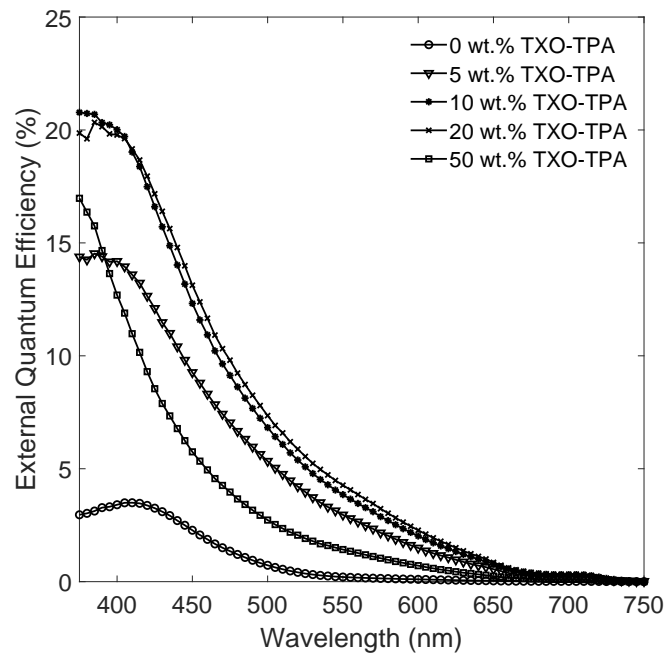
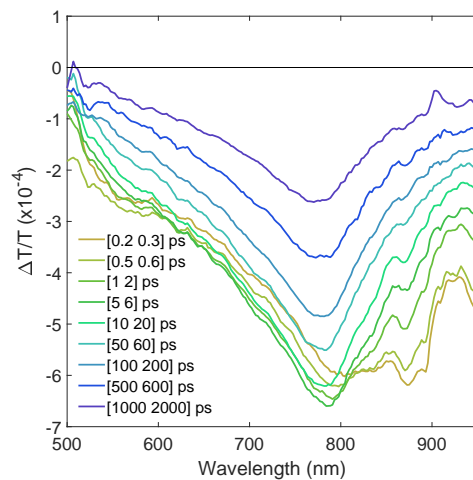
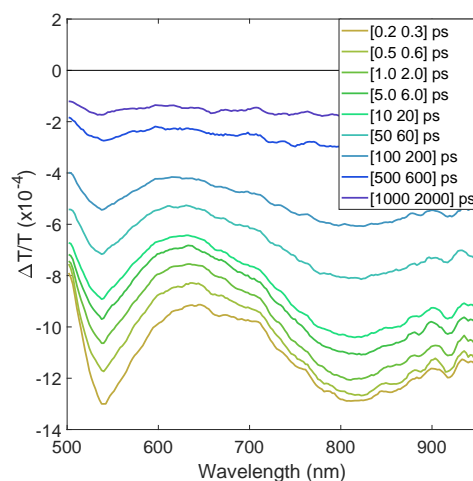


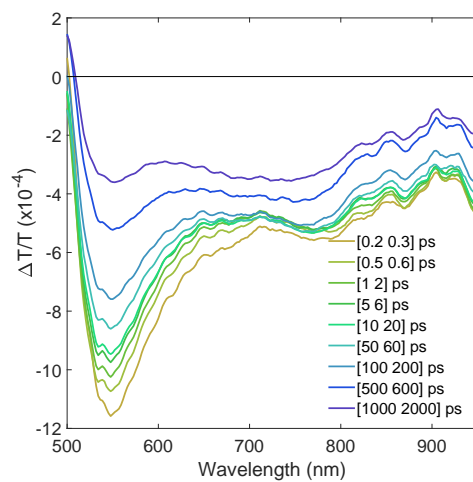
Fig. 6.11 External quantum efficiency as a function of excitation wavelength for TXO-TPA:PC₆₁BM bulk heterojunction OPV cells with varying composition ratios



(a) Pure TXO-TPA. $\lambda_{Ex} = 450$ nm, $H_{Ex} = 95.9 \mu\text{J cm}^{-2}$



(b) Pure PC₆₁BM. $\lambda_{Ex} = 430$ nm, $H_{Ex} = 39.6 \mu\text{J cm}^{-2}$



(c) TXO-TPA:PC₆₁BM. $\lambda_{Ex} = 450$ nm, $H_{Ex} = 44.4 \mu\text{J cm}^{-2}$

Fig. 6.12 Transient absorption spectroscopy of a) pure TXO-TPA b) pure PC₆₁BM and c) TXO-TPA:PC₆₀BM films

The champion TXO-TPA:PC₆₁BM device in figure 6.7b has $V_{OC} = 1.0$ V and the median is $V_{OC} = 0.92$ V. This represents a total V_{OC} loss of 0.7 V when compared to the onset of optical absorption of the blend at 740 nm. Despite the blend design being such as to avoid a loss pathway through low-lying triplet states this V_{OC} loss is similar to other OPV devices. Additionally, given the poor η_{PCE} performance these devices fall a long way short of benchmark OPV cells. Poor optical absorption of the TXO-TPA, incomplete charge transfer and potentially poor charge transport in TXO-TPA have been cited as factors limiting the device efficiency and contributing to increased V_{OC} loss.

6.4.2 APDC-DTPA

APDC-DTPA is a near-infrared emitting material with a wide absorption band between 500-600 nm, so is able to utilise a greater part of the solar spectrum as shown in the absorption spectra in figure 6.13. Figure 6.14 shows J-V curves for devices fabricated from a bulk heterojunction blend of PFB:APDC-DTPA with 75 wt.% of APDC-DTPA. It is apparent that there is significant charge leakage through the device at reverse bias, even in the dark. This could suggest that the optimum thickness of the active layer is greater than that achieved in the fabricated devices. The film thickness deposited under the same conditions (spin-coating at 1000 rpm from a 10 mg mL⁻¹ chlorobenzene solution) onto a silicon substrate was found to be 90 nm using spectral ellipsometry, however it is possible that spin-coating on a surface of PEDOT:PSS may have created a thinner layer than expected. Similarly to devices incorporating TXO-TPA, a field-assisted charge extraction effect is observed suggesting inefficient charge transport through the APDC-DTPA. The consequent recombination in the device is a limitation on the J_{SC} , fill factor and V_{OC} . The η_{PCE} is therefore restricted to a maximum of 0.26 % and a median of 0.17 %.

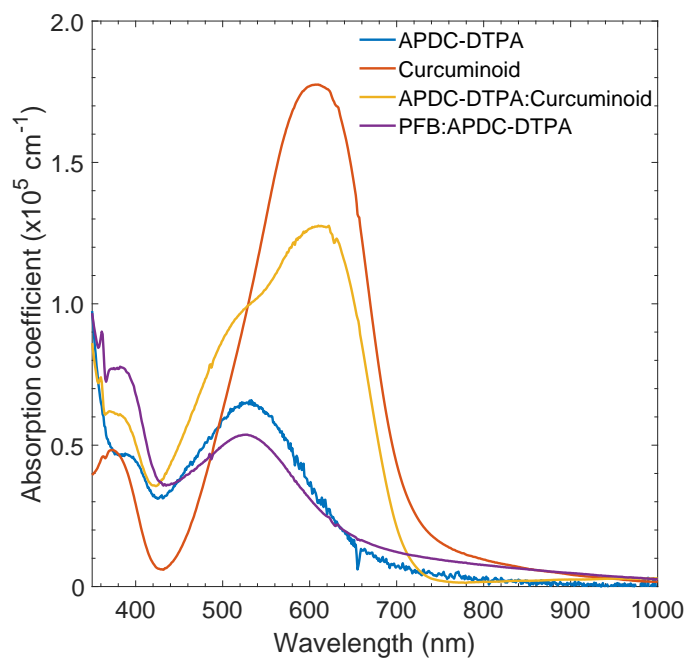
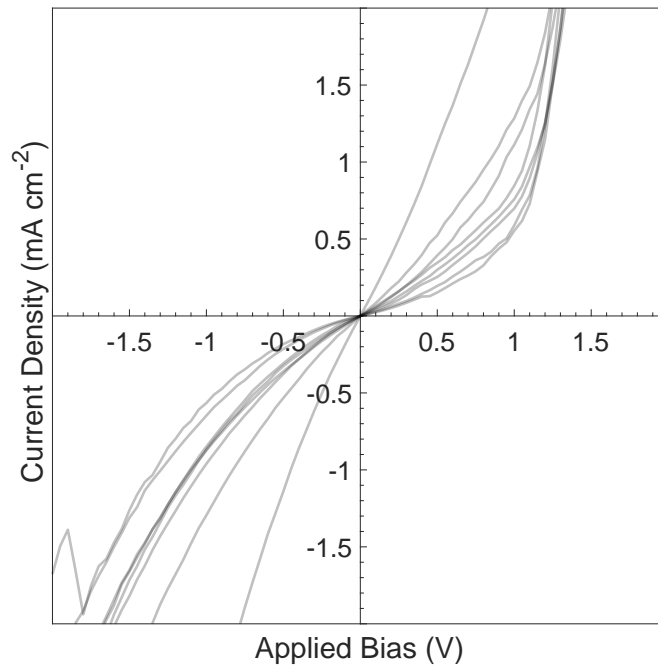
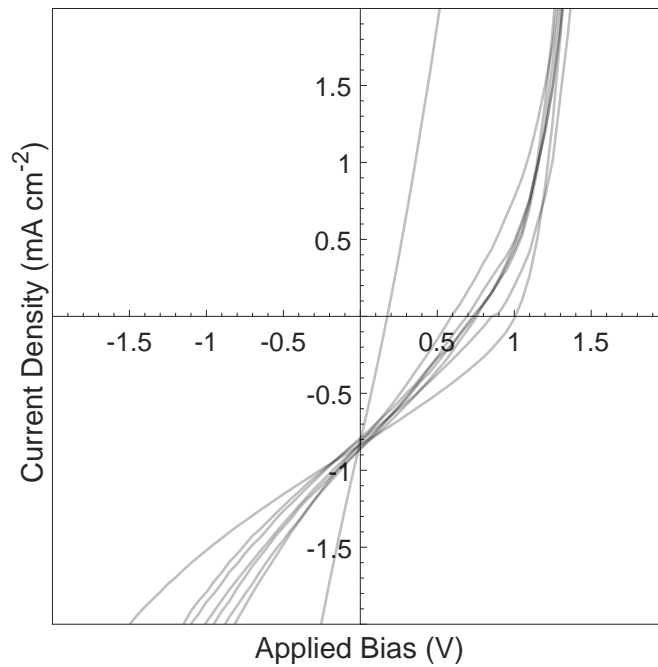


Fig. 6.13 Absorption spectra of APDC-DTPA, FDE-HTPA and blends of APDC-DTPA: FDE-HTPA (1:1 by weight) and PFB:APDC-DTPA (1:3 by weight)



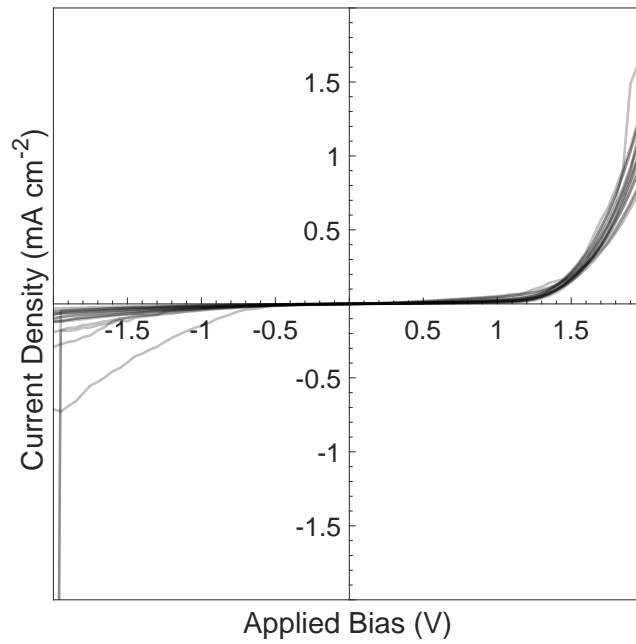
(a) Dark J-V characteristic



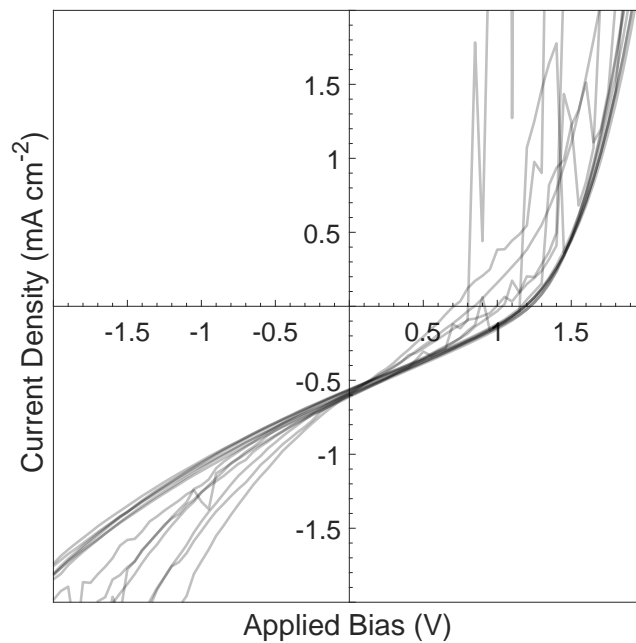
(b) Light J-V characteristic

Fig. 6.14 J-V characteristics a) in the dark and b) under 100 mW cm^{-2} illumination from an AM1.5G solar simulator of PFB:APDC-DTPA (1:3 by weight) OPV cells

It was not possible to use APDC-DTPA as an electron acceptor in a solution-processed bulk heterojunction blend with PC₆₁BM due to the poor quality of films which could be produced by spin-coating. However an experimental device incorporating FDE-HTPA as electron acceptor was fabricated. As shown in figure 6.13 FDE-HTPA has a strong absorption band centred at 610 nm and closely related molecules have previously been successfully used as electron donors in OPV devices. As shown in figure 6.15, APDC-DTPA:FDE-HTPA devices also showed poor charge extraction and a low η_{PCE} . The V_{OC} of 1.2 V is notably high and compares well to the onset of optical absorption at 775 nm, however losses in the device are evident through the observed field-assisted charge extraction and low fill factor of 0.29. Quantification of the V_{OC} loss is therefore of limited value.



(a) Dark J-V characteristic



(b) Light J-V characteristic

Fig. 6.15 J-V characteristics a) in the dark and b) under 100 mW cm^{-2} illumination from an AM1.5G solar simulator of APDC-DTPA:FDE-HTPA (1:1 by weight) OPV cells

6.5 Discussion

OPV devices fabricated with the low ΔE_{ST} materials TXO-TPA and APDC-DTPA have characteristically shown poor charge extraction, which can potentially be attributed to poor charge mobility in these materials. This poor charge extraction has frustrated attempts to fabricate OPV devices with high fill factor, which can be used as a non-specific measure of loss mechanisms within the device, and has limited the observed J_{SC} , V_{OC} and η_{PCE} . Consequently any favourable properties conferred on these devices by the lack of a low-lying T_1 state are difficult to determine. The performance of APDC-DTPA and particularly TXO-TPA devices are also severely limited by poor absorption over much of the visible spectrum. This is seen as a more fundamental limitation as the separation of HOMO and LUMO wavefunctions which weakens the exchange interaction and allows a small ΔE_{ST} also gives rise to a small cross-section for photon absorption.

Contemporaneously with this work large advances have been made in OPV efficiency with reports of single-junction devices with $\eta_{PCE} > 13\%$.^[34, 35] These rapid advances have been made possible with the introduction of non-fullerene acceptors which have enabled increases in photocurrent as a result of good complementary absorption while maintaining efficient charge separation and transport properties. The use of non-fullerene acceptors also represents an additional degree of freedom in the design of donor-acceptor blends and means that the energy levels of acceptor materials can be custom engineered to match donor materials with favourable absorption, transport and recombination properties. In some instances, efficient non-fullerene acceptor based devices have been fabricated with little or no offset of frontier orbitals between the donor and acceptor material.^[144, 145] These devices break with the previous experience of fullerene-based devices where some frontier orbital offset, and hence V_{OC} loss, is required to provide a so-called driving energy to promote efficient charge separation.^[38] Non-fullerene acceptor based devices can therefore display reduced V_{OC} loss on formation of the interfacial CT state while maintaining high J_{SC} .

A detailed photophysical model of charge separation and recombination dynamics in non-fullerene acceptor OPV blends has yet to be produced.^[146] However in some low offset blends it has been found that charge separation occurs on a longer timescale to conventional polymer:fullerene blends (approximately 15-30 ps compared with less than 1 ps) but that the charge separation efficiency remains high due to low non-radiative recombination rates.^[147] The consequent low V_{OC} losses displayed by these systems suggest that molecular triplet levels are not being accessed from the interfacial CT states or are not acting as a significant loss pathway in spite of a lack of consideration of ΔE_{ST} in these systems. This can be rationalised by observations from fullerene-based systems that delocalisation of CT states, which can be promoted by order in the donor and acceptor domains in a blend, can

both limit the back transfer of CT states to molecular triplets and enable efficient charge separation.[41, 46]

6.6 Conclusion

It is apparent that the use of low ΔE_{ST} materials in OPV devices is limited by intrinsically weak optical absorption. Additionally, fulfilling the molecular design requirements for low ΔE_{ST} limits the degrees of freedom available to achieve other favourable properties such as good transport. Recently large advances have been made in improving the V_{OC} and η_{PCE} of OPV devices through the use of non-fullerene acceptors which do not seem to suffer significant non-radiative losses through low-lying triplet states, which is possibly aided by CT state delocalisation. It is concluded that the use of non-fullerene acceptors is a more promising avenue for low V_{OC} -loss and high η_{PCE} OPV research.

Chapter 7

Conclusions

This thesis presented a number of investigations into the role and management of triplets in organic optoelectronic devices. A number of key findings are summarised here with discussion into the future direction of work in the field.

7.1 Carbene-metal-amide organic light-emitting diodes

The first demonstration of vacuum-processed CMA OLEDs was made. High values of η_{eqe} were achieved with a maximum of 26.9% in a green-emitting device, demonstrating efficient triplet utilisation. It was discovered that CMA emitters can be resistant to concentration-dependent luminescence quenching which can affect other OLED materials. Consequently it was possible to achieve $\eta_{eqe} = 23.1\%$ in a host-free emissive layer structure, which is believed to be a record. If fully explored, this property has the potential to facilitate simplified OLED manufacture and consequent reduction in cost. It is also noted that increased emitter concentration could reduce the molecular density of excited states during OLED operation. A reduced excited state density could have a consequent reduction in annihilation processes and lead to advantages in efficiency roll-off and device lifetime.

The ability to control emission colour of CMA materials through manipulation of host environment was discovered. This was used to tune the emission of the green material Au-Cz into the sky-blue while maintaining high efficiency and sub-microsecond emission lifetime. A longstanding challenge in OLED research has been to achieve high-efficiency and stable blue-emitting devices. Through the use of molecular design and a polar host environment to raise the CT energy, high-efficiency blue devices were achieved with maximum $\eta_{eqe} = 18.9\%$ at peak wavelength of 460 nm and CIE co-ordinates (0.17, 0.20). Further molecular side group substitution can be used to achieve deep-blue electroluminescence at CIE (0.16, 0.05) but at the expense of device stability owing to increased triplet lifetimes. Through this series

of side group substitutions it was shown that the molecular CT energy must be kept below the ligand-centred ^3LE energy for efficient electroluminescence in CMA materials.

The first demonstration of efficient OLED devices based on mononuclear silver complexes was made. While gold and copper-centred materials had previously been investigated, both in the CMA motif and in other organometallic structures, efficient silver-based emitters are much rarer. By showing that silver-centred CMA materials can be used in efficient OLED devices, the design space for CMA materials is further opened giving synthetic chemists a greater degree of freedom to select favourable molecular properties.

These results open many avenues for further research. In terms of molecular design, modification to the carbene structure and side groups has not been explored in this thesis and could provide a further route for structural optimisation of CMAs for efficient emission. No investigations of device stability have been made in this thesis, yet this is one of the big challenges facing all types of organic optoelectronic device, especially blue-emitting OLEDs. CMAs have many properties which may allow them to show good operational stability, but this must be demonstrated experimentally. The resistance of CMAs to concentration-dependent luminescence quenching and consequent ability to be used in high-concentration or host-free emissive layers may allow a reduction in excited state density and hence increased device lifetime. Additionally removing the host material may also remove a source of degradation. The wide range of emission colours demonstrated by varying molecular design could be further extended to produce red emission. For example, the use of stronger electron donating side groups such as methoxy could lower the CT state energy enough to produce efficient red emission. Further, it might be possible to combine CMA materials of varying emission colour to make efficient white OLEDs for large-area lighting applications.

7.2 Intersystem crossing in 4CzIPN

A transient EPR study of solid films of 4CzIPN yielded remarkably different results to those previously found in dilute solution. At a film concentration of 5 wt.% — as used in efficient OLED devices — the dominant mechanism of intersystem crossing was found to be through an intermediate spin-correlated radical pair state. This is in contrast to the prevailing spin-vibronic model of intersystem crossing in TADF devices, which had been used to explain ESR signals from isolated molecules in dilute solution. It was also found that as 4CzIPN concentration increased in films, charge separation outcompeted the back transfer of spin-correlated radical pair states to molecular excitons. This would lead to a larger population of free polarons in a film and possibly cause an increase in polaron-exciton annihilation events. An increased rate of charge separation at higher film concentrations

could therefore be a mechanism for the observed concentration-dependent luminescence quenching in 4CzIPN films and devices.

Further investigation is necessary to determine whether these results can be generalised to other TADF materials. One interesting line of enquiry would be to study other carbazoyl dicyanobenzene derivatives to see whether the mechanism of intersystem crossing varies between structurally similar materials but which display varying device performance. Another possibility would be to study other molecular motifs, for example donor-acceptor-donor structured molecules, or materials incorporating different functional groups.

7.3 Open-circuit voltage loss in organic photovoltaics

An investigation into the use of low ΔE_{ST} materials in OPV blends found poor device performance. A number of causes can be attributed to this, including weak absorption in low ΔE_{ST} materials and low efficiency of charge separation and/or collection as evidenced by a common field-assisted charge extraction property. However rapid advances have been made in the record efficiencies of OPV cells through the optimisation of non-fullerene acceptor molecular design. Research into the mechanisms of charge separation and recombination in non-fullerene acceptor blends seems to be the logical priority for the OPV field. An improved mechanistic understanding of the operation of high-efficiency materials could lead to rational design of new materials.

7.4 Outlook and concluding remarks

Research into organic optoelectronic devices is a fast-moving field. Despite having perhaps become eclipsed by the attention given to perovskite materials in recent years, major breakthroughs have been made using organic materials. The advent of TADF OLED emitters and the revolution brought to OPV by non-fullerene acceptors are exciting developments which are still being explored both mechanistically and in the development of high-efficiency devices. Further advances are required to demonstrate that OPV can be competitive with perovskites, other thin-film technologies and established materials such as silicon. OLEDs are already an established technology used in displays, however investigations into and improvements in stability in blue-emitting devices are needed to enable large-area white lighting applications based on organic semiconductors.

This thesis has shown work contributing to the development of new materials for high-efficiency OLEDs, improved the mechanistic understanding of the excitonic processes in the important molecule 4CzIPN, and explored methods of triplet management in OPV devices.

Decarbonisation of electrical power generation and improved efficiency in lighting are key goals to ensure future human wellbeing. The study of optoelectronics could have an important role to play in achieving these goals, and it is clear that the full potential of organic semiconductors is yet to be reached.

References

- [1] M. Kasha. Characterization of electronic transitions in complex molecules. *Discussions of the Faraday Society*, 9:14–19, 1950.
- [2] M. Knupfer. Exciton binding energies in organic semiconductors. *Applied Physics A: Materials Science and Processing*, 77:623–626, 2003.
- [3] T. Chen, L. Zheng, J. Yuan, Z. An, R. Chen, Y. Tao, H. Li, X. Xie, and W. Huang. Understanding the Control of Singlet-Triplet Splitting for Organic Exciton Manipulating: A Combined Theoretical and Experimental Approach. *Scientific Reports*, 5, 2015.
- [4] A. Köhler and H. Bässler. Triplet states in organic semiconductors. *Materials Science and Engineering: R: Reports*, 66:71–109, 2009.
- [5] A. D. McNaught and A. Wilkinson. *Compendium of Chemical Terminology "Gold Book"*. Blackwell Scientific Publications, Oxford, 2nd edition, 2014.
- [6] C. D. Buckley, D. A. Hunter, P. J. Hore, and K. A. McLauchlan. Electron spin resonance of spin-correlated radical pairs. *Chemical Physics Letters*, 135:307–312, 1987.
- [7] A. Köhler and H. Bässler. *Electronic Processes in Organic Semiconductors*. Wiley-VCH, Weinheim, Germany, first edition, 2015.
- [8] G. Baryshnikov, B. Minaev, and H. Ågren. Theory and Calculation of the Phosphorescence Phenomenon. *Chemical Reviews*, 117:6500–6537, 2017.
- [9] Y. Tao, K. Yuan, T. Chen, P. Xu, H. Li, R. Chen, and C. Zheng. Thermally Activated Delayed Fluorescence Materials Towards the Breakthrough of Organoelectronics. *Advanced Materials*, 26:7931–7958, 2014.
- [10] C. A. Parker and C. G. Hatchard. Triplet-singlet emission in fluid solutions. *Transactions of the Faraday Society*, 57:1894–1904, 1961.
- [11] M. A. El-Sayed. The Triplet State : Its Radiative and Nonradiative Properties. *Accounts of Chemical Research*, 1:8–16, 1968.
- [12] B. T. Lim, S. Okajima, A. K. Chandra, and E. C. Lim. Radiationless transitions in electron donor-acceptor complexes: selection rules for S1-T1 intersystem crossing and efficiency of S1-S0 internal conversion. *Chemical Physics Letters*, 79:22–27, 1981.
- [13] C. M. Marian. Mechanism of the Triplet-to-Singlet Upconversion in the Assistant Dopant ACRXTN. *The Journal of Physical Chemistry C*, 120:3715–3721, 2016.

- [14] M. K. Etherington, J. Gibson, H. F. Higginbotham, T. J. Penfold, and A. P. Monkman. Revealing the spin-vibronic coupling mechanism of thermally activated delayed fluorescence. *Nature Communications*, 7, 2016.
- [15] P. L. Santos, J. S. Ward, P. Data, A. S. Batsanov, M. R. Bryce, F. B. Dias, and A. P. Monkman. Engineering the singlet-triplet energy splitting in a TADF molecule. *Journal of Materials Chemistry C*, 4:3815–3824, 2016.
- [16] J. S. Ward, R. S. Nobuyasu, A. S. Batsanov, P. Data, A. P. Monkman, F. B. Dias, and M. R. Bryce. The interplay of thermally activated delayed fluorescence (TADF) and room temperature organic phosphorescence in sterically-constrained donor-acceptor charge-transfer molecules. *Chemical Communications*, 52:2612–2615, 2016.
- [17] M. Saigo, K. Miyata, S. Tanaka, H. Nakanotani, C. Adachi, and K. Onda. Suppression of Structural Change upon S₁-T₁ Conversion Assists Thermally Activated Delayed Fluorescence Process in Carbazole-Benzonitrile Derivatives. *The Journal of Physical Chemistry Letters*, 10:2475–2480, 2019.
- [18] T. Hosokai, H. Matsuzaki, H. Nakanotani, K. Tokumaru, T. Tsutsui, A. Furube, K. Nasu, H. Nomura, M. Yahiro, and C. Adachi. Evidence and mechanism of efficient thermally activated delayed fluorescence promoted by delocalized excited states. *Science Advances*, 3, 2017.
- [19] B. R. Kaafarani, C. Risko, T. H. El-Assaad, A. O. El-Ballouli, S. R. Marder, and S. Barlow. Mixed-Valence Cations of Di(carbazol-9-yl) Biphenyl, Tetrahydropyrene, and Pyrene Derivatives. *Journal of Physical Chemistry C*, 120:3156–3166, 2016.
- [20] Y. Olivier, B. Yurash, L. Muccioli, G. D’Avino, O. Mikhnenko, J. C. Sancho-García, C. Adachi, T. Q. Nguyen, and D. Beljonne. Nature of the singlet and triplet excitations mediating thermally activated delayed fluorescence. *Physical Review Materials*, 1, 2017.
- [21] E. W. Evans, Y. Olivier, Y. Puttisong, W. K. Myers, T. J. H. Hele, S. M. Menke, T. H. Thomas, D. Credgington, D. Beljonne, R. H. Friend, and N. C. Greenham. Vibrationally Assisted Intersystem Crossing in Benchmark Thermally Activated Delayed Fluorescence Molecules. *The Journal of Physical Chemistry Letters*, 9:4053–4058, 2018.
- [22] S. Lobsiger, M. Etinski, S. Blaser, F. Hans-Martin, C. Marian, and S. Leutwyler. Intersystem crossing rates of S₁ state keto-amino cytosine at low excess energy. *The Journal of Chemical Physics*, 143, 2015.
- [23] J. A. Weil and J. R. Bolton. *Electron Paramagnetic Resonance*. John Wiley & Sons, Hoboken, New Jersey, second edition, 2007.
- [24] N. M. Atherton. *Principles of Electron Spin Resonance*. Ellis Horwood and Prentice Hall, Chichester, first edit edition, 1993.
- [25] S. Richert, C. E. Tait, and C. R. Timmel. Delocalisation of photoexcited triplet states probed by transient EPR and hyperfine spectroscopy. *Journal of Magnetic Resonance*, 280:103–116, 2017.

- [26] M. G. Newman and O. M. G. Lyons. Photovoltages In Tetracene Films. *Australian Journal of Chemistry*, 24:13–23, 1971.
- [27] A. K. Ghosh and T. Feng. Rectification, space-charge-limited current, photovoltaic and photoconductive properties of Al/tetracene/Au sandwich cell. *Journal of Applied Physics*, 44:2781–2788, 1973.
- [28] A. K. Ghosh, D. L. Morel, T. Feng, R. F. Shaw, and C. A. Rowe. Photovoltaic and rectification properties of Al/Mg phthalocyanine/Ag Schottky-barrier cells. *Journal of Applied Physics*, 45:230–236, 1974.
- [29] C. W. Tang and A. C. Albrecht. Photovoltaic effects of metal-chlorophyll-a-metal sandwich cells. *The Journal of Chemical Physics*, 62:2139–2149, 1975.
- [30] M. A. Green, K. Emery, Y. Hishikawa, and W. Warta. Solar cell efficiency tables (version 33). *Progress in Photovoltaics: Research and Applications*, 17:85–94, 2009.
- [31] M. A. Green, Y. Hishikawa, E. D. Dunlop, D. H. Levi, J. Hohl-Ebinger, M. Yoshita, and A. W. Y. Ho-Baillie. Solar cell efficiency tables (Version 53). *Progress in Photovoltaics: Research and Applications*, 27:3–12, 2019.
- [32] D. W. Laird, S. Vaidya, S. Li, M. Mathai, B. Woodworth, E. Sheina, S. Williams, and T. Hammond. Advances in Plexcore active layer technology systems for organic photovoltaics: roof-top and accelerated lifetime analysis of high performance organic photovoltaic cells. *Proceedings of SPIE*, 6656, 2007.
- [33] W. Zhao, S. Li, H. Yao, S. Zhang, Y. Zhang, B. Yang, and J. Hou. Molecular Optimization Enables over 13% Efficiency in Organic Solar Cells. *Journal of the American Chemical Society*, 139:7148–7151, 2017.
- [34] W. Li, L. Ye, S. Li, H. Yao, H. Ade, and J. Hou. A High-Efficiency Organic Solar Cell Enabled by the Strong Intramolecular Electron Push–Pull Effect of the Nonfullerene Acceptor. *Advanced Materials*, 30, 2018.
- [35] S. Zhang, Y. Qin, J. Zhu, and J. Hou. Over 14% Efficiency in Polymer Solar Cells Enabled by a Chlorinated Polymer Donor. *Advanced Materials*, 30, 2018.
- [36] J. J. M. Halls, J. Cornil, D. A. dos Santos, R. Silbey, D. H. Hwang, A. B. Holmes, J. L. Brédas, and R. H. Friend. Charge- and energy-transfer processes at polymer/polymer interfaces: A joint experimental and theoretical study. *Physical Review B*, 60:5721–5727, 1999.
- [37] G. Yu, J. Gao, J. C. Hummelen, F. Wudl, and A. J. Heeger. Polymer photovoltaic cells: Enhanced efficiencies via a network of internal donor-accepter heterojunctions. *Science*, 270:1789–1791, 1995.
- [38] W. Li, K. H. Hendriks, A. Furlan, M. M. Wienk, and R. A. J. Janssen. High quantum efficiencies in polymer solar cells at energy losses below 0.6 eV. *Journal of the American Chemical Society*, 137:2231–2234, 2015.
- [39] R. A. J. Janssen and J. Nelson. Factors limiting device efficiency in organic photovoltaics. *Advanced Materials*, 25:1847–1858, 2013.

- [40] J. Yao, T. Kirchartz, M. S. Vezie, M. A. Faist, W. Gong, Z. He, H. Wu, J. Troughton, T. Watson, D. Bryant, and J. Nelson. Quantifying losses in open-circuit voltage in solution-processable solar cells. *Physical Review Applied*, 4, 2015.
- [41] S. M. Menke, N. A. Ran, G. C. Bazan, and R. H. Friend. Understanding Energy Loss in Organic Solar Cells: Toward a New Efficiency Regime. *Joule*, 2:25–35, 2018.
- [42] T. M. Burke, S. Sweetnam, K. Vandewal, and M. D. McGehee. Beyond Langevin Recombination: How Equilibrium Between Free Carriers and Charge Transfer States Determines the Open-Circuit Voltage of Organic Solar Cells. *Advanced Energy Materials*, 5, 2015.
- [43] A. Cuevas. The recombination parameter J_0 . *Energy Procedia*, 55:53–62, 2014.
- [44] W. Shockley and H. J. Queisser. Detailed Balance Limit of Efficiency of p-n Junction Solar Cells. *Journal of Applied Physics*, 32(3):510, 1961.
- [45] A. P. Monkman, H. D. Burrows, L. J. Hartwell, L. E. Horsburgh, I. Hamblett, and S. Navaratnam. Triplet Energies of p-Conjugated Polymers. *Physical Review Letters*, 86:1358–1361, 2001.
- [46] A. Rao, P. C. Y. Chow, S. Gélinas, C. W. Schlenker, C. Z. Li, H. L. Yip, A. K. Y. Jen, D. S. Ginger, and R. H. Friend. The role of spin in the kinetic control of recombination in organic photovoltaics. *Nature*, 500:435–9, 2013.
- [47] W. Chang, D. N. Congreve, E. Hontz, M. E. Bahlke, D. P. McMahon, S. Reineke, T. C. Wu, V. Bulović, T. Van Voorhis, and M. A. Baldo. Spin-dependent charge transfer state design rules in organic photovoltaics. *Nature Communications*, 6:6415, 2015.
- [48] C W Tang and S A Vanslyke. Organic electroluminescent diodes. *Applied Physics Letters*, 51:913–915, 1987.
- [49] Y. Q. Zhang, G. Zhong, and X. A. Cao. Concentration quenching of electroluminescence in neat Ir(ppy)₃ organic light-emitting diodes. *Journal of Applied Physics*, 108(8), 2010.
- [50] J. Lee, N. Aizawa, M. Numata, C. Adachi, and T. Yasuda. Versatile Molecular Functionalization for Inhibiting Concentration Quenching of Thermally Activated Delayed Fluorescence. *Advanced Materials*, 29, 2017.
- [51] Y. L. Chang. *Efficient Organic Light-Emitting Diodes (OLEDs)*. Pan Stanford Publishing, Singapore, first edition, 2015.
- [52] J. S. Kim, P. K. H. Ho, N. C. Greenham, and R. H. Friend. Electroluminescence emission pattern of organic light-emitting diodes: Implications for device efficiency calculations. *Journal of Applied Physics*, 88:1073–1081, 2000.
- [53] R. Meerheim, M. Furno, S. Hofmann, B. Lüssem, and K. Leo. Quantification of energy loss mechanisms in organic light-emitting diodes. *Applied Physics Letters*, 97:28–31, 2010.

- [54] K. Saxena, V. K. Jain, and D. Singh Mehta. A review on the light extraction techniques in organic electroluminescent devices. *Optical Materials*, 32(1):221–233, 2009.
- [55] S. Reineke, F. Lindner, G. Schwartz, N. Seidler, K. Walzer, B. Lüssem, and K. Leo. White organic light-emitting diodes with fluorescent tube efficiency. *Nature*, 459:234–8, 2009.
- [56] M. A. Baldo, D. F. O’Brien, Y. You, A. Shoustikov, S. Sibley, M.E. Thompson, and S R Forrest. Highly efficient phosphorescent emission from organic electroluminescent devices. *Nature*, 395:151–154, 1998.
- [57] M. A. Baldo, S. Lamansky, P. E. Burrows, M. E. Thompson, and S. R. Forrest. Very high-efficiency green organic light-emitting devices based on electrophosphorescence. *Applied Physics Letters*, 75:4–6, 1999.
- [58] S. Lamansky, P. Djurovich, D. Murphy, F. Abdel-Razzaq, H. E. Lee, C. Adachi, P. E. Burrows, S. R. Forrest, and M. E. Thompson. Highly Phosphorescent Bis-Cyclometalated Iridium Complexes : Synthesis, Photophysical Characterization, and Use in Organic Light Emitting Diodes. *Journal of the American Chemical Society*, 123:4304–4312, 2001.
- [59] R. J. Holmes, S. R. Forrest, Y. J. Tung, J. J. Kwong, S. Brown, S. Garon, and M. E. Thompson. Blue organic electrophosphorescence using exothermic host-guest energy transfer. *Applied Physics Letters*, 82:2422–2424, 2003.
- [60] C.-H Yang, Y.-M. Cheng, Y. Chi, C. J. Hsu, F. C. Fang, K.-T. Wong, P. T. Chou, C. H. Chang, M. H. Tsai, and C. C. Wu. Blue-Emitting Heteroleptic Iridium (III) Complexes Suitable for High-Efficiency Phosphorescent OLEDs. *Angewandte Chemie*, 119:2470–2473, 2007.
- [61] M. Y. Wong and E. Zysman-Colman. Purely Organic Thermally Activated Delayed Fluorescence Materials for Organic Light-Emitting Diodes. *Advanced Materials*, 29:1–54, 2017.
- [62] Y. Zhang, J. Lee, and S. R. Forrest. Tenfold increase in the lifetime of blue phosphorescent organic light-emitting diodes. *Nature Communications*, 5:1–7, 2014.
- [63] H. Yersin, A. F. Rausch, R. Czerwieniec, T. Hofbeck, and T. Fischer. The triplet state of organo-transition metal compounds. Triplet harvesting and singlet harvesting for efficient OLEDs. *Coordination Chemistry Reviews*, 255:2622–2652, 2011.
- [64] A. Endo, M. Ogasawara, A. Takahashi, D. Yokoyama, Y. Kato, and C. Adachi. Thermally Activated Delayed Fluorescence from Sn 4+-Porphyrin Complexes and Their Application to Organic Light-Emitting Diodes — A Novel Mechanism for Electroluminescence. *Advanced Materials*, 21:4802–4806, 2009.
- [65] J. C. Deaton, S. C. Switalski, D. Y. Kondakov, R. H. Young, T. D. Pawlik, D. J. Giesen, S. B. Harkins, A. J. M. Miller, S. F. Mickenberg, and J. C. Peters. E-Type Delayed Fluorescence of a Phosphine-Supported Cu₂(μ-NAr₂)₂ Diamond Core : Harvesting Singlet and Triplet Excitons in OLEDs. *Journal of the American Chemical Society*, 132:9499–9508, 2010.

- [66] A. Endo, K. Sato, K. Yoshimura, K. Takahiro, A. Kawada, H. Miyazaki, and C. Adachi. Efficient up-conversion of triplet excitons into a singlet state and its application for organic light emitting diodes. *Applied Physics Letters*, 98, 2011.
- [67] H. Uoyama, K. Goushi, K. Shizu, H. Nomura, and C. Adachi. Highly efficient organic light-emitting diodes from delayed fluorescence. *Nature*, 492:234–238, 2012.
- [68] C. Murawski, K. Leo, and M. C. Gather. Efficiency roll-off in organic light-emitting diodes. *Advanced Materials*, 25:6801–6827, 2013.
- [69] S. Reineke, K. Walzer, and K. Leo. Triplet-exciton quenching in organic phosphorescent light-emitting diodes with Ir-based emitters. *Physical Review B*, 75(12), 2007.
- [70] D. Song, S. Zhao, Y. Luo, and H. Aziz. Causes of efficiency roll-off in phosphorescent organic light emitting devices: Triplet-triplet annihilation versus triplet-polaron quenching. *Applied Physics Letters*, 97, 2010.
- [71] N. C. Giebink and S. R. Forrest. Quantum efficiency roll-off at high brightness in fluorescent and phosphorescent organic light emitting diodes. *Physical Review B*, 77, 2008.
- [72] V. Shrotriya, G. Li, Y. Yao, T. Moriarty, K. Emery, and Y. Yang. Accurate measurement and characterization of organic solar cells. *Advanced Functional Materials*, 16:2016–2023, 2006.
- [73] T. Smith and J. Guild. The C.I.E. colorimetric standards and their use. *Transactions of the Optical Society*, 33(3), 1931.
- [74] N. C. Greenham, R. H. Friend, and D. D. C. Bradley. Angular Dependence of the Emission from a Conjugated Polymer Light-Emitting Diode: Implications for Efficiency Calculations. *Advanced Materials*, 6(6):491–494, 1994.
- [75] F. Urbach. The long-wavelength edge of photographic sensitivity and of the electronic absorption of solids. *Physical Review*, 92:1324, 1953.
- [76] J. A. Olley. Structural disorder and the Urbach edge. *Solid State Communications*, 13:1437–1440, 1973.
- [77] S. D. Stranks and H. J. Snaith. Metal-halide perovskites for photovoltaic and light-emitting devices. *Nature Nanotechnology*, 10:391–402, 2015.
- [78] J. C. de Mello, H. F. Wittman, and R. H. Friend. An Improved Experimental Determination of External Photoluminescence Quantum Efficiency. *Advanced Materials*, 9:230–232, 1997.
- [79] F. G. Celii, T. B. Harton, and O. F. Phillips. Characterization of organic thin films for OLEDs using spectroscopic ellipsometry. *Journal of Electronic Materials*, 26:366–371, 1997.
- [80] A. S. Romanov, C. R. Becker, C. E. James, D. Di, D. Credginton, M. Linnolahti, and M. Bochmann. Copper and Gold Cyclic (Alkyl)(amino) carbene Complexes with Sub-Microsecond Photoemissions : Structure and Substituent Effects on Redox and Luminescent Properties. *Chemistry - A European Journal*, 23:4625–4637, 2017.

- [81] D. Di, A. S. Romanov, L. Yang, J. M. Richter, J. P. H. Rivett, S. Jones, T. H. Thomas, M. A. Jalebi, R. H. Friend, M. Linnolahti, M. Bochmann, and D. Credgington. High-performance light-emitting diodes based on carbene-metal-amides. *Science*, 356:159–163, 2017.
- [82] H. M. J. Wang, C. S. Vasam, T. Y. R. Tsai, S. H. Chen, A. H. H. Chang, and I. J. B. Lin. Gold(I) N-heterocyclic carbene and carbazolate complexes. *Organometallics*, 24:486–493, 2005.
- [83] C. Jeong, C. Coburn, M. Idris, Y. Li, P. I. Djurovich, M. E. Thompson, and S. R. Forrest. Understanding molecular fragmentation in blue phosphorescent organic light-emitting devices. *Organic Electronics: physics, materials, applications*, 64:15–21, 2019.
- [84] R. Hamze, J. L. Peltier, D. Sylvinson, M. Jung, J. Cardenas, R. Haiges, M. Soleilhavoup, R. Jazzar, P. I. Djurovich, G. Bertrand, and M. E. Thompson. Eliminating nonradiative decay in Cu(I) emitters: >99% quantum efficiency and microsecond lifetime. *Science*, 363:601–606, 2019.
- [85] P. J. Conaghan, S. M. Menke, A. S. Romanov, S. T. E. Jones, A. J. Pearson, E. W. Evans, M. Bochmann, N. C. Greenham, and D. Credgington. Efficient Vacuum-Processed Light-Emitting Diodes Based on Carbene – Metal – Amides. *Advanced Materials*, 30, 2018.
- [86] A. S. Romanov, S. T. E. Jones, L. Yang, P. J. Conaghan, D. Di, M. Linnolahti, D. Credgington, and M. Bochmann. Mononuclear Silver Complexes for Efficient Solution and Vacuum-Processed OLEDs. *Advanced Optical Materials*, 6, 2018.
- [87] S. Shi, M. C. Jung, C. Coburn, A. Tadle, D. M. R. Sylvinson, P. I. Djurovich, S. R. Forrest, and M. E. Thompson. Highly Efficient Photo- and Electroluminescence from Two-Coordinate Cu(I) Complexes Featuring Nonconventional N-Heterocyclic Carbenes. *Journal of the American Chemical Society*, 141:3576–3588, 2019.
- [88] J. Föllner and C. M. Marian. Rotationally Assisted Spin-State Inversion in Carbene - Metal - Amides Is an Artifact. *Journal of Physical Chemistry Letters*, 8(22):5643–5647, 2017.
- [89] E. J. Taffet, Y. Olivier, F. Lam, D. Beljonne, and G. D. Scholes. Carbene - Metal - Amide Bond Deformation, Rather Than Ligand Rotation, Drives Delayed Fluorescence. *Journal of Physical Chemistry Letters*, 9:1620–1626, 2018.
- [90] J. S. Kim, M. Granström, R. H. Friend, N. Johansson, W. R. Salaneck, R. Daik, W. J. Feast, and F. Cacialli. Indium–tin oxide treatments for single- and double-layer polymeric light-emitting diodes : The relation between the anode physical, chemical, and morphological properties and the device performance. *Journal of Applied Physics*, 84(12):6859–6870, 1998.
- [91] Y. Yang, P. Cohn, A. L. Dyer, S.-h. Eom, J. R. Reynolds, R. K. Castellano, and J. Xue. Blue-Violet Electroluminescence from a Highly Fluorescent Purine. *Chemistry of Materials*, 22:3580–3582, 2010.

- [92] R. J. Holmes, B. W. D'Andrade, S. R. Forrest, X. Ren, J. Li, and M. E. Thompson. Efficient, deep-blue organic electrophosphorescence by guest charge trapping. *Applied Physics Letters*, 83(18):3818–3820, 2003.
- [93] H. Etori, T. Yasuda, X. L. Jin, K. Fujita, S. Mataka, and T. Tsutsui. Design of Multilayer Structure for UV Organic Light-Emitting Diodes Based on 2-(2-Naphthyl)-9,9'-spirobifluorene. *Japanese Journal of Applied Physics*, 46:5071–5075, 2007.
- [94] S. Gong, X. He, Y. Chen, Z. Jiang, C. Zhong, D. Ma, J. Qin, and C. Yang. Simple CBP isomers with high triplet energies for highly efficient blue electrophosphorescence. *Journal of Materials Chemistry*, 22:2894–2899, 2012.
- [95] G. Méhes, K. Goushi, W. J. Potscavage, and C. Adachi. Influence of host matrix on thermally-activated delayed fluorescence: Effects on emission lifetime, photoluminescence quantum yield, and device performance. *Organic Electronics*, 15:2027–2037, 2014.
- [96] S. K. Jeon, H. J. Park, and J. Y. Lee. Blue-shifted emission color and high quantum efficiency in solution-processed blue thermally activated delayed fluorescence organic light-emitting diodes using an intermolecular interaction suppressing host decorated with blocking groups. *Journal of Materials Chemistry C*, 6:6778–6783, 2018.
- [97] L. S. Hung, C. W. Tang, and M. G. Mason. Enhanced electron injection in organic electroluminescence devices using an Al/LiF electrode. *Applied Physics Letters*, 70:152–154, 1997.
- [98] T. Mori, H. Fujikawa, S. Tokito, and Y. Taga. Electronic structure of 8-hydroxyquinoline aluminum/LiF/Al interface for organic electroluminescent device studied by ultraviolet photoelectron spectroscopy. *Applied Physics Letters*, 73:2763–2765, 1998.
- [99] Q. Zhang, D. Tsang, H. Kuwabara, Y. Hatae, B. Li, T. Takahashi, S. Y. Lee, T. Yasuda, and C. Adachi. Nearly 100% Internal Quantum Efficiency in Undoped Electroluminescent Devices Employing Pure Organic Emitters. *Advanced Materials*, 27(12):2096–2100, 2015.
- [100] N K Patel, S Cinà, and J H Burroughes. High-Efficiency Organic Light-Emitting Diodes. *Journal on Selected Topics In Quantum Electronics*, 8(2):346–361, 2002.
- [101] Y. Kawamura, K. Goushi, J. Brooks, J. J. Brown, H. Sasabe, and C. Adachi. 100% phosphorescence quantum efficiency of Ir(III) complexes in organic semiconductor films. *Applied Physics Letters*, 86, 2005.
- [102] N. C. Erickson and R. J. Holmes. Investigating the Role of Emissive Layer Architecture on the Exciton Recombination Zone in Organic Light-Emitting Devices. *Advanced Functional Materials*, 23:5190–5198, 2013.
- [103] Y. H. Chung, L. Sheng, X. Xing, L. Zheng, M. Bian, Z. Chen, L. Xiao, and Q. Gong. A pure blue emitter (CIE_y = 0.08) of chrysene derivative with high thermal stability for OLED. *Journal of Materials Chemistry C*, 3:1794–1798, 2015.

- [104] G. Blasse and D. R. McMillin. On the luminescence of bis (triphenylphosphine) phenanthroline copper (I). *Chemical Physics Letters*, 70:1–3, 1980.
- [105] M. Hong, M. K. Ravva, P. Winget, and J. L. Brédas. Effect of Substituents on the Electronic Structure and Degradation Process in Carbazole Derivatives for Blue OLED Host Materials. *Chemistry of Materials*, 28:5791–5798, 2016.
- [106] A. Y. Freidzon, A. A. Safonov, A. A. Bagaturyants, D. N. Krasikov, B. V. Potapkin, A. A. Osipov, A. V. Yakubovich, and O. Kwon. Predicting the Operational Stability of Phosphorescent OLED Host Molecules from First Principles: A Case Study. *Journal of Physical Chemistry C*, 121:22422–22433, 2017.
- [107] N. Lin, J. Qiao, L. Duan, H. Li, L. Wang, and Y. Qiu. Achilles heels of phosphine oxide materials for OLEDs: Chemical stability and degradation mechanism of a bipolar phosphine oxide/carbazole hybrid host material. *Journal of Physical Chemistry C*, 116:19451–19457, 2012.
- [108] C. A. Hutchison and B. W. Mangum. Paramagnetic resonance absorption in Naphthalene in its phosphorescent state. *The Journal of Chemical Physics*, 29:952–953, 1958.
- [109] H. Levanon and J. R. Norris. The Photoexcited Triplet State and Photosynthesis. *Chemical Reviews*, 78:185–198, 1978.
- [110] T. Biskup, E. Schleicher, A. Okafuji, G. Link, K. Hitomi, E. D. Getzoff, and S. Weber. Direct observation of a photoinduced radical pair in a cryptochrome blue-light photoreceptor. *Angewandte Chemie - International Edition*, 48:404–407, 2009.
- [111] F. Kraffert, R. Steyrlleuthner, S. Albrecht, D. Neher, M. C. Scharber, R. Bittl, and J. Behrends. Charge separation in PCPDTBT:PCBM blends from an EPR perspective. *Journal of Physical Chemistry C*, 118:28482–28493, 2014.
- [112] T. Ogiwara, Y. Wakikawa, and T. Ikoma. Mechanism of Intersystem Crossing of Thermally Activated Delayed Fluorescence Molecules. *The Journal of Physical Chemistry A*, 119:3415–3418, 2015.
- [113] H. S. Kim, S.-R. Park, and M. C. Suh. Concentration Quenching Behavior of Thermally Activated Delayed Fluorescence in a Solid Film. *Journal of Physical Chemistry C*, 121:13986–13997, 2017.
- [114] S. Stoll and A. Schweiger. EasySpin , a comprehensive software package for spectral simulation and analysis in EPR. *Journal of Magnetic Resonance*, 178:42–55, 2006.
- [115] B. Yurash, H. Nakanotani, Y. Olivier, D. Beljonne, C. Adachi, and T. Q. Nguyen. Photoluminescence Quenching Probes Spin Conversion and Exciton Dynamics in Thermally Activated Delayed Fluorescence Materials. *Advanced Materials*, In press, 2019.
- [116] A. Köhler, H. F. Wittmann, R. H. Friend, M. S. Khan, and J. Lewis. The photovoltaic effect in a platinum poly-yne. *Synthetic Metals*, 67:245–249, 1994.

- [117] R. N. Marks, J. J. M. Halls, D. D. C. Bradley, R. H. Friend, and A. B. Holmes. The photovoltaic response in poly(p-phenylene vinylene) thin-film devices. *Journal of Physics: Condensed Matter*, 6:1379–1394, 1994.
- [118] M. A. Baldo and S. R. Forrest. Transient analysis of organic electrophosphorescence: I. Transient analysis of triplet energy transfer. *Physical Review B*, 62, 2000.
- [119] N. C. Giebink, Y. Sun, and S. R. Forrest. Transient analysis of triplet exciton dynamics in amorphous organic semiconductor thin films. *Organic Electronics*, 7:375–386, 2006.
- [120] W. A. Luhman and R. J. Holmes. Enhanced exciton diffusion in an organic photovoltaic cell by energy transfer using a phosphorescent sensitizer. *Applied Physics Letters*, 94, 2009.
- [121] C. L. Lee, I. W. Hwang, C. C. Byeon, B. H. Kim, and N. C. Greenham. Triplet exciton and polaron dynamics in phosphorescent dye blended polymer photovoltaic devices. *Advanced Functional Materials*, 20:2945–2950, 2010.
- [122] F. A. Angel and C. W. Tang. Understanding the effect of triplet sensitizers in organic photovoltaic devices. *Organic Electronics*, 30:247–252, 2016.
- [123] T. N. Singh-Rachford and F. N. Castellano. Photon upconversion based on sensitized triplet-triplet annihilation. *Coordination Chemistry Reviews*, 254:2560–2573, 2010.
- [124] Y. Y. Cheng, T. Khoury, R. G. C. R. Clady, M. J. Y. Tayebjee, N. J. Ekins-Daukes, M. J. Crossley, and T. W. Schmidt. On the efficiency limit of triplet-triplet annihilation for photochemical upconversion. *Physical Chemistry Chemical Physics*, 12(1):66–71, 2010.
- [125] V. Gray, D. Dzebo, M. Abrahamsson, B. Albinsson, and K. Moth-Poulsen. Triplet-triplet annihilation photon-upconversion: Towards solar energy applications. *Physical Chemistry Chemical Physics*, 16(22):10345–10352, 2014.
- [126] T. F. Schulze, J. Czolk, Y. Y. Cheng, B. Fückel, R. W. MacQueen, T. Khoury, M. J. Crossley, B. Stannowski, K. Lips, U. Lemmer, A. Colmann, and T. W. Schmidt. Efficiency enhancement of organic and thin-film silicon solar cells with photochemical upconversion. *Journal of Physical Chemistry C*, 116:22794–22801, 2012.
- [127] D. Veldman, S. C. J. Meskers, and R. A. J. Janssen. The energy of charge-transfer states in electron donor-acceptor blends: insight into the energy losses in organic solar cells. *Advanced Functional Materials*, 19(12):1939–1948, 2009.
- [128] H. Wang, L. Xie, Q. Peng, L. Meng, Y. Wang, Y. Yi, and P. Wang. Novel thermally activated delayed fluorescence materials-thioxanthone derivatives and their applications for highly efficient OLEDs. *Advanced Materials*, 26(30):5198–5204, 2014.
- [129] M. Redecker, D. D. C. Bradley, M. Inbasekaran, W. W. Wu, and E. P. Woo. High Mobility Hole Transport Fluorene-Triarylamine Copolymers. *Advanced Functional Materials*, 11:241–246, 1999.

- [130] A. C. Morteani, A. S. Dhoot, J. S. Kim, C. Silva, N. C. Greenham, C. Murphy, E. Moons, S. Ciná, J. H. Burroughes, and R. H. Friend. Barrier-Free Electron-Hole Capture in Polymer Blend Heterojunction Light-Emitting Diodes. *Advanced Materials*, 15:1708–1712, 2003.
- [131] A. Köhler and D. Beljonne. The singlet-triplet exchange energy in conjugated polymers. *Advanced Functional Materials*, 14:11–18, 2004.
- [132] F. Archet, D. Yao, S. Chambon, M. Abbas, A. D'Aléo, G. Canard, M. Ponce-Vargas, E. Zaborova, B. Le Guennic, G. Wantz, and F. Fages. Synthesis of Bioinspired Curcuminoid Small Molecules for Solution-Processed Organic Solar Cells with High Open-Circuit Voltage. *ACS Energy Letters*, 2:1303–1307, 2017.
- [133] D. H. Kim, A. D'Aléo, X. K. Chen, A. D. S. Sandanayaka, D. Yao, L. Zhao, T. Komino, E. Zaborova, G. Canard, Y. Tsuchiya, E. Choi, J. W. Wu, F. Fages, J. L. Brédas, J. C. Ribierre, and C. Adachi. High-efficiency electroluminescence and amplified spontaneous emission from a thermally activated delayed fluorescent near-infrared emitter. *Nature Photonics*, 12:98–104, 2018.
- [134] S. Cook, H. Ohkita, J. R. Durrant, Y. Kim, J. J. Benson-Smith, J. Nelson, and D. D. C. Bradley. Singlet exciton transfer and fullerene triplet formation in polymer-fullerene blend films. *Applied Physics Letters*, 89, 2006.
- [135] E. T. Hoke, I. T. Sachs-Quintana, M. T. Lloyd, I. Kauvar, W. R. Mateker, A. M. Nardes, C. H. Peters, N. Kopidakis, and M. D. McGehee. The role of electron affinity in determining whether fullerenes catalyze or inhibit photooxidation of polymers for solar cells. *Advanced Energy Materials*, 2:1351–1357, 2012.
- [136] Y. Yuan, Y. Hu, Y. X. Zhang, J. D. Lin, Y. K. Wang, Z. Q. Jiang, L. S. Liao, and S. T. Lee. Over 10% EQE Near-Infrared Electroluminescence Based on a Thermally Activated Delayed Fluorescence Emitter. *Advanced Functional Materials*, 27, 2017.
- [137] M. C. Scharber, D. Mühlbacher, M. Koppe, P. Denk, C. Waldauf, A. J. Heeger, and C. J. Brabec. Design rules for donors in bulk-heterojunction solar cells - Towards 10 % energy-conversion efficiency. *Advanced Materials*, 18:789–794, 2006.
- [138] F. B. Kooistra, J. Knol, F. Kastenberg, L. M. Popescu, W. J. H. Verhees, J. M. Kroon, and J. C. Hummelen. Increasing the open circuit voltage of bulk-heterojunction solar cells by raising the LUMO level of the acceptor. *Organic Letters*, 9:551–554, 2007.
- [139] J. Liu, X. Guo, Y. Qin, S. Liang, Z. X. Guo, and Y. Li. Dumb-belled PCBM derivative with better photovoltaic performance. *Journal of Materials Chemistry*, 22:1758–1761, 2012.
- [140] B. W. Larson, J. B. Whitaker, X. B. Wang, A. A. Popov, G. Rumbles, N. Kopidakis, S. H. Strauss, and O. V. Boltalina. Electron affinity of Phenyl-C61-butyric acid methyl ester (PCBM). *Journal of Physical Chemistry C*, 117:14958–14964, 2013.
- [141] K. Tvingstedt, K. Vandewal, A. Gadisa, F. Zhang, J. Manca, and O. Inganäs. Electroluminescence from charge transfer states in polymer solar cells. *Journal of the American Chemical Society*, 131(33):11819–11824, 2009.

- [142] D. M. Guldi, H. Hungerbuehler, and K. D. Asmus. Redox and excitation studies with C60-substituted malonic acid diethyl esters. *Journal of physical chemistry*, 99:9380–9385, 1995.
- [143] S. Cook, R. Katoh, and A. Furube. Ultrafast studies of charge generation in PCBM: P3HT blend films following excitation of the fullerene PCBM. *Journal of Physical Chemistry C*, 113:2547–2552, 2009.
- [144] J. Liu, S. Chen, D. Qian, B. Gautam, G. Yang, J. Zhao, J. Bergqvist, F. Zhang, W. Ma, H. Ade, O. Inganäs, K. Gundogdu, F. Gao, and H. Yan. Fast charge separation in a non-fullerene organic solar cell with a small driving force. *Nature Energy*, 1:1–7, 2016.
- [145] D. Baran, T. Kirchartz, S. Wheeler, S. Dimitrov, M. Abdelsamie, J. Gorman, R. S. Ashraf, S. Holliday, A. Wadsworth, N. Gasparini, P. Kaienburg, H. Yan, A. Amassian, C. J. Brabec, J. R. Durrant, and I. McCulloch. Reduced voltage losses yield 10% efficient fullerene free organic solar cells with >1 V open circuit voltages. *Energy and Environmental Science*, 9:3783–3793, 2016.
- [146] J. Hou, O. Inganäs, R. H. Friend, and F. Gao. Organic solar cells based on non-fullerene acceptors. *Nature Materials*, 17:119–128, 2018.
- [147] D. Qian, Z. Zheng, H. Yao, W. Tress, T. R. Hopper, S. Chen, S. Li, J. Liu, S. Chen, J. Zhang, X. K. Liu, B. Gao, L. Ouyang, Y. Jin, G. Pozina, I. A. Buyanova, W. M. Chen, O. Inganäs, V. Coropceanu, J. L. Bredas, H. Yan, J. Hou, F. Zhang, A. A. Bakulin, and F. Gao. Design rules for minimizing voltage losses in high-efficiency organic solar cells. *Nature Materials*, 17:703–709, 2018.